UNIVERSITÀ DEGLI STUDI DI NAPOLI "FEDERICO II"

DOTTORATO DI RICERCA IN INGEGNERIA ELETTRONICA E DELLE TELECOMUNICAZIONI
XX CICLO

REMOTE CONTROL OF NANOMACHINES AND BIOLOGICAL PROCESSES BY MEANS OF NON OPTICAL ELECTROMAGNETIC FIELDS

GENNARO BELLIZZI

Il Coordinatore
Ch.mo Prof. Giovanni Poggi

Il Tutore
Ch.mo Prof. Ovidio M. Bucci

Anno Accademico 2007-2008

Acknowledgements

I wish to thank my advisor, Prof. Ovidio M. Bucci, for giving me the opportunity to work to this interesting and fascinating research activity.

Moreover, I wish to thanks Prof. Amedeo Capozzoli for his support during the first year of my Ph.D. studies, but mainly for his sincerely friendship.

Finally, I would like to thanks the BioIndustry Park Canavese for the hospitality and opportunity

Thank you very much

Gennaro Bellizzi

Contents

List of Acronyms IX

Introduction 1

1 State of art and open questions 5

1.1 Use of nanoparticles as transducer to activate biological nanomachines by means of non optical electromagnetic fields.....5

1.1.1 State of art, open questions and solution proposed in this thesis 7

1.2 Magnetic Fluid Hyperthermia.....8

1.2.1 State of art.....12

1.2.1.1 Specific Loss Power measurements.....13

1.2.1.2 In vitro e in vivo experiments.....15

1.2.2 Some open questions and solutions proposed in this thesis.....17

2 On the energy transfer between electromagnetic fields and biological nanomachines 19

2.1 Expression of the power dissipated by a non optical electromagnetic field on a biological nanomachine.....20

2.2 Energy transfer between electromagnetic field and biological nanomachine in practical applications.....24

2.2.1 The Hamad Schifferli's experiment and model.....24

2.2.2 Estimation of P_D in the Hamad Schifferli's model.....25

2.2.3 Some considerations on the hypotheses formulated in the Hamad Schifferli's model.....26

2.2.4 Estimation of P_D by including the quadrupolar contribution.....27

2.3 Conclusions.....29

3 Magnetic nanoparticles 31

3.1 Mechanisms of interaction with a magnetic field.....32

3.1.1 Magnetism in matter.....32

3.1.2 Nanomagnetism.....35

3.1.3 Anisotropy of the magnetic nanoparticles.....36

3.1.4 Superparamagnetism……...37
3.1.5 Ferrofluids……...……38
3.1.5.1 Equilibrium magnetization of a ferrofluid..…..…….39
3.1.5.2 Relaxation mechanisms in a ferrofluid……41
3.1.5.3 Ferromagnetic resonance in a ferrofluid……...44
3.1.5.4 Dynamic susceptibility of a ferrofluid……..45
3.1.5.5 Magnetic power dissipation in a ferrofluid……...48
3.2 Experimental validation of the models proposed for the magnetic susceptibility of a ferrofluid……..….50
3.2.1 Experimental values of the magnetic power absorbed by magnetite nanoparticles in suspension ……..……..….50
3.2.2 Experimental values of M_s e K_a for magnetite nanoparticles.……56
3.2.3 Comparison between experimental and theoretical values of the power absorbed by magnetite nanoparticles in suspension.……57
3.3 Conclusions……...…….58

4 Short/Open Coaxial Line multicells measurement technique 61

4.1 Requirement for the measurement of the magnetic permeability of water-based ferrofluids ……..…..…...62
4.2 Overview of the methods used in literature to measure the magnetic permeability of ferrofluids…….…….63
4.2.1 Transmission/Reflection measurement methods…….……63
4.2.2 Short Circuited Coaxial Line measurement technique…...……65
4.2.3 Open ended Coaxial Line measurement technique…...…..…….…67
4.2.4 Improvement of Short Circuited and Open Ended Coaxial Line measurement techniques…….68
4.2.5 Uncertainty analysis of the Transmission/Reflection and Short Circuited Coaxial Line measurement techniques…..…….70
4.3 The Short/Open Coaxial Line multicells measurement technique…….72
4.4 Uncertainty analysis of the Short/Open Coaxial Line multicells measurement technique……..75
4.5 Measurement apparatus…….……76
4.6 Experimental validation of the Short/Open Coaxial Line multicells measurement technique and apparatus……...…79
4.7 Conclusions……...……83

5 Wideband spectroscopy of a water-based ferrofluid and final considerations on the remote control of biological nanomachines 85

5.1 Main features of the investigated water-based ferrofluid……...…...85

5.2 Measurement results and discussion……...87

5.3 Conclusions on the measurement results……....93

5.4 Final considerations on the remote control of biological nanomachines……....94

6 Electromagnetic field and magnetic nanoparticle design for applications in anticancer hyperthermia 95

6.1 Criterion to selectively heat cancer in hyperthermia ……..……...…...97

6.1.1 Expression of p_m and p_e in the case of a spherical geometry and a step like heat generation……99

6.2 Electromagnetic field and nanoparticle design……..……...102

6.3 Conclusions...……..108

Summary and Conclusions 109

A Derivation of the expression for P_D 113

B Expression of the polarization coefficients for a metallic sphere with radius much smaller than the wavelength 125

C Electromagnetic characterization of a coil 131

D Uncertainty analysis 141

E Exact solution of the Pennen's Bio-Heat Equation in a finite spherical region characterized by a step-like heat generation 149

References 157

List of acronyms

Acronym	Description
AuNP	gold NanoParticle
BM	Background Medium
BNM	Biological NanoMachine
EF	Electric Field
EMF	ElectroMagnetic Field
FF	Ferrofluid
FM	FerroMagnetic
MF	Magnetic Field
MFH	Magnetic Fluid Hyperthermia
MNP	Magnetic NanoParticle
NM	NanoMachine
NP	NanoParticle
OECL	Open Ended Coaxial Line
PBHE	Pennen's BioHeat Equation
RF	RadioFrequency
SCCL	Short Circuited Coaxial Line
SD	Single Domain
SDR	Single Domain Radius
SLP	Specific Loss Power
S/OLC	Short/Open Coaxial Line
T/R	Transmission/Reflection
VNA	Vector Network Analyser
WFF	Water-based FerroFluid

Introduction

Nanotechnology can be defined as the science and engineering involved in designing, synthesis, characterization and application of materials and devices at nanometer scale.

Since much of biology happens at nanometer scale, it is expected that the recent advances of nano-scale technologies will produce major benefits principally in biomedical area.

In this context, in the last years, particular attention has been addressed to the possibility of using nanoparticles for diagnostic and therapeutic purposes. In fact, nanoparticles have some characteristics that make them particularly attractive for these purposes:

- dimension, comparable to those of biological macromolecules;
- possibility to cover them with biocompatible polymer allowing their linking to biological macromolecules;
- capability to interact with an applied non-optical electromagnetic field.

Nowadays, nanoparticles are already successfully exploited as contrast agent to increase the sensibility of some diagnostic techniques, such as Magnetic Resonance Imaging [1]. Moreover, nanoparticles have shown to be useful also as therapeutic agents in hyperthermia for cancer treatment. This emerging and promising technique of hyperthermia exploits, as source of heat to destroy cancerous tissues, the high capabilities exhibited by magnetic nanoparticles to convert in heating the energy associated to an applied radiofrequency magnetic field [2].

Obviously, the applications above described represent only a small part of the enormous potentialities that the integration of nanotechnology with biology and medicine (i.e. nano-biomedicine) could offer, especially for therapeutic purposes.

One of the most ambitious aims of nano-biomedicine is indubitably the realization of remotely controlled biological nanomachines [3]. Broadly speaking, a remotely controlled biological nanomachine can be defined as a system able to accomplish biological tasks at cellular scale, whose function can be activated through an applied external stimulus. Remotely controlled biological nanomachines are of great interest because their use could

completely revolutionize the existing therapeutic approaches, making, for example, drug delivery [4] a real opportunity.

Currently, one of main limits of the conventional pharmacologic therapies is represented by the uncontrolled delivery of the drugs to both diseased and healthy cells. This aspect, on one hand, strongly reduces the efficiency and efficacy of therapy in that one needs to administered large amount of drug to reach the therapeutic concentration at the target site. On the other hand, it produce significant adverse collateral effects on healthy organs, which can preclude the applicability of therapy on long times. Obviously, these limits could be completely overcome through a selective and controlled delivery of the drug to the only target cells. This task could be efficiently accomplished by using remotely controlled biological nanomachines as vehicles for the transport and selective release of the drug.

In similar fashion, remotely controlled biological nanomachine could be fruitfully exploited also to transport and substitute genes (gene delivery). In particular, one could build remotely controlled nanomachines able to selectively delivery genes and at same time to exploit the information therein contained to repair or regenerate damaged cells or tissues (regenerative biomedicine).

As a matter of fact, extremely efficient biological nanomachines already exist and are the biological macromolecules, such as protein, peptides, nucleic acids. Accordingly, currently, the main problem to be addressed to turn into reality remotely controlled biological nanomachine is to realize the control.

According to a recent experiment [5], this could be attained by using metallic nanoparticles as control unit and radiofrequency electromagnetic fields as control signal. In fact, it has been experimentally shown that it is possible to remotely and selectively induce the cyclical opening and closing of a double helix of DNA by attaching to it a gold nanocrystal and applying a radiofrequency electromagnetic field [5].

This result is very important in that makes the realization of remotely controlled biological nanomachines, for *in vivo* drug delivery or other biomedical applications, a concrete opportunity.

Accordingly, nanotechnology applied to biomedicine seems to have the potentiality to revolutionize medicine itself. In particular, from the preliminary experimental results, it appear that the major advances will come from using nanoparticles and non optical electromagnetic fields.

However, apart from some encouraging results on the use of nanoparticles and electromagnetic field for biomedical applications, the research in this field is still at an early stage.

Concerning the hyperthermia, although it is available a satisfactory number of experiences proving the ability of magnetic field and magnetic

nanoparticles to heat solid tumour above a therapeutic temperature, the choice of nanoparticles and the parameters of magnetic field to be exploited in the treatment is still carried out on the base of semi-empirical considerations and not on the base of designing criterions.

Concerning the remotely control of biological nanomachines, the state of research is even at an earlier stage, In fact, to the best of our knowledge, the experimental results reported in [5] is the first and only example available in open literature on the use of electromagnetic fields and nanoparticles to remotely control biological nanomachines.

Accordingly, the aim of this thesis is to investigate the possibility of using nanoparticles and non optical electromagnetic fields to:

a) remotely control biological nanomachines and processes;

b) selective destroy solid tumours by means of hyperthermia.

In particular, points a) and b) have been addressed by developing:

1) simple and accurate theoretical tools useful either to analyze the interaction mechanisms between an electromagnetic field and a nanomachine underlying the experimental results reported in literature [5] or to design biological nanomachines and the corresponding control apparatuses.

2) measurement strategy and apparatuses for measuring on a wide frequency range the electromagnetic parameters of nanoparticles, dispersed in biocompatible solvents

3) broadband spectroscopy of the electromagnetic parameters of above suspension;

4) Criterion to determine nanoparticles and electromagnetic field parameters for application in cancer hyperthermia.

The outline of the thesis is the following.

- In **Chapter 1** it is provided a critical analysis of the main results available in open literature on the use of nanoparticles and non optical electromagnetic fields for applications in hyperthermia and remote control of biological nanomachine, with particular attention to the open questions and the possible solutions to be adopted and proposed in this thesis.
- In **Chapter 2**, by using a classical macroscopic approach, it is derived a simple and accurate expression quantifying the power exchange between electromagnetic fields and biological nanomachines. Moreover, by exploiting the obtained expression it has been analyzed

the model of interaction suggested in [5] to justify the experimental results.

- In **Chapter 3** are presented and analyzed the main mechanisms of interaction between magnetic field and magnetic nanoparticles in suspension (ferrofluids) together with the theoretical models developed to describe their dependence on the physical parameters of magnetic nanoparticles and some interesting experimental data, reported in literature, on the magnetic properties of ferrofluids.
- In **Chapter 4** it is presented the measurement strategy and apparatus purposely designed and realized to measure on a wide frequency range the electromagnetic parameters of nanoparticles, dispersed in biocompatible solvents.
- In **Chapter 5** are presented and discussed the measurement results on the broadband spectroscopy of the complex permittivity and permeability of a commercial water-based ferrofluid, obtained by exploiting the measurement strategy and apparatus described in Chapter 4. Finally, by using the results obtained in the previous Chapters and others available in literature, it is critically analyzed the possibility of using nanoparticle and radiofrequency electromagnetic fields to remotely control biological nanomachines, by exploiting the mechanism of interaction proposed in [5].
- In **Chapter 6** it is provided a criterion to determine the values of nanoparticles and electromagnetic field parameters minimizing the therapeutic dose of magnetic nanoparticles to be administered in cancer hyperthermia
- In the section **Summary and Conclusions** are summarized and discussed the most interesting results obtained in this thesis and the future objectives

Finally, to improve readability, part of mathematics is presented in the **Appendix A**, **B**, **C**, **D** and **E**.

Chapter 1

State of art and open questions

In this Chapter it is provided a critical analysis of the main results available in open literature on the use of NanoParticles (NP) and non optical ElectroMagnetic Fields (EMF) for applications in hyperthermia and remote control of Biological NanoMachines (BNM), with particular attention to the open questions and the possible solutions to be adopted and proposed in this thesis.

1.1 Use of nanoparticles as transducers to activate biological nanomachines by means of non optical electromagnetic fields

As discussed in the Introduction, one of the most ambitious aims of nano-biomedicine is to realize remotely controlled BNMs. i.e. systems able to operate at nanometer scale, whose function can be activated by means of an applied external stimulus.

As a matter of fact, extremely efficient BNMs already exist in nature and are the biological macromolecules (such as protein, peptides, nucleic acids), which accomplish the biological processes underlying the life. Moreover, the modern techniques of molecular biology enable the synthesis, purification and collection and of a great variety of bio-macromolecules, natural and synthetic. Accordingly, the biological macromolecules appear to be the most suitable components to build remotely controlled BNMs. As a result, the main problem to be addressed to turn into reality remotely controlled BNMs is to realize the control.

Obviously, to be useful the control must be remote, selective, reversible and allow the biomedical application of BNMs.

A possible way to control BNMs is to exploit bio-chemical stimuli. For example, in [6] it has been shown that it is possible to change the structure of a DNA molecule in solution, denoted with “Body”, from a G-quadruplex configuration to a duplex one and viceversa, by adding in turn two other

kinds of DNA molecules, denoted with “Fuel” and “AntiFuel”. In particular, the addition of the DNA Fuel favours the transition from a G-quadruplex configuration to a duplex one; the subsequent addition of the DNA AntiFuel removes the DNA Fuel, by linking to it, allowing so to DNA-Body to come back to its initial G-quadruplex configuration.

In similar fashion, in [7] it has been shown that it is possible to wrap and unwrap a super-wound double helical DNA molecule in solution by changing the concentration of Mg^{2+} ions.

Conformational changes of bio-macromolecules in solution has been obtained also by varying the pH or other chemical properties of the solution.

Although efficient, the bio-chemical control has some advantages which make it unsuitable to remotely control BNMs. In particular, it produces results (like DNA Fuel-AntiFuel conjugate [6], Mg^{2+} ions [7] or other bio-chemical agents) whose accumulation in solution lead to:

- the progressive switching off of the control (low degree of reversibility);
- the chemical defiling of the solution and consequently limits of applicability in biomedical applications.

Control signals much more attractive are the RadioFrequency (RF) EMFs. In fact, they can easily penetrate the biological tissues without producing significant adverse biological effects if the heating produced, via Joule effect, by the electric component of the field is maintained sufficient small. Moreover, unlike bio-chemical control, the electromagnetic control does not produce results, which accumulating, inhibits the operation of the BNMs, therefore, it does not exhibit limits of reversibility or applicability in biomedical area characterizing the bio-chemical control.

However, to make bio-molecules sufficiently sensitive to an applied external electromagnetic stimulus, and so to allow their electromagnetic control, one needs to link them to devices which are:

- of dimensions comparable to those of the involved biological macromolecules;
- biocompatible, in order to allows their biomedical applications;
- sensitive to an applied RF EMF;
- able to affect the activity of attached bio-molecule in response to the applied external stimulus

Devices which seem to have the above characteristics are the NPs. In particular, the most interesting ones are:

- Magnetic NanoParticles (MNP), as suggests their applications in anticancer hyperthermia (see Chapter 6);
- gold nanoparticles (AuNP), as proposed in recent experimental experiences [5];

However, a part from a small number of experimental investigations showing the possibility of using NPs to remotely control BNMs by means of RF EMF, the research in this field is still at an early stage and therefore it needs of further investigations.

1.1.2 State of art, open questions and solution proposed in this thesis

To the best of our knowledge, the first and only case available in open literature on the use of non-optical EMF and NP to remotely control BNMs is the experimental results reported in [5]. Here, it has been shown that it is possible to remotely control, in a reversible and selective manner, the dehybridization of an hairpin DNA molecule by attaching it to a AuNP and applying the EMF produced by a coil working at 1 GHz.

Besides the biological relevance of the observed phenomenon, this results has attracted great attention in that a very simple mechanism of interaction between the applied EMF and BNM seems to be at the base of the observed effect: the local heating produced, via the Joule effect, by the conduction currents induced on the AuNP by the impinging EMF.

The understanding of the interaction mechanisms underlying the interactions EMF-BNM is a crucial step to successfully design remotely control BNMs and the relative control apparatuses.

However, the proposed model of interaction [5] is merely a hypothesis, because, till now, no theoretical study has been carried out to support its consistency. The reason is the absence of a properly and simple theoretical tool able to correctly describe the mechanisms of interaction between EMF and BNMs, probably due to the difficulty to describe the electromagnetic interaction at the borderline between quantum and classical physics. In fact, the number of atoms composing a BNMs could be too small to allow a classical-macroscopic approach, and too large to make a quantum approach feasible.

To this, it must be added a full lack of knowledge on the electromagnetic properties of the used NPs, likely due to the difficulty to measure on a wide frequency range the electromagnetic properties of such a NPs in a biocompatible environment.

Accordingly, to provide an univocal interpretation of the experimental results and to effectively design BNMs, remotely controlled, and electromagnetic control apparatuses for bio-medical applications, a first important step is represented by:

1) the development a accurate and simple theoretical tool able to correctly describe the interaction mechanisms and the energy transfer between EMFs and BNMs;
2) the accurate characterization, on a frequency range as large as possible, of the electromagnetic properties of the used NPs in a biocompatible environment.

These points has been successfully addressed in this first part of this thesis. In particular, point 1) is faced in Chapter 2 and 3, while point 2) is faced in Chapter 4 and 5.

1.2 Magnetic Fluid Hyperthermia

Hyperthermia is a method to treat cancer based on heating malignant tissues [2, 8, 9]. It is, in fact, well-established that it is possible to induce damaging or necrosis of cancerous cells by increasing their temperature above a therapeutic value, of about 42-46 °C, and keeping it for approximately 30 minutes [9].
Hyperthermia treatments are usually classified in two categories:

- mild hyperthermia, in which the temperature elevation of tumour is limited to less than about 42-45 °C
- thermoablation, where the temperature of the cancer is increased above 46 °C.

Mild hyperthermia induces almost reversible damage to malignant cells and tissues. However, its combined use with radiotherapy can significantly improve the efficacy of this cancer treatments. The improvement is due to heat-induced malfunction of the processes that repair the DNA-damages produced in cancerous cells by radiotherapy [10]. Mild hyperthermia also affects the activity of regulatory proteins, kinases and cyclins, which in turn alters cell growth and differentiation, and can induce apoptosis. On the contrary, thermoablation leads a direct destruction of the tumour by cell necrosis, coagulation or carbonisation [10]. Accordingly, unlike mild hyperthermia, thermoablation does not require a combined use with other cancer treatments.

Obviously, in both types of hyperthermia the heating must be selective, i.e. must involve only the diseased tissue. In other words, at same time, hyperthermia must guarantee the desired temperature enhancement within the tumour and a negligible temperature rise in the neighbouring healthy tissue, in order to preserve integrity [8-9].

Currently, an interesting modality to perform hyperthermia is based on the application of a RF EMF. This method, referred to as RF hyperthermia, exploit as source of heat, to elevate the temperature of cancer, the ability of biological tissues to dissipate the energy associated to an applied RF radiation, due to their non-null electric conductivity. The heating selectivity is achieved either by focusing the radiation on the target or by exploiting the higher conductivity of malignant tissues than healthy tissues due to the higher degree of vascularisation of tumours (cancer angiogenesis).

RF hyperthermia is more interesting than other proposed modalities of hyperthermia, like microwave, ultrasound or laser hyperthermia, since the high capability of RF EMF to penetrate biological tissues allows to treat deep-seated tumour in the body, inaccessible for the other techniques.

However, this technique, like others, do not allow to obtained the desired degree of heating selectivity, required to hit only target cells. The reasons are the difficulty to focus a RF radiation in a volume as small as a tumour and the low difference in electric conductivity between the diseased and healthy tissues, which does not enable to produce an appreciable gradient of temperature between the diseased and healthy regions.

In the past, many attempts has been carried out to enhance the heating selectivity of the RF hyperthermia. Improvements have been obtained by inserting near the tumour metallic electrodes, of millimetric size, and using capacitive applicators, i.e. designed for favouring the Electric Field (EF) component of applied EMF [11]. This approach significantly increases the electric conductivity of a small region containing the tumour and consequently the heating selectivity of the RF hyperthermia.

Nevertheless, this method have some limitations which limits its practical applicability on human patients. Firstly, the use of a radiation with high EF component may lead to the generation of uncontrolled and undesired heat-spots in the body, caused by the non-null electrical conductivity and the differences in electric permittivity of the diverse kinds of tissues, like muscles, bones, blood, fat, etc, composing the body. Second, millimetric-size implants require stressful surgical intervention to be inserted in the body. This aspect, on one hand, makes the therapy invasive; on the other hand, practically precludes its applicability to difficulty accessible cancers, like brain tumours. Third, this method produce non-uniform temperature pattern in the tumour.

In the recent years, as an alternative to the use of metallic implant and capacitive applicators, it has been proposed the use of magnetisable materials, like ferromagnetics or ferrimagnetics, and inductive applicators, like coils, where the EF component is lowered to the benefit of the magnetic one [11]. This solution is surely more attractive because does not present the problem of the heat-spots generation. In fact, biological tissues do not have intrinsic magnetic losses which could led to an uncontrolled heating of unexpected regions of the body, in presence of an alternating Magnetic Field (MF). Furthermore, this aspect also allows to significantly increase the heating selectivity because the heating is produced only by magnetic implant inserted near the tumour.

For this solution, however, remain the limits of a invasive stressful surgical intervention required to insert the implant and non-uniform temperature pattern in the tumour.

Currently, thanks to the recent advances of nanoscale technologies, these limits has been overcome by using MNPs as heating agents, instead of macroscopic ferromagnetic implants. This emerging technique of anticancer hyperthermia, referred to as Magnetic Fluid Hyperthermia (MFH), consists of introducing MNPs, in form of colloidal dispersion (i.e. magnetic fluid), directly inside the tumour and to apply a RF MF.

The physical mechanisms exploited to heat cancer is MFH are the loss processes that occur during the reorientation of the magnetization of MNPs when exposed to a alternating MF (see Chapter 3).

Experimental investigations on the application of MNPs for hyperthermia date back to 1957 when Gilchrist *et al* [12] heated various tissue samples with 20–100 nm size particles of γ -Fe_2O_3 exposed to a 1.2 MHz MF. Since then there have been numerous publications describing a variety of schemes using different types of MNPs, different MF strengths and frequencies and different methods of delivery of the NPs.

The main features which make MFH the most promising modality of anticancer hyperthermia are:

1) high transparency of biological tissues in the RF range;
2) heat generation restricted to the only tumour area, containing MNPs;
3) possibility of using MF intensities and frequency much more biologically tolerable than the ones required to heat macroscopic ferromagnetic implants.
4) possibility of minimally invasive administration of MNPs directly inside the cancer.

Point 1) in important in that allows to treat also deep-seated tumour in the body, inaccessible for the other techniques of hyperthermia.

Points 2) allows to obtain a selective heating of tumours, above a therapeutic temperature, leaving practically unaffected the neighbouring healthy tissue.

Concerning point 3), since nanostructured ferromagnetic materials, such as MNPs, have shown to have an absorbing power capability higher than the macroscopic ferromagnetic materials (see Chapter 3), their use in hyperthermia allows to successfully heat tumours with smaller MF intensities and frequencies. This aspect is very important in anticancer hyperthermia, because smaller the amplitude and frequency of the applied MF, smaller the adverse effects (like heat-spots generation) produced in the healthy tissues by the unavoidable presence of the EF component of the applied field, and consequently higher the heating selectivity of the treatment.

Concerning point 4), due to very small dimension of MNPs and the possibility to cover them with biocompatible polymers and/or bio-molecules, they can be directly administered inside the cancer as colloidal suspension. This feature allows to avoid the invasive and traumatic surgical intervention, needed to insert macroscopic implants, and, at same time, to obtain an quite uniform NP-concentration, and hence an quite uniform heat generation, in the cancer.

Currently, various modalities for delivering MNPs has been proposed. The simplest one, and thus the most used one, is the direct injection of MNPs inside diseased area, in form of colloidal suspension (intra-tumoural injection). This approach, although allows to concentrate a large amount of MNPs at the cancer site (up to some hundreds of milligram per millilitre [13]), is applicable only to well-localized and easily-accessible tumours in the body. Moreover, once injected, the NPs do not keep localized at the target site, but spread toward the surrounding healthy tissue [14]. The latter aspect significantly reduces the heating-selectivity of MFH.

A more selective and efficient methods of MNP-delivery can be achieved by using MNPs coated with specific bio-molecules (like proteins, peptides, hormones, antibodies etc.), able to stick only to target cells, administered via intravenous injection [2]. In fact, by exploiting the cardiovascular system it is possible to reach tumours anywhere in the body. Furthermore, the chemical functionalization of MNPs enables their accumulation only at the cancer sites and to keep them therein localized. Accordingly, MFH could be notably improved by adopting the described strategy. However, this emerging modality of MNP-targeting presents some limits as, for example, the impossibility to attain in the tumour the high MNP-concentrations reachable in the case of the intra-tumoural injection [9].

Besides the heating selectivity, an other important aim in MFH is to reduce as much as possible the effective amount of MNPs to be used in

the treatment (therapeutic dose) to obtain the therapeutic temperature raise inside the diseased tissue. Optimization of therapeutic dose of MNPs is important to limit the amount of material to be administered and consequently to be expelled after the treatment. Moreover, reducing the therapeutic dose of MNPs makes possible the use of modalities of MNP-administration more efficient than the intra-tumoural injection, but able to deliver a smaller amount of MNPs. An example is bio-chemical targeting of MNPs above-described.

A way to reduce the amount of MNPs required to obtain the desired temperature rise is to increase their absorbing power capability. This result can be obtained by increasing the amplitude, $|H|$, and/or frequency, f, of the applied MF (see Chapter 3). However, higher the values of $|H|$ and f, higher the intensity of the EF component of the applied field and consequently lower the degree of the heating selectivity of treatment. Accordingly, in MFH the choice of the MF amplitude and the working frequency is a trade-off between the requirement of heating selectivity and the minimization of the therapeutic dose of MNPs.

Indeed, the absorbing power capability of MNPs strongly depends also on their physical features, like magnetic size magnetic material composing the MNPs, etc. (see Chapter 3). Therefore, a crucial step to minimize the therapeutic dose of MNPs, without affecting the EF intensity, is to properly choose the characteristics of MNPs. In literature many efforts has been addressed to identifying the optimal values of the MF and MNPs parameters. The most interesting result are discussed in the next section.

As a concluding remark, it is worth noting that MFH, and more generally anticancer hyperthermia, can successfully treat only tumour of moderate size, not smaller than about 1 cm. In fact, as it well-known, smaller the tumour-size, higher the capability of tumour to transfer heat toward the surrounding healthy tissues and consequently harder is to elevate the temperature of cancer above the therapeutic value. As a result, MFH is not able to treat small metastases disseminated in the body, as suggested by some Authors [8]. However, this therapy can be helpful also for small cancer if used in combination with other cancer treatments, like radio and chemo therapies.

1.2.1 State of art

In literature there are many studies which confirm the feasibility of MFH as anticancer treatment. They can be classified in three categories:

- Specific Loss Power measurements;

- in vitro experiments;
- in vivo experiments;

Later on, for each category are presented and discussed the most interesting results available in open literature.

1.2.1.1 Specific Loss Power measurements

The Specific Loss Power (SLP) of an assembly of MNPs, like magnetic fluids, represents the mean magnetic power absorbed by the assembly, per gram of magnetic material, when exposed to an alternating MF of assigned frequency and amplitude ([SLP] = W/g). Accordingly, SLP provides a direct estimation of the capability of MNPs to convert in heating the energy associated to an applied alternating MF. As a result, measuring SLP is a crucial step to investigate the feasibility of MFH as anticancer treatment.

In literature are available a satisfactory number of experimental data on SLP of MNPs, most of which are referred to magnetite (Fe_3O_4) NPs dispersed in water or in other physiological fluids. Obviously, the choice to investigate Fe_3O_4-NPs is not arbitrary, but imposed by biocompatibility constraints. In fact, magnetite is the only magnetic material biocompatible and consequently the only one exploitable in biomedical applications. It is worth noting that this fact strongly limits the possibility of reducing the therapeutic dose of MNPs to be used in hyperthermia in that reduces the number physical parameters on which one can act to minimize the dose of NPs.

The SLP measurements reported in literature cover a wide range of Fe_3O_4-NPs size, MF amplitude and frequency. The aim has been to investigate the influence of MF and NP parameters on the SLP and, at same time, to identify the values of these parameters for which the SLP has a maximum.

It is worth noting that the frequencies and amplitudes used in the experiments are not arbitrarily chosen, but their value is upper bounded in order to limits the intensity of the EF component of the applied field and so to save heating selectivity. In particular, the values of f and $|H|$ are chosen by assuming that the product $|H|f$ does not exceed the safety value 4.85×10^8 A/ms, obtained through clinical trials. In fact, it has been experimentally found that below 4.85×10^8 A/ms the EF generated by a coil with a diameter of about 30 cm produces a tolerable heating in the surrounding healthy tissue for a treatment duration of one hour [15]. However, due to the empirical character of such condition, it does not provides the actual constraint on the

Magnetic material	Magnetic size (nm)	$\|H\|$ kA/m	f (kHz)	solvent	SLP (W/g)	ref
Fe_3O_4	6	14	300	water	0.5	[16]
Fe_3O_4	8	14	300	water	97	[16]
Fe_3O_4	10	7.2	880	water	210	[19]
γ-Fe_2O_3	15	11	410	water	600	[17]
γ-Fe_2O_3	18	8	400	water	160	[18]
γ-Fe_2O_3	150	7.2	880	water	45	[19]
Fe_3O_4	250	14	300	water	42	[16]

Tab. 1.1. Specific Loss Power of various magnetic nanoparticles.

values of f and $|H|$ exploitable in MHF. Hopefully, it is expected that the real constraint on of the product $|H|f$ is larger than the one proposed empirically in [15]. As a result, to minimize the therapeutic dose of NP and simultaneously save heating selectivity, a crucial step is to individuate the actual constraint an the product $|H|f$.

In Tab 1.1 are reported some of the most interesting data on SLP available in open literature. They include data on both very large (size large than 100 nm) and ultrafine (size of about 10 nm) Fe_3O_4-NPs.

As can be seen, the value of SLP significantly changes with the NP and MF parameters, indicating a strong dependence of SLP on such parameters. Moreover, the SLP of ultrafine Fe_3O_4-NPs are higher than the SLP of quasi-micrometer NP, confirming an higher capability of nanostructured magnetic materials to absorb power. Accordingly, for application in MFH, ultrafine Fe_3O_4-NPs are more appropriate than large particle in that they are able to dissipate larger amount of energy at more medically tolerable MF amplitude and frequency.

Finally, let us note that the largest value of SLP listen in Tab. 1.1, of 600 W/g, is reached for Fe_3O_4-NPs of 15 nm in size and for a MF amplitude and frequency of 400 kHz and 11 kA/m respectively. These values are not determined on the base of a systematic and rigorous approach, but they are merely the result of trials. The only constraint imposed is the empirical one on the product $|H|f$[(*)]. By exploiting the maximum SLP reported in Tab. 1.1 one could obtain the therapeutic temperature rise inside the diseased tissues with a dose magnetite not larger than of few tens of milligrams per cubic centimetre of tumour. A dose which could be further reduced by determining the MF and NP parameters as a result a optimization procedure based on a rigours description of the problem.

(*) Sometime, the value 4.85×10^8 A/ms is exceeded depending on the diameter of the region to be treated and by the treatment duration

1.2.1.2 In vitro e in vivo experiments

In literature, besides SLP measurements, it is available also an extensive number of in vitro and in vivo experiments on animal models. The aim of these experiments has been to test the real efficacy of Magnetic fluid Hyperthermia in eliminating cancerous cells.
In addition, the in vivo experiments have allowed also to study some important aspects as:

- the influence of some factors, like blood perfusion and electric and thermal heterogeneities of the tissues, on heating of diseased and healthy tissues in MFH;
- possible non thermal effects induced by the applied RF radiation in biological tissues
- possible adverse effects induced by the circulation of Fe_3O_4-NPs in the body, like toxicity, arterial embolization, etc.

In the following are presented and discussed some of most interesting results on in vivo experiments presented in literature.

In [20] the heating effects of MNPs on a New Zealand rabbit with a liver carcinoma of 2 cm in size were investigated. A colloidal suspension containing 50 mg of Fe_3O_4-NPs with an average diameter of 10 nm was injected into the centre of the tumour. Then, the rabbit was putted in a coil and irradiated with a MF, having a frequency of 55 kHz and an amplitude of 20 kA/m, for 600 s. A temperature higher than 45 °C in the tumour core and lower 43.3 °C at tumour border, over a treatment duration of 600 sec was observed proving the capability of Fe_3O_4-NPs to increase the temperature of the entire tumour above the therapeutic value of 43 °C.

In [21] the effects of Magnetic Fluid Hyperthermia on human mammary carcinoma implanted in mice was investigated. Magnetic fluid containing Fe_3O_4-NPs of 10 nm in size was delivered by intra-tumoural injection in dose of 15 mg magnetite/cm^3 of tumour. Post-injection examination of the cancerous tissues showed deep fluid penetration. An alternating MF with an amplitude tuned between 6 – 12.5 kA/m and frequency of 520 kHz was applied for 20 – 30 minutes. Widespread death of cancerous cells was observed after Magnetic Fluid Hyperthermia treatment indicating the efficacy of treatment.

In [22] the results of a similar experimental investigation were reported. In particular, a solution of antibody-functionalized Fe_3O_4-NPs of 20 nm in size were injected intravenously into mice bearing human breast cancers.

The amount of nanoparticles delivered for gram of tumour, 48 hours after intravenously injection, was 0.3 mg. Then, mice were grouped in five groups (each group consisted of ten mice) and each of them was exposed to a different alternating MF (produced by a coil) having same frequency, of 153 kHz, but different amplitude and duty-cycle. In particular, the used amplitudes and duty-cycles were 113 kA/m, 104 kA/m, 56 kA/m at 30%, 60%, and 90% duty-cycle, respectively, and 84 kA/m at 50% and 70% duty-cycle, over a treatment duration of 20 min. Concerning the observed results, six of ten mice of the group exposed to the highest MF amplitude duty-cycle, of 104 kA/m and 60%, died acutely. Tumour regression occurred in all of the other groups, except for the group exposed to the lowest amplitude duty-cycle, confirming the substantial efficacy of treatment.

Accordingly, the in vivo study reported in literature have demonstrated the therapeutic efficacy of MFH, at least, on animal models. However, the choice of NP-size, amplitude and frequency of the applied MF, modalities of exposition (continuous or pulsed irradiation) and treatment duration is not carried out by using optimization procedure based on a rigorous description of the problem, but on the base of empirical considerations, often derived by experimental trials. The NP and MF parameters, in best of cases, are chosen on the base of SLP data available in literature (see Sec. 1.2.1.1). In most of cases, the choice of these parameters depended more on the commercial availability of the NPs and MF applicators rather than on theoretical predictions for optimised SLP. The only condition imposed is $|H|f \leq 4.85\times10^{8}$ A/ms, sometime not even respected, as happens for the experiments above quoted.

Concerning the exposition modalities and treatment duration, in [20] the irradiation was clearly stopped as soon as the temperature of the tumour, continuously monitored in the experiment, exceeded the therapeutic value of 43 °C, confirming that the treatment duration was not established on the base of theoretical considerations.

Similarly, in the experiment reported in [21] the amplitude of the applied MF was continuously tuned to balance possibly overheating due to a too high MF amplitude.

In [22] the choice of using a pulsed irradiation is clearly based on empirical considerations. This hypothesis is well supported by the significant number of mice death (six mice) and mice not cured (ten mice) after treatment.

Accordingly, to improve the MFH it is crucial to derive rigorous tools for the determination of the optimal NP and MF parameters. Obviously, a key role is played by the designing of properly exposition apparatuses, able to minimize the EF component with respect to the magnetic one and simultaneously to focus the radiation on the target. Currently, the most used

MFH applicators are induction coils or air-gap of a magnetic inductor, which surely do not represent the best solutions adoptable in MFH (see Appendix C).

Finally, it is must be stressed that all the in vivo experiment reported in literature are performed on animals with very small size, like mice rabbits hamsters. This aspect makes difficult the scaling of the observed results on human patients, thus making even more crucial the definition of rigorous criterions to determine the optimal NP-size, amplitude and frequency of the applied MF, as well as the designing of properly exposition equipments to be exploit in MFH.

1.2.2 Some open questions and solutions proposed in this thesis

As discussed in Sec 1.2 one of the main aims of MFH is to minimize the therapeutic dose of Fe_3O_4-NPs. However, this result cannot be achieved by simply increasing the MF intensity and frequency, because of the constraint on the product $|H|f$ required to limit the EF component and so to save heating selectivity of the treatment. Accordingly, a properly choice of the MF and Fe_3O_4-NPs parameters is required in order to minimize the therapeutic dose of magnetite and, at same time, save heating selectivity. Unfortunately, as shown in Sec 1.2.1.1 and 1.2.1.2, until now, this question has been faced in an unsystematic and empirical fashion.

For example, the upper bound value of the product $|H|f$ has been determined on the base of clinical trials and no on the knowledge of the actual levels of electric and magnetic powers to be dissipate in the tissues to obtain the therapeutic temperature rise inside the tumour with a desired degree of heating selectivity. The latter approaches surely would allows to weaken the constraint on $|H|f$ and consequently to reduce the therapeutic dose of magnetite to be used in MFH.

Moreover, no efforts have been addressed toward the development of applicators able to minimize the EF component with respect to the magnetic one and simultaneously to focus the radiation on the target. This aspect would allow to additionally weaken the constraint on $|H|f$.

Finally, within the constraint $|H|f \leq 4.85\times10^{8}$ A/ms, the values of MF and NPs parameters used in the experiments are chosen more on the base of experimental trials or commercial availability rather than as results of optimization procedure based on a rigours description of the problem.

In this thesis, part of the above questions have been successfully addressed, by developing a criterion that allows to determine the actual constraint on $|H|f$ and the values of NP and EMF parameters minimizing the

therapeutic dose of Fe_3O_4-NPs to be administered in MFH, given a desired degree of heating selectivity. The criterion is presented in Chapter 6.

Chapter 2

On the energy transfer between electromagnetic fields and biological nanomachines

In Chapter 1 it has been stressed that the main difficulty related to the description of the energy interaction between EMF and BNM is represented by the dimension of the BNM. Indeed, the number of atoms composing a BNM could be too small to allow a classical-macroscopic approach, and too large to make a quantum approach feasible.

However, in practically all cases of interest, as the ones considered in [5, 23], simplifying assumptions can be introduced and successfully exploited to circumvent the above difficulty:

1) The solution of BNMs is diluted;
2) The applied EMF has a wavelength, say λ, much larger than the sizes of the BNM.

In this Chapter, by exploiting the assumptions 1) and 2), it is derived a simple and accurate expression quantifying the power exchange, say P_D, between a BNM, embedded in a homogeneous lossless background medium (the solvent containing the BNMs), and the EMF.

As it will be shown, above assumptions allow a classical macroscopic description of the energy interaction and to accurately characterize the electromagnetic behaviour of the BNM, i.e. the field scattered by the BNM, by means of few parameters (the first terms of the its multipole series expansion).

The derived expression take into account the energetic exchange due to both the electric and magnetic parts of impinging EMF. As a consequence, on one hand, the expression for P_D is useful to analyse the interaction mechanism and test the hypothesis on its nature by checking the consistency with the experimental data. On the other hand, the expression is helpful at a design stage of both the BNM and the control apparatuses.

Finally, the expression for P_D is exploited to analyse the model suggested in [5] to justify the experimental results. The analysis shows that the value of

the energy absorbed by the AuNP-DNA conjugate estimated by adopting the Hamad-Schiferli's model, i.e. the Joule power dissipation caused by the currents induced on the AuNP, is many orders lower than the one required to effectively dehybridize the DNA molecule. As a consequence, to explain the reported results, other interaction mechanism should be considered.

2.1 Expression of the power dissipated by a non optical electromagnetic field on a biological nanomachine

Let us consider a BNM embedded in a homogeneous, isotropic, lossless Background Medium (BM), of electromagnetic parameters ε and μ, and let us indicate with a the radius of the smallest sphere, say $\mathcal{D}$, containing the BNM. Moreover, let us denote with ($\mathbf{E_i}$, $\mathbf{H_i}$) the EMF impinging on the BNM and with ($\mathbf{E_s}$, $\mathbf{H_s}$) the EMF scattered by the BNM. It is well known that the total EMF, ($\mathbf{E}$, $\mathbf{H}$), in the BM can be written as the superposition of the incident field ($\mathbf{E_i}$, $\mathbf{H_i}$) and of the scattered field ($\mathbf{E_s}$, $\mathbf{H_s}$) (Fig 2.1).

In the following, a Cartesian reference system (O, x_1, x_2, x_3) centred on $\mathcal{D}$ will be exploited and an exp($j\omega t$) time dependence of the EMF will be assumed and dropped, being as usual, f the frequency of the exciting signal ($\mathbf{E_i}$, $\mathbf{H_i}$) and $\omega = 2\pi f$ its angular frequency.

Before explicitly inferring the expression for P_D, let us critically discuss the simplifying assumptions to be used in the following. As stressed in the introductory part, one will exploit two hypotheses:

1) The BNMs concentration in the BM is small enough (diluted solution) to assume BNMs separated by macroscopic distances and negligible the energy exchange between BNMs;

2) The wavelength λ of ($\mathbf{E_i}$, $\mathbf{H_i}$) is much larger than the BNM-sizes.

Quantitatively, condition 1) is surely verified for BNMs concentrations up to about 10 μmol/l, corresponding to an average distance between two BNMs of about 50 nm. As a consequence, the energy interaction between the impinging EMF and each BNM can be studied as if it were an isolated BNM

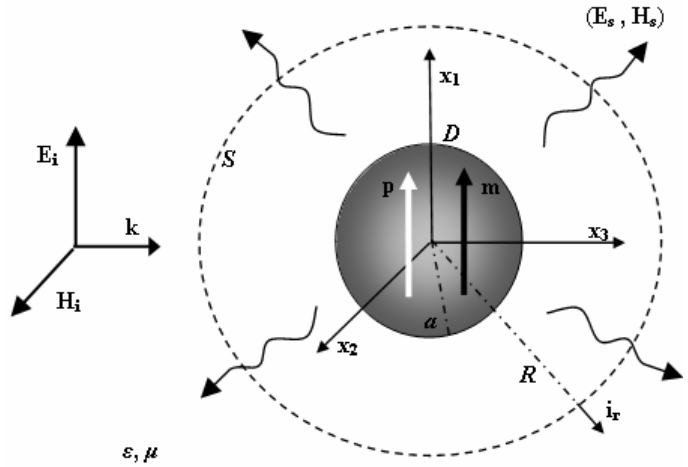

Fig 2.1. Scattering by a biological nanomachine embedded in a homogeneous isotropic background medium of electromagnetic parameters ε and μ.

in the BM. Condition 2) is satisfied up to frequencies in the range of THz when nanometer size BNMs are involved.

Now, let us turn the attention back to the expression for P_D. Since the BM is lossless, P_D can be calculated as the flux of the active power crossing a spherical surface, S, centred in O. In particular, due to the conditions 1), S can be chosen with a radius R much larger than a in order to apply a macroscopic approach. In other words, by calculating the flux of the active power on a sphere with a macroscopic radius, the representation of the field inside and in a neighbourhood of $\mathcal{D}$ is completely avoided, while (**E**, **H**) on S is governed by classical macroscopic Maxwell's equations. Accordingly, one has:

$$\begin{aligned} P_D &= -\Re\mathrm{e}\left\{\frac{1}{2}\oiint_S \mathbf{E}\times\mathbf{H}^*\cdot\mathbf{i}_\mathrm{r}\,\mathrm{d}S\right\} = \\ &-\Re\mathrm{e}\left\{\frac{1}{2}\oiint_S \mathbf{E}_\mathrm{i}\times\mathbf{H}_\mathrm{i}^*\cdot\mathbf{i}_\mathrm{r}\,\mathrm{d}S + \frac{1}{2}\oiint_S \mathbf{E}_\mathrm{s}\times\mathbf{H}_\mathrm{s}^*\cdot\mathbf{i}_\mathrm{r}\,\mathrm{d}S + \frac{1}{2}\oiint_S \left(\mathbf{E}_\mathrm{i}\times\mathbf{H}_\mathrm{s}^* + \mathbf{E}_\mathrm{s}\times\mathbf{H}_\mathrm{i}^*\right)\cdot\mathbf{i}_\mathrm{r}\,\mathrm{d}S\right\} \end{aligned} \tag{2.1}$$

where $\mathbf{i_r}$ is the radial unit vector (see Fig 2.1). The right hand of eq. (2.1) represents the flux of the Poynting's vector expressed as a function of the incident field ($\mathbf{E_i}$, $\mathbf{H_i}$) and the scattered field ($\mathbf{E_s}$, $\mathbf{H_s}$). Later on, one will denote with P_i, P_s, P_t the three flux integrals at the right hand of eq. (2.1), respectively. Obviously, due to lossless nature of BM, P_i vanishes.

According to eq. (2.1), to evaluate P_D one has to determine the expression of ($\mathbf{E_s}$, $\mathbf{H_s}$) on S. In principle, this task would require the rigorous solution of

the scattering problem. However, the assumption: $a << \lambda$, namely conditions 2), drastically simplifies the analysis. Indeed, as long as one supposes the scattered field ($\mathbf{E_s}$, $\mathbf{H_s}$) essentially equal to the one radiated by an equivalent current density distribution confined on S, the relationship $a << \lambda$, allows to express ($\mathbf{E_s}$, $\mathbf{H_s}$) in eq. (2.1) by means of the first terms only of the corresponding multipole series expansion [24]: the electric dipole, the magnetic dipole and the electric quadrupole moments. In other words, to evaluate P_D, ($\mathbf{E_s}$, $\mathbf{H_s}$) can be assumed on S as the superposition of the EMF radiated by an elementary electric dipole with moment $\mathbf{p}$, an elementary magnetic dipole with moment $\mathbf{m}$, and an elementary electric quadrupole with moment $\underline{\underline{\mathbf{Q}}}$, located at the O (Appendix A) (see Fig 2.1).

By replacing in eq. (2.1) the expressions of the EMF radiated by $\mathbf{p}$, $\mathbf{m}$ and $\underline{\underline{\mathbf{Q}}}$ and by manipulating the integrals therein, one obtains the following expression for P_D (see Appendix A):

$$\begin{aligned} P_D = {} & \Re\mathrm{e}\left\{\frac{j\omega}{2}\mathbf{E}_{\mathbf{i0}}^{*}\cdot\mathbf{p}\right\}+\Re\mathrm{e}\left\{\frac{j\omega\mu}{2}\mathbf{H}_{\mathbf{i0}}^{*}\cdot\mathbf{m}\right\}+\Re\mathrm{e}\left\{\frac{j\omega}{4}\sum_{h=1}^{3}\left(\vec{\nabla}E_{ih}^{*}(\mathbf{0})\right)\cdot\left(\underline{\underline{\mathbf{Q}}}\cdot\mathbf{i_h}\right)\right\} \\ & -\frac{vk^4|\mathbf{p}|^2}{12\pi\varepsilon}-\frac{\mu vk^4|\mathbf{m}|^2}{12\pi}-\frac{vk^6}{160\pi\varepsilon}\left(\sum_{n,h=1}^{3}|Q_{nh}|^2-\frac{1}{3}\left|\sum_{n=1}^{3}Q_{nn}\right|^2\right) \end{aligned} \tag{2.2}$$

In eq. (2.2), $j=\sqrt{-1}$, "*" denotes the complex conjugation, Q_{nh} (n, h = 1, 2, 3) is the nh-th element of $\underline{\underline{\mathbf{Q}}}$, E_{ih} and $\mathbf{i_h}$ are the components of $\mathbf{E_i}$ and the unit vectors along the x_h-direction, respectively, ($\mathbf{E_{i0}}$, $\mathbf{H_{i0}}$) is the impinging EMF at the origin O, $v = (\varepsilon\mu)^{-1/2}$ and $k = \omega(\varepsilon\mu)^{-1/2}$ is the propagation constant in the BM. In eq. (2.2), the first three terms represent the contribution of P_t to P_D, while the remaining three represent the contribution of P_s to P_D (see Appendix A).

As can be seen from eq. (2.2), P_D depends on the electromagnetic behaviour of the BNM, by means of $\mathbf{p}$, $\mathbf{m}$ and $\underline{\underline{\mathbf{Q}}}$, and on the characteristics of the exposition apparatus, by means of ($\mathbf{E_i}$, $\mathbf{H_i}$).

If linearity and isotropy are assumed for $\mathcal{D}$, $\mathbf{p}$, $\mathbf{m}$ and $\underline{\underline{\mathbf{Q}}}$ can be related to the impinging EMF as follows:

$$\mathbf{p} = \varepsilon\alpha_e\mathbf{E}_{\mathbf{i0}} \tag{2.3}$$

$$\mathbf{m} = \alpha_m\mathbf{H}_{\mathbf{i0}} \tag{2.4}$$

$$\underline{\underline{\mathbf{Q}}} = \frac{4\varepsilon}{k^2}\alpha_Q\left(\partial\mathbf{E}_{\mathbf{i0}}\right)^{S} \tag{2.5}$$

where α_e, α_m and α_Q are complex quantities depending only on the properties of BNM, and $(\partial \mathbf{E_{i0}})^S$ is the symmetric part of the matrix $\partial \mathbf{E_{i0}}$, whose h-th column is the gradient of E_{ih}, calculated at the origin O (see Appendix A).

It is worth noting that the hypotheses of linearity and isotropy introduced for $\mathcal{D}$ are quite verified if the amplitude of the impinging EMF is sufficiently small and the BNM is not strongly asymmetrical.

By substituting eqs. (2.3) to (2.5) in eq. (2.3) and noting that the trace of $(\partial \mathbf{E_{i0}})^S$ vanishes, due to the divergence-less character of $(\mathbf{E_i}, \mathbf{H_i})$, the expression for P_D becomes:

$$P_D = \frac{kv}{2}\left(\varepsilon\alpha_e''\left|\mathbf{E_{i0}}\right|^2 + \mu\alpha_m''\left|\mathbf{H_{i0}}\right|^2 + 2\varepsilon\alpha_Q''\sum_{n,h=1}^{3}\frac{1}{k^2}\left|\left(\partial E_{i0nh}^S\right)\right|^2 \right) - \frac{k^4 v}{12\pi}\left(\varepsilon\left|\alpha_e\right|^2\left|\mathbf{E_{i0}}\right|^2 + \mu\left|\alpha_m\right|^2\left|\mathbf{H_{i0}}\right|^2 + \frac{6}{5}\varepsilon\left|\alpha_Q\right|^2\sum_{n,h=1}^{3}\frac{1}{k^2}\left|\left(\partial E_{i0nh}^S\right)\right|^2 \right) \tag{2.6}$$

In eq. (2.6) α_e'', α_m'' and α_Q'' are the opposite of the imaginary parts of α_e, α_m and α_Q, respectively, and ∂E_{i0nh}^S $(n, h = 1, 2, 3)$ is the nh-th element of $(\partial \mathbf{E_{i0}})^S$.

Eq. (2.6) represents the expression to be used to evaluate the energy transfer between the applied field and BNM. One wishs to stress that in deriving eq. (2.6) no hypotheses have been formulated on the impinging EMF and on the electromagnetic and structural properties of the BNM. The only conditions to be satisfied are condition 1) and 2).

From eq. (2.6), once the expressions of α_e, α_m and α_Q are known, i.e by exploiting a model of the electromagnetic behaviour of the BNM, the electromagnetic energy transfer corresponding to the adopted model can be estimated and its reliability established by comparing the value of P_D with the experimental results. Moreover, the expression (2.6) allows the estimation of the values of α_e, α_m, α_Q and the amplitudes of the applied EMF required to obtain the energy transfer between applied field and BNM associated with an observed phenomenon. Accordingly, the obtained expression for P_D represents a useful tool to analyze the energy transfer mechanisms between the impinging EMF and BNM. Finally, once the correct mechanism is identified, eq. (2.6) can be used to design BNMs and electromagnetic control apparatuses for specific bio-medical applications.

It is must be stressed that, in principle, both $\mathbf{E_{i0}}$ and $\mathbf{H_{i0}}$ must be known to correctly evaluate P_D. As a result, it is crucial to provide an accurate electromagnetic characterization of the problem, in particular, the electromagnetic exposition equipment.

In Sec. 2.2, to show the practical usefulness of the derived expression for P_D, it is exploited to discuss the hypothesis on the energy transfer

mechanism proposed by authors in [5] to explain the experimental evidence. Obviously, at this stage one adopts exactly the model proposed in [5] to verify whether the mechanism therein suggested is able to provide a consistent description of the physics of the observed phenomena.

2.2 Energy transfer between electromagnetic field and biological nanomachine in practical applications

As discussed in Sec. 1.3, the first and, till now, the only experiments displaying the possibility to use NPs and radiofrequency EMFs to remotely control BNM, is the one described in [5].

In [5], besides the experimental results, it is also proposed a model to explain the observed phenomenon. In particular, the Author suggest that the observed DNA dehybridization is a consequence of the local heating produced, via Joule effect, by the conduction currents induced on the AuNP by the impinging EMF. However, they don't carry out any estimation of the amount of energy dissipated by AuNP, to support the consistency of their hypothesis.

In this section one exploits the expression of P_D to analyse the model proposed in [5] about the energy transfer mechanisms between the impinging EMF and AuNP-DNA conjugate.

2.2.1 The Hamad Schifferli's experiment and model

Let us first summarize the main aspects of the experiment. Concerning the experimental results, in [5] it has been observed that by putting an aqueous solution of AuNP-DNA conjugates into a RF MF, pulsed at 15 sec intervals, the absorbance UV of the solution significantly increased when MF was switched on, enlightening the DNA dehybridization. When MF was switched off the absorbance returned to its original value, indicating the DNA hybridization.

Concerning the details of the experimental setup, the DNA molecule used in [5] was a 38-nucleotide hairpin-loop DNA which is self-complementary at each end for 7 bases. The AuNPs was an uncharged gold nanocrystal with radius a of about 1nm, functionalized with a single sulfo-N-hydroxy-succinimide ester. The AuNP-DNA conjugates were dispersed in 1× PBS at a concentration of 1 μ-mol/litre. The RF MF were generated by using a coil

of 35 turns and a cross section of about 1cm, fed by an incident power of 4 watt at f = 1GHz.

As can be noted, both the conditions 1) and 2) are consistent with the experiment described in [5], so one can exploit eq. (2.5) to analyse the proposed model.

Concerning the physical mechanisms underlying the observed phenomenon, since control solutions with only DNA resulted in no changing in the absorbance with RF MF, the Authors ascribed the DNA dehybridization to the interaction between AuNP and applied MF. More specifically, they maintained that AuNP behaves in an alternating MF like a macroscopic metallic body and that the DNA dehybridization is caused by the heat produced, via Joule effect, by the conduction current induced on the AuNP by the impinging RF-MF.

Accordingly, the model therein adopted can be summarized as follows:

a) The EMF inside and in the neighbourhood of the BNM can be expressed by a classical macroscopic approach;

b) The energy transfer is due, essentially, to the presence inside the BNM of the AuNP;

c) The electromagnetic behaviour of the AuNP is assimilated to that of an isotropic metallic ball with radius $a << \lambda$.

Moreover, it is also assumed that:

d) Only a MF is present inside the coil, at f = 1GHz;

e) No dielectric losses occur in the BM (solvent).

Obviously, assumption e) is consistent with assumption d).

2.2.2 Estimation of P_D in the Hamad Schifferli's model

According to hypotheses a)-c), to evaluate α_e, α_m and α_Q, one can exploit the expressions for the polarization coefficients of a metallic ball of radius, a, much smaller than λ (see Appendix B):

$$\alpha_e \cong 4\pi a^3 \left(1 - j\frac{3\omega\varepsilon_0\varepsilon_r}{\sigma_D}\right) \tag{2.7}$$

$$\alpha_m = \frac{2\pi}{15} a^5 \omega^2 \varepsilon\mu \left(\frac{1-\varepsilon_r}{\varepsilon_r} - j\frac{\sigma_D}{\omega\varepsilon_r\varepsilon_0}\right) \tag{2.8}$$

$$\alpha_Q \cong \frac{\pi}{3} a^5 \omega^2 \varepsilon \mu \left(1 - j \frac{5}{2} \frac{\omega \varepsilon_r \varepsilon_0}{\sigma_D} \right) \tag{2.9}$$

where $\varepsilon_{0,}$ ε_r and σ_D represent the permittivity of the vacuum ($\varepsilon_0 \cong 8.85 \times 10^{-12}$ Farad/m), the relative permittivity of the BM ($\varepsilon_r \cong 81$ for the distilled water at $f = 1$ GHz) and the conductivity of $\mathcal{D}$ ($\sigma_D \cong 4.2 \times 10^7$ Siemens/m for bulk gold). Later on, it will be assumed: $\sigma_D / \omega \varepsilon_0 \varepsilon_r >> 1$ that is widely verified for the quoted values of σ_D ε_r and f.

Due to the assumption d), in eq. (2.6) one has to retain only those terms related to the MF. As a results, by replacing eqs. (2.8) in eq. (2.6) and by retaining only the lowest order terms in ka ($ka << 1$), one obtains:

$$P_D = \frac{\pi}{15} a^5 \sigma_D \left(\omega \mu \right)^2 \left| \mathbf{H_{i0}} \right|^2 \cong 50 \left| \mathbf{H_{i0}} \right|^2 \times 10^{-32} \text{ [watt]} \tag{2.10}$$

To dehybridize the used DNA molecule the energy required is, according to Zuker algorithm, about 10^{-19} J [25]. From eq. (2.10), by assuming an exposition time of 15s, as indicated in [5], the amplitude of the applied MF should be of the order of 10^5 A/m. This is not possible by using the coil described in [5], fed by input power equal to 4 watt. Accordingly, the value of the energy dissipated on the AuNP, via Joule effect, assuming the Hamad-Schifferli's model, is too small to produce the observed DNA dehybridization.

2.2.3 Some considerations on the hypotheses formulated in the Hamad Schifferli's model

The hypothesis formulated on the incident EMF, i.e. assumption d), is not realistic in that, due to the pitch of the winding of the coil, a non zero EF is present in the sample at $f = 1$GHz (see Appendix C), which can significantly contribute to P_D, as shown in eq. (2.6). Accordingly, the power exchange must be calculated by removing hypothesis d) (i.e including an EF), and retaining the other ones.

For a coil result: $|E_z| = \gamma \zeta |H_z|$, where E_z and H_z represent the components of the EMF along the axis of the coil, ζ is the characteristic impedance of the medium filling the coil and γ is a factor lesser than one (see Appendix C). Accordingly, by assuming the DNA-AuNP conjugates located on the axis of the coil and neglecting the quadrupolar contribution to P_D, one has:

$$P_D = 6\pi a^3 \frac{\left(\omega\varepsilon_0\varepsilon_r\right)^2}{\sigma_D}\left|\mathbf{E_{i0}}\right|^2 + \frac{\pi}{15}a^5\sigma_D\left(\omega\mu\right)^2\left|\mathbf{H_{i0}}\right|^2 = \left(\left(\gamma\zeta\right)^2 + 50\right)\left|H_z\right|^2 \times 10^{-32} \quad \text{[watt]} \tag{2.11}$$

Eq. (2.11) has been achieved by replacing eqs. (2.7) and (2.8) in eq. (2.6) and retaining only the lowest order terms in ka ($ka << 1$).

Note that in presence of a non zero EF a characterization of the dielectric losses of the BM is needed. However, as shown in Appendix A, the hypothesis of a lossless BM can still be exploited as long as one retains condition a) and the BM has not strong dielectric losses.
In (2.11) by ascribing to ζ the value of the distilled water and by setting γ = 1, we have:

$$P_D \le 1.8\times10^{-29}\times\left|H_z\right|^2 \ \text{[watt]} \tag{2.12}$$

From eq. (2.12), to obtain in 15s an energy transfer of 10^{-19}J required to dehybridize the used DNA molecule, the amplitude of the applied MF should be larger than about 20kA/m, again too large a value for the considered coil and input power. Therefore, even if a more accurate EMF is considered, the energy dissipated on the AuNP, via Joule effect, is again too small to produce the observed DNA dehybridization.

2.2.4 Estimation of P_D by including the quadrupolar contribution

In order to provide a more accurate estimation of the energy dissipated by the AuNP in the Hamad-Schifferli's model, P_D is estimated by including also the contribution due to the quadrupolar terms.

Denoted with P_Q this contribution, from eq. (2.6) it results:

$$P_Q = \omega\varepsilon\alpha_Q''\sum_{n,h=1}^{3}\frac{1}{k^2}\left|\left(\partial E^S_{i0nh}\right)\right|^2 - \frac{k^4 v}{10\pi}\varepsilon\left|\alpha_Q\right|^2\sum_{n,h=1}^{3}\frac{1}{k^2}\left|\left(\partial E^S_{i0nh}\right)\right|^2 \tag{2.13}$$

By exploiting the results of the electromagnetic characterization of a coil given in Appendix A, the matrix $\partial\mathbf{E_{i0}}$, evaluated along the axis of a coil, has the expression:

$$\partial\mathbf{E}_{\mathbf{i0}}(z)=\frac{\tau}{2}\begin{pmatrix} \mathrm{V}_{TM}^{i}(z) & -\mathrm{V}_{TE}^{i}(z) & 0 \\ \mathrm{V}_{TE}^{i}(z) & \mathrm{V}_{TM}^{i}(z) & 0 \\ 0 & 0 & -2\mathrm{V}_{TM}^{i}(z) \end{pmatrix} \tag{2.14}$$

where τ, $\mathrm{V}_{TE}^{i}(z)$, $\mathrm{V}_{TM}^{i[o]}(z)$, are given in Appendix A
From eq. (2.14) follows that:

$$\left(\partial\mathbf{E}_{\mathbf{i0}}\right)^{S}=\frac{\tau}{2}\begin{pmatrix} \mathrm{V}_{TM}^{i}(z) & 0 & 0 \\ 0 & \mathrm{V}_{TM}^{i}(z) & 0 \\ 0 & 0 & -2\mathrm{V}_{TM}^{i}(z) \end{pmatrix} \tag{2.15}$$

By substituting eqs. (2.9) and (2.15) in eq. (2.13) and retaining only the lowest order terms in *ka* one has:

$$P_{Q}\cong\frac{5\pi}{4}a^{5}\frac{(\omega\varepsilon)^{2}}{\sigma_{D}}\tau^{2}\left|\mathrm{V}_{TM}^{i}(z)\right|^{2}\le\frac{5\pi}{4}a^{5}\frac{(\omega\varepsilon)^{2}}{\sigma_{D}}\tau^{2}\left|\mathrm{V}_{TM}^{i}(z)\right|_{\max}^{2} \tag{2.16}$$

Since $\mathrm{V}_{TM}^{i[o]}(z)$ satisfy the equations of the transmission lines, it follows that:

$$\tau^{2}\left|\mathrm{V}_{TM}^{i}(z)\right|_{\max}^{2}=\tau^{2}Z_{TM}^{2}\left|\mathrm{I}_{TM}^{i}(z)\right|_{\max}^{2}=\tau^{2}\frac{\tau^{2}+k^{2}}{(\omega\varepsilon)^{2}}\left|\mathrm{I}_{TM}^{i}(z)\right|_{\max}^{2} \tag{2.17}$$

(obviously, it is assumed the transmission line without losses).
Moreover, along the axis of a coil it results (see Appendix C):

$$\frac{\tau^{2}}{(\omega\varepsilon)^{2}}\left|\mathrm{I}_{TM}^{i}(z)\right|_{\max}^{2}=\left|E_{z}\right|_{\max}^{2}=\gamma^{2}\frac{\mu}{\varepsilon}\left|H_{z}\right|_{\max}^{2}\le\frac{\mu}{\varepsilon}\left|H_{z}\right|_{\max}^{2} \tag{2.18}$$

By replacing eq. (2.17) and (2.18) in eq. (2.16) and setting $\tau\approx 205.1$ m^{-1} (see Appendix C), one obtains:

$$\begin{aligned} P_{Q}\le\frac{5\pi}{4}a^{5}\frac{(\omega\varepsilon)^{2}}{\sigma_{D}}\tau^{2}\left|\mathrm{V}_{TM}^{i}(z)\right|_{\max}^{2}\le \\ \frac{5\pi}{4}a^{5}\frac{k^{2}}{\sigma_{D}}\left(\tau^{2}+k^{2}\right)\left|H_{z}\right|_{\max}^{2}\cong 1.7\left|H_{z}\right|_{\max}^{2}\times 10^{-45}\ \text{[watt]} \end{aligned} \tag{2.19}$$

As can be seen from eq. (2.19), the contribution to P_D due to the quadrupolar moment is negligible as compared with the contribution to P_D due to dipolar moments (see eq. (2.12)). Therefore, even if the contribution of the quadrupolar moment is considered, the energy dissipated on the AuNP, via Joule effect, is again too small to produce the observed DNA dehybridization. Accordingly, the phenomenon observed cannot be ascribed to local heating produced by the conduction currents induced by the applied field inside the AuNP, even if a non zero EF acts on the AuNP.

Accordingly, one can conclude that a different modelling of the physical system, reconsidering hypotheses b) and c) as well as the mechanisms describing energy balance of the whole NM and of its subsystems, should possibly be adopted to explain the experimental results.

2.3 Conclusions

In this Chapter a simple expression of the power absorbed by a BNM subjected to a non-optical EMF has been derived. The obtained expression represents an useful tool to analyze the energy transfer mechanisms between applied field and BNM. Moreover, since in many cases the functions of the biologically active part can be driven by means of a simple energy transfer, such expression is very useful in designing remotely controlled BNMs and the relative control equipments, for bio-medical applications.

Finally, the obtained expression have been applied to analyze the energy transfer mechanism proposed to explain the first and only experimental results on the use of NPs and RF EMFs to remotely control BNM: the Hamad-Schifferli's experiment [5].

The analysis has shown that the model proposed in [5] to justify the experimental results, i.e. the local heating produced via Joule effect by the conduction currents induced on the AuNP, is not maintainable because the corresponding energy transfer is many orders lower than the one required to effectively dehybridize the DNA molecule. As a consequence, to explain the reported results, other mechanisms should be taken in account. Furthermore, a more accurate electromagnetic characterization of the experiment, in particular of the exposition apparatus and the BM, should be provided in order to be sure that only local energy transfer mechanisms are involved in the observed phenomenon.

Chapter 3

Magnetic nanoparticles

The analysis carried out in Chapter 2 has shown that the energy transfer mechanism proposed in [5] to justify the observed DNA-dehybridization, i.e. the heating produced via Joule effect by the conduction currents induced on AuNP attached to DNA, is not acceptable in that the corresponding amount of energy dissipated is too small to effectively denaturate the used DNA. This result makes questionable the possibility of using AuNPs to remotely control BNMs by means of RF EMFs. Therefore, the attention has been turned to MNPs, which seem to have such potentialities as suggested by their application in anticancer magnetic hyperthermia (see Chapter 6).

MNPs are small clusters of atoms of magnetic material (tipically ferromagnetic or ferrimagnetic) coated with functionalizing polymers.
They are usually supplied as FerroFluid (FF), i.e. stable colloidal suspension of MNPs dispersed in carrier liquid (solvent).
FFs are of interest in that allow:

- the investigation of the physical properties of the suspended MNPs;
- the biomedical applications of MNPs, when the solvent is biocompatible.

Like gold NPs, MNPs have size comparable with those of the bio-macromolecules and can be coated with biocompatible polymers that allow their linking to bio-macromolecules. In addition, they have some features that makes them particularly attractive in biomedical applications:

1) High sensitivity to an applied RF-MF;
2) Capability to absorb an amount of energy from an applied MF, large enough to control the activities of the most of bio-macromolecules.

Characteristics 1) is of interest due to the low interaction of the biological tissues with an applied RF-MF. Characteristic 2) is appealing since makes them promising candidates to remotely control BNMs.

Moreover, for MNPs the interaction mechanisms with the MF have been already understood and embodied in theoretical models of sufficient accuracy and simplicity.

In this Chapter one presents and analyzes the main mechanisms of interaction between MF and MNPs in suspension (FF) together with the theoretical models developed to describe their dependence on the physical parameters of MNPs and some interesting experimental data, reported in literature, on the magnetic properties of FFs. The aim is to establish the applicability of MNPs in biomedical applications and to derive analytical tools for designing MNPs and exposition apparatuses, for biomedical applications.

3.1 Mechanisms of interaction with a magnetic field

In this section are presented the main mechanisms of interaction between MNPs in suspension (FF) and applied MF together with the theoretical models developed to describe their dependence on the physical parameters of the system (i.e. amplitude and frequency of the applied MF, nature of the solvent, MNP-concentration, MNP-size, nature of the magnetic material composing the MNP, temperature of the FF, etc.)

3.1.1 Magnetism in matter

The magnetic properties of matter are a consequence of the existence of atomic magnetic dipoles, which arise from both the orbital motion of the electrons and their spin moments.

Although atoms can have a permanent non-zero magnetic dipole, in absence of an applied MF, the net magnetic moment of a macroscopic assembly of non interacting atoms is zero because of the action of thermal agitation that tends to orient the atomic moments in random fashion (see Fig. 3.1a). However, the net magnetic moment can be changed by putting the assembly into an external MF. For a material with non interacting dipole, denoted with **H** the applied MF and the and **M** the net magnetization (i.e. the net dipole moment per unit volume), provided that the amplitude of **H** is small enough to avoid saturation phenomena, it results: $\mathbf{M} = \chi\mathbf{H}$ where χ is the magnetic susceptibility of the material.

Depending on the sign of χ, positive or negative, such materials are classified in *paramagnetics* and *diamagnetics*.

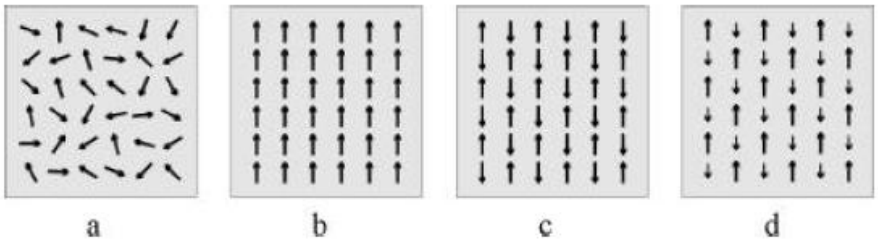

Fig. 3.1. Dipole orientation in four type of magnetic material: a) paramagnet; b) ferromagnet; c) antiferromagnet; d) ferrimagnet.

The sign of χ can be positive or negative in consequence of two different mechanism of magnetization of an atom in an external MF: spin-moment orientation and Larmor's precession of the orbital angular moments of the electron. The spin-moment orientation is caused by the mechanical torque exerts by MF on the spin moment. This mechanism produce a parallel alignment of the atomic dipole in direction of the field and consequently a net magnetization parallel to the field orientation. Therefore, the contribution to χ due to the spin-moment orientation is positive.

An external MF induce also the precession (Larmor's precession) of the orbital angular moment of the electrons around the field direction. Since this precession is always in an anti-clockwise direction with respect to the field orientation, it produce an induced magnetic dipole opposite to the MF direction and hence a net magnetization anti-parallel to the field orientation. Therefore, the contribution to χ due to the Larmor's precession is negative.

It is worth noting that the latter mechanism is present in all atoms, whereas the spin-orientation, for the Pauli's law, is present only in atoms with a permanent dipole, i.e. with unpaired spins in the electron shells. However, the intensity of magnetization produced by the spin orientation is much larger than the one due to the Larmor's precession of the orbital angular moments of electrons. As a result, a material displays a paramagnetic behaviour if its atoms exhibit permanent dipoles (i.e. unpaired spins in the electron shells). On the contrary, a material is diamagnetic if its atoms do not have permanent dipoles.

The results above described referred to a substances with non interacting magnetic dipoles. However, in some materials strong dipole-dipole interactions, of quantum-mechanical origin, there exist that produce long-range correlations between the orientations of atomic dipoles. Depending on the type of alignment between neighbouring dipoles, such material are classified in *ferromagnets*, *antiferromagnets* and *ferrimagnets*.

Are FerroMagnetics (FM) all materials for which dipolar interactions favour parallel alignment of the dipoles (see Fig. 3.1b). This materials are

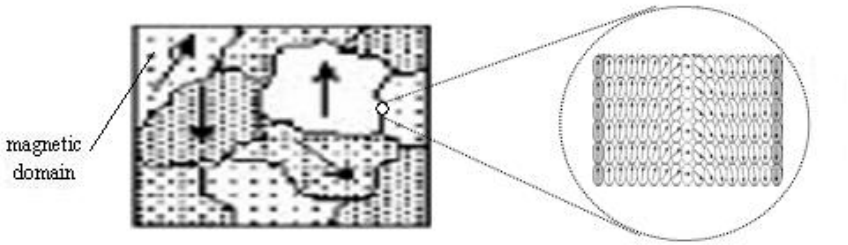

Fig. 3.2. Magnetic domains in a ferromagnetic material.

characterized by a non null net magnetization even in the absence of an external field. However, above the so-called Curie temperature, which is material-dependent, the dipolar ordering inside a ferromagnet is lost and the material becomes a paramagnet.

Antiferromagnetics, instead, are characterized by an anti-parallel alignment of neighbouring dipoles (see Fig. 3.1c). Therefore, for this class of substances no macroscopic magnetization is observed in absence of an applied external MF.

Finally, FerriMagnetics (FM) are similar to antiferromagnets, with anti-parallel arrangement of neighboring dipoles, but the number (or magnitude) of dipoles pointing in one direction differs from the number (or magnitude) pointing in the opposite direction (see Fig. 3.1d). Thus, like ferromagnets, the net magnetization in absence of an external MF is different from zero. Obviously, Due to partial cancellation of dipole moments, the magnetization of ferrimagnets is generally lower than that of ferromagnets.

The dipole ordering previously described does not extend over the entire volume of a macroscopic sample but is limited to micrometric regions, referred to as *magnetic domains* or *Weiss domain* (see Fig. 3.2), which have different orientations. The transition between two adjacent domains with different orientation takes place by means of narrow regions called *domain wall* or *Bloch walls*, wherein the atomic dipoles change their orientation (see Fig. 3.2).

Although each domain is uniformly magnetized, with a magnetization close to the saturation magnetization M_s, in absence of an applied external MF, the different orientation of the magnetic domain makes the net magnetization of the sample negligible. However, due to high capability of the magnetic domain to change their orientation or size in response to an external MF, it is sufficient to apply a small MF, H, to produce a intense magnetization, M, of the sample. As a result, ferromagnets and ferrimagnets are characterized by a strong H-M response, which is non-linear and dispersive.

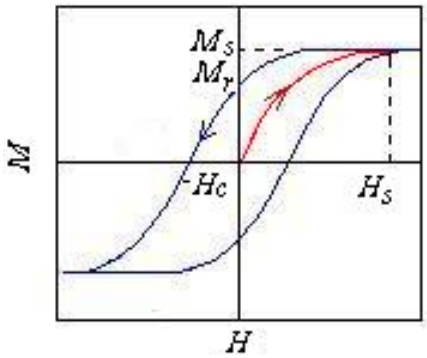

Fig. 3.3. *H-M* diagram for a ferromagnetic material: hysteresis loop.

In Fig. 3.3 it is shown the typical *H-M* diagram for a ferromagnetic material. From a physical viewpoint, the curve plotted in Fig. 3.3 can be justified as follows. By increasing the MF-intensity, magnetic domains oriented in the field direction grow while magnetic domain oriented in opposite direction to the field reduce (domain wall motion). This phenomenon produces an enhancement of M with H according to the red curve in Fig. 3.3 if the initial magnetization of the sample is zero. Next, by reducing the field intensity, M does not follows the red path, but decrease more slowly and when H approaches zero $M = M_r \neq 0$.The phenomenon of remanence (M_r) is caused by defects of the crystal lattice that prevent the magnetic domain from reaching their initial dimensions once the MF is removed. (magnetic domain pinning). To cancel M_r it is needed to apply a MF in opposite direction to M_r and of amplitude H_c (see Fig. 3.3), where H_c represents the coercivity of the FM material.

The hysteretic behaviour of the FM materials above described produce within the FM sample a magnetic power dissipation proportional, for a complete loop, to the area bounded by the hysteresis loop.

3.1.2 Nanomagnetism

The physical properties of FM materials drastically changes when the sample-size becomes of the order of nanometres (*nanomagnetism*).

Although the transition between the FM behaviour and nano-magnetism is not of threshold type it is possible to identify the S*ingle-Domain Radius* (SDR) as the borderline between the two different behaviours. SDR is the size below which the gain in magnetostatic energy due to domain formation is smaller than the domain-wall energy. Therefore, FM materials of size smaller than SDR display a Single Domain (SD) state and an uniform magnetization in the direction of the FM crystal axis [26-27].

Typically, SDR range from tens nanometer to hundredths nanometer depending on the nature of FM materials. Indeed, the value SDR is strongly geometry-dependent.
For a spherical-geometry it can be proved that [27]:

$$\mathrm{SDR} = \frac{36\sqrt{AK_a}}{\mu_0 M_s^2} \tag{3.1}$$

where A and K_a the quantities depending on the FM material [27].

FM materials of spheroidal shape and size smaller than SDR are commonly called SD MNP. Being in a SD state, SD MNP exhibit an uniform magnetization with $M = M_s$. As a consequence, each SD MNP has a permanent magnetic dipole of magnitude $m = M_s V_m$ [27], where V_m is the magnetic volume of the MNP

As a concluding remark, it is worth noting that for very small MNP the value of M_s is smaller than the saturation magnetization of bulk material composing MNPs. This effect is a consequence of the spin disorder arising at the surface of MNP, which, due to the large value of the surface-volume ratio, becomes important at nanometer scale.

Later on, we will refer to the only SD MNP, therefore, we will omit the acronym SD, if it is not strictly needed.

3.1.3 Anisotropy of the magnetic nanoparticles

The behaviour of a suspended MNP in an external MF is determined not only by its magnetic moment, **m**, but also by its magnetic anisotropy that tends to align **m** along preferred directions referred to as *axes of easy magnetization* or *easy axes* [26-27].

Generally, the anisotropy of a MNP consists of three contributions: a magneto-crystalline anisotropy associated to the crystal lattice of the FM material composing MNP, shape anisotropy due to the geometry of the MNPs and an surface anisotropy caused by the spin disorder at the surface of MNP [26-29].

In the case of uniaxial anisotropy, the energy of **m** in an external applied MF, **H**, is given by [26, 30-31]:

$$U = -\mu_0 \mathbf{m} \cdot \mathbf{H} - K_a V_m \left(\mathbf{i_e} \cdot \mathbf{i_n}\right)^2 \tag{3.2}$$

where $\mathbf{i_e}$ and $\mathbf{i_n}$ are the unit vectors along the directions of **m** and the easy axis, respectively, and K_a is the anisotropy constant. Accordingly, the effective magnetic field acting on **m** is given by [26]:

$$-\frac{1}{\mu_0}\frac{\partial U}{\partial \mathbf{m}} = \mathbf{H} + \frac{2K_a}{\mu_0 M_s}\left(\mathbf{i_e}\cdot\mathbf{i_n}\right)\mathbf{i_n} = \mathbf{H} + \mathbf{H_a} \tag{3.3}$$

As can be seen from eq. (3.3), the effect of the anisotropy on **m** is the same of a static MF, $\mathbf{H_a}$, applied along the easy axis and of amplitude:

$$H_a = \frac{2K_a}{\mu_0 M_s}\left(\mathbf{i_e}\cdot\mathbf{i_n}\right) \tag{3.4}$$

3.1.4 Superparamagnetism

Although the effect of anisotropy is to keep **m** along the easy axis, at equilibrium and in absence of an external MF, **m** is not aligned along the easy axis, but fluctuates inside the MNP subjected to the thermal agitation. Accordingly, a MNP can spontaneously reverse its magnetization in response to the thermal agitation.

For uniaxial anisotropy, the frequency at which the spontaneous magnetization reversal occurs is given by [26, 28, 32-33]:

$$f_N = \frac{1}{\tau_0}\exp\left(-\sigma\right) \tag{3.5}$$

where τ_0 is a characteristic time whose value depends on the FM material composing the MNP (τ_0 is given in eq. (3.18)), $\sigma = K_a V_m/k_B T$, k_B is the Boltzmann constant ($k_B = 1.38\times10^{-23}$ J/K) and T is the absolute temperature.

From eq. (3.5) it follows that for an assembly of MNP such that $\sigma >> 1$, i.e. characterized by a large value of $K_a V_m$, **m** results practically blocked along the easy axis [26]. Thus, the only way to reverse the magnetization is to apply an external MF, **H**, opposite to **m** and of amplitude H_a. Accordingly, a such assembly has a *M-H* diagram like that shown in Fig. 3.4a, i.e. an hysteretic profile with $M_r \approx M_s$ and $H_c \approx H_a$ [26-27].

On the contrary, for an assembly of MNP such that $\sigma << 1$, i.e. characterized by a small value of $K_a V_m$, **m** is free to fluctuates inside the MNP in response to the thermal agitation. Therefore, a such assembly behaves in an external MF like a paramagnetic substance, but the magnetic moments are those of MNPs, which are about four orders in magnitude larger than atomic moment (*superparamagnetism* [26-28, 33-37]). As a result, the assembly has a *M-H* diagram like that shown in Fig. 3.4b, i.e. a

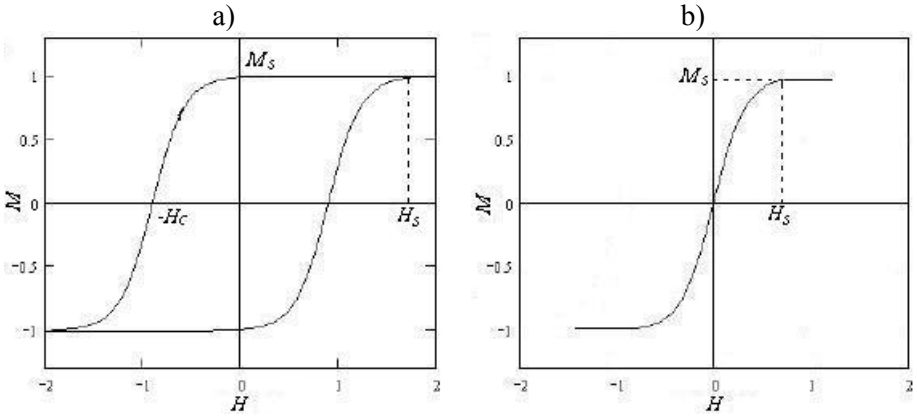

Fig. 3.4. a) *H-M* diagram for an assembly of blocked MNPs; b) *H-M* diagram for an assembly of superparamagnetic MNPs.

unhysteretic profile with no remanence ($M_r \approx 0$) and coercivity ($H_c \approx 0$) [26-28, 33-37].

As a concluding remark, it should be noted that the observation of the superparamagnetism depends, besides the value of anisotropy energy $K_a V_m$, also on the observation time τ_{oss}. In particular, if $\tau_{oss} << 1/f_N$ the magnetic moment appears blocked along the easy axis. In contrast, if $\tau_{oss} >> 1/f_N$ the MNP appears superparamagnetics.

3.1.5 Ferrofluids

FFs are stable suspension of SD MNP dispersed in liquids (solvent). The nature of the solvent depends on the applications of FFs (for biomedical applications the solvent is water).

To make MNPs soluble in liquids, they are coated with a thin layer of polymers, whose chemical composition changes according to the nature of the solvent. Therefore, MNPs dispersed in FFs consist of a magnetic core, of diameter d_m, and of a coating, of thickness δ.

A stable FF requires not only the solubility of MNP in the carrier liquid, but also the absence of NP-aggregation. If it is assumed that the magnetic dipole-dipole interaction is the main cause of aggregation, then the condition of non agglomeration is [26]:

$$\frac{E_{dd}}{E_T} = \frac{\mu_0 m^2}{2\pi (d_m + 2\delta)^3 k_B T} = \frac{\pi}{72} \frac{\mu_0 M_s^2 d_m^6}{(d_m + 2\delta)^3 k_B T} < 1 \qquad (3.6)$$

where E_{dd} is the magnetostatic energy of the system consisting of two aggregated MNPs with anti-parallel magnetic moments, $E_T = k_B T$ is the thermal energy and $d_m + 2\delta$ is the hydrodynamic diameter of MNPs. Eq. (3.6) imposes that the thermal energy is larger than the magnetostatic energy of the system consisting of two aggregated MNPs so that the only thermal agitation is sufficient to prevent aggregations.

By solving the inequality (3.6) with respect to d_m we obtain a maximum value for d_m that represents the maximum size of the magnetic core below which the MNP-agglomeration is prevented. As can be noted, this value depends on the nature of the FM material composing MNPs and on the coating-thickness.

Typically, the size of dispersed MNPs ranges from few nanometres (about 5-6 nm) to tens of nanometer (40-50nm).

3.1.5.1 Equilibrium magnetization of a ferrofluid

A FF, consisting of SD MNPs, behaves in an applied, static (dc), MF like a polar fluids, in which the orientation of dipole moments along the field direction is counteracted by the action of the thermal agitation. Therefore, in absence of an applied MF a no net magnetization is observed in FFs because of the random orientation of MNP-moments, due to the thermal agitation. However, as soon as a MF is applied a net magnetization arises in the MF direction, due to moment orientation. Obviously, the magnetization does not reach the saturation because of the thermal agitation that tends to destroy the magnetic moment ordering induced by the applied dc MF.

The behaviour just described is exhibited in both cases of blocked and superparamagnetic MNPs with the difference that for blocked MNPs the orientation of **m** takes place by means of a mechanical rotation of the whole MNP inside the solvent, while for superparamagnetic MNPs the orientation of **m** takes place inside MNPs.

Although the phenomenon of magnetization for a FF is very similar to the one for a paramagnetic gas, the classical Langevin's theory developed to explain the paramagnetism, in general, cannot be exploited to describe the FF-magnetization in that it does not take in account the effects due to the anisotropy field $\mathbf{H_a}$ acting on each MNP.

However, for FFs consisting of non interacting MNPs, with uniaxial anisotropy, and free to rotate in the solvent (i.e. for FFs with moderate MNP-concentration and temperature above the melting point), the equilibrium magnetization can be still described by the classical Langevin's theory for the paramagnetism [38]. Physically, this result can be explained as follows. In presence of an applied dc MF the magnetic moments of MNPs tend to

align along the field direction. The anisotropy tends to align the easy axes along the direction of magnetic moments and this second alignment has no effect on the moment-orientation.

Accordingly, the equilibrium magnetization of such FFs can be described by the following formula [38]:

$$M = nm\left(\coth\left(\frac{\mu_0 mH}{k_B \mathrm{T}} \right) - \frac{k_B \mathrm{T}}{\mu_0 mH} \right) = M_\infty \mathcal{L}\left(\frac{\mu_0 mH}{k_B \mathrm{T}} \right) \tag{3.7}$$

where n is the number of MNPs per meter (MNP-concentration), M_∞ the saturation magnetization of the FF and $\mathcal{L}(\cdot)$ the Langevin function. As a result, a FF has a M-H diagram like that shown in Fig. 3.4b, i.e. a unhysteretic profile with no remanence ($M_r \approx 0$) and coercivity ($H_c \approx 0$).

Formula (3.7) holds for monodisperse(*) FFs. For polydisperse FFs, characterized by a distribution-size $g(\cdot)$, the expression for the equilibrium magnetization it is obtained by averaging the formula (3.7), i.e.:

$$M = \int M_\infty \mathcal{L}\left(\frac{4\pi\mu_0 M_s H}{3k_B \mathrm{T}} r_m^3 \right) g\left(r_m\right) \mathrm{d}r_m \tag{3.8}$$

where r_m is the magnetic radius of suspended MNPs.
From eq. (3.7) it follows that:

$$M_\infty = nm = nV_m M_s \qquad \Rightarrow \qquad \frac{M_\infty}{M_s} = nV_m = c \tag{3.9}$$

where c is the volumetric concentration of dispersed FM material.

Generally, in experiments involving FFs, typical temperatures and fields are such that $\mu_0 mH/k_B\mathrm{T} << 1$. Thus, eq. (3.7) becomes:

$$M \cong \frac{\mu_0 nm^2}{3k_B \mathrm{T}} H = c \frac{\mu_0 V_m M_s^2}{3k_B \mathrm{T}} H = \chi_0 H \tag{3.10}$$

where χ_0 is a quantity depending only on the physical characteristics of FF, refers to as static susceptibility [26, 34, 37] of the FF. Accordingly, for small values of the ratio $\mu_0 mH/k_B\mathrm{T}$, the equilibrium magnetization of a FF depends

(*) the term "monodisperse" is used to indicate FFs containing MNPs of the same size and shape. In contrast the term "polydisperse" is used indicate FFs characterized by a MNP-size distribution.

linearly on the MF-amplitude. In other words, as long as H is small enough to prevent saturation phenomena, FFs behave as linear system.

Finally, we note that eqs. (3.19) and (3.10) hold also for a polydisperse FF. In this case V_m represents the mean magnetic volume of the suspended MNPs.

3.1.5.2 Relaxation mechanisms in a ferrofluid

The magnetization of a FF, after an applied dc MF has been removed, decays due to the thermal agitation that tends to reorient the magnetic moments of MNPs in random fashion.

In a FF, at temperature above the melting point, the orientation of magnetic moments can take place through both a mechanical motion of MNPs in the carrier liquid and a rotation of **m** inside MNPs. Accordingly, in a FF one can distinguish two different relaxation mechanisms: *Brownian relaxation* [29, 39-49], due to the mechanical rotation of MNPs in the solvent, and *Néel relaxation* [30, 32-33, 42, 50-58] due to the fluctuation of **m** inside MNPs.

Obviously, because of inertial and frictional effects acting on **m**, the magnetization decay of a FF is not instantaneously but characterized by a *relaxation time*.

For Brownian relaxation, this characteristic time, referred to as Brownian relaxation time, τ_B, is given by [29, 39-49]:

$$\tau_B = \frac{3\eta V_h}{k_B \mathrm{T}} = \frac{3\eta}{K_a}\left(1+\frac{2\delta}{d_m}\right)^3 \sigma \tag{3.11}$$

where η is the dynamic viscosity of the solvent and V_h, the hydrodynamic volume of MNPs. As can be noted from eq. (3.11), τ_B depends on the nature of the solvent and on the hydrodynamic size of MNPs and is independent of the magnetic properties of MNPs (i.e. K_a, M_s, d_m, etc.).

Concerning the Néel relaxation time, τ_N, a semi-empirical expression for τ_N is: $\tau_N = 1/f_N$ where f_N is given in eq. (3.5). However, this expression is unsuitable to describe τ_N when σ approaches zero (i.e. when d_m approaches zero) because it predicts a non-zero value of τ_N, which is in strong contrast with the physical evidence. The exact expression for τ_N is the one obtained analytically by Brown, for small and large value of σ [50, 52]:

$$\tau_N = \begin{cases} \frac{\sqrt{\pi}}{2}\tau_0\sigma^{-1/2}\exp(\sigma) & \sigma \gg 1 \\ \tau_0\sigma(1+0.4\sigma) & \sigma \ll 1 \end{cases} \tag{3.12}$$

where τ_0 is a characteristic time whose expression is given in eq (3.18). However, although eq. (3.12) provide the exact expression for τ_N, it does not allow to evaluate τ_N for $\sigma \sim 1$.

Expressions of τ_N valid for a continuous range of values of σ are the ones developed, by fitting the Brown's expression (3.12), by Bessais [30, 32, 52]:

$$\tau_N = \tau_0 \frac{\sigma}{(1+0.25\sigma)^{5/2}} \operatorname{epx}(\sigma) \tag{3.13}$$

Aharoni [30, 33, 52]:

$$\tau_N = \tau_0 \frac{\sigma(2+\sigma)^{3/2}}{\left(2+\frac{9}{5}\sigma+\left(\frac{4}{\pi}\right)^{1/3}\sigma^2\right)^{3/2}} \operatorname{epx}(\sigma) \tag{3.14}$$

and Coffey [59]:

$$\tau_N = \tau_0 \frac{\operatorname{epx}(\sigma)-1}{\left(\frac{2\sigma}{\sigma+1}\sqrt{\frac{\sigma}{\pi}}+2^{-\sigma}\right)} \tag{3.15}$$

As a matter of fact, only the expressions (3.14) and (3.15) exhibit the correct behaviour for $\sigma << 1$ e $\sigma >> 1$ (see eq. (3.12)). Moreover, the comparison between the expressions (3.14) and (3.15) reported in [59] shows that eq. (3.15) is a better approximation of the actual behaviour of τ_N than eq. (3.14). Accordingly, the expression for τ_N to be used is eq. (3.15).

One wishes to stress that τ_N depends on the magnetic properties of MNPs, band is independent of the nature of the solvent. Moreover, due to the exponential dependence of τ_N on σ, small change in MNP-size results in strong variation of τ_N, hence of the dynamic response of a FF.

Since Brownian and Néel relaxations act simultaneously on the magnetization decay of a FF, the effective relaxation times, τ_{eff}, is given by [26, 35-36, 40, 44]:

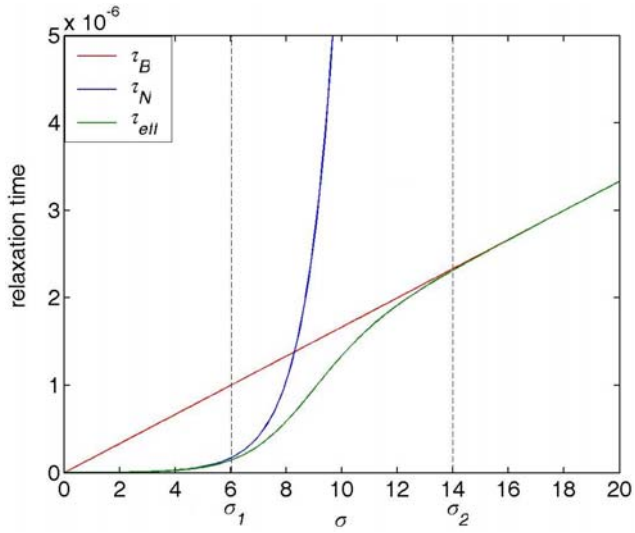

Fig. 3.5. theoretical profile versus σ of the Brownian, Néel and effective relaxation times of a suspension of magnetite nanoparticles of 10 nm in size and dispersed in water.

$$\tau_{eff} = \frac{\tau_N \tau_B}{\tau_N + \tau_B} \tag{3.16}$$

From eq. (3.16) it can be easily proved that $|\tau_N - \tau_{eff}| \lesseqgtr |\tau_B - \tau_{eff}|$ for $\tau_N \lesseqgtr \tau_B$. In particular, it result that: $\tau_{eff} \cong \tau_N$ for $\tau_N << \tau_B$ and $\tau_{eff} \cong \tau_B$ for $\tau_B << \tau_N$. According to the above relations, the dominant relaxation mechanism in a FF is the one with the shortest relaxation time. Physically, condition $\tau_N << \tau_B$ occurs when the internal fluctuation of **m** is faster than the mechanical rotation of MNP in the solvent, i.e. when **m** is free to rotate inside MNP (superparamagnetic NPs). On the contrary, condition $\tau_B << \tau_N$ occurs when the internal fluctuation of **m** is slower than the mechanical rotation of MNP in the solvent, i.e. when **m** is fixed along the easy axis (blocked MNPs). Accordingly, for FFs with superparamagnetic NPs the actual relaxation mechanism is the Néel one, while for FFs with blocked MNPs the actual relaxation mechanism is the Brownian one.

Fig. 3.5 shows the theoretical profiles of τ_B, τ_N and τ_{eff} versus σ, obtained by exploiting eqs (3.11), (3.15) and (3.16) and assuming: d_m = 10 nm, δ = 0 nm, $\eta = 10^{-3}$ Ns/m^2 (water), M_s = 318.3 kA/m, K_a = 18 kJ/m^3, $\tau_0 = 10^{-9}$ s (magnetite NPs). As can be noted, it is possible to identify two regions of values of σ : $\sigma < \sigma_1$ wherein $\tau_{eff} \cong \tau_N$, and hence MNPs relax through the Néel

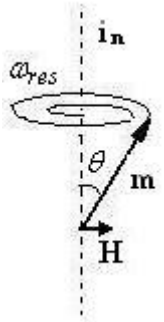

Fig. 3.6. Larmor's precession of the dipole moment, **m**, of a magnetic nanoparticle around the axis of easy magnetization $\mathbf{i_n}$.

relaxation, and $\sigma > \sigma_2$ wherein $\tau_{eff} \cong \tau_B$ and hence MNPs relax through the Brownian relaxation. Accordingly, fixed the physical characteristics of a FF (nature of the solvent and FM material composing MNPs), σ_1 and σ_2 individuate two values of d_m, say d_{m1} and d_{m2}, representing MNP-sizes respectively below which MNPs in suspension exhibit a superparamagnetic behavior and above which MNPs in suspension are magnetically blocked.
For $\sigma_1 < \sigma < \sigma_2$ both Néel and Brownian relaxations are important for the magnetization decay.

3.1.5.3 Ferromagnetic resonance in a ferrofluid

Besides the relaxation mechanisms, the magnetization of a FF can change due to the phenomenon of *ferromagnetic resonance* [26, 29, 60-69]. The physical mechanism underlying the ferromagnetic resonance is the Larmor's precession of **m** about the easy axis (see Fig. 3.6), arising when **m** deviates from easy axis direction.

For MNPs with uniaxial anisotropy and for small value of the polar angle, θ, between the easy axis and **m** (see Fig. 3.6), the angular frequency of the precession is given by [26, 29, 60-69]:

$$\omega_{res} = \gamma H_a \cong \gamma \frac{2K_a}{\mu_0 M_s} \tag{3.17}$$

where γ is the giromagnetic ratio ($\gamma \approx 2.21 \times 10^5$m/As [63]).
Obviously, the precession is damped because of the *magnetic friction* that **m** experiences when rotating inside MNP. The damping time of the precession of **m** about the easy axis is given by [63]:

$$\tau_0 = \left(\alpha\omega_{res}\right)^{-1} = \frac{\mu_0 M_s}{2\alpha\gamma K_a} \tag{3.18}$$

Typical value of the damping coefficient, α, ranges from 0.01 to 0.1 [63] (α è is dimensionless).

In presence of an external dc MF, of amplitude H applied to MNPs and parallel to the anisotropy field, the expression of the resonance angular frequency changes in agreement with the following formula [26, 29, 60-69]:

$$\omega_{res} = \gamma\left(H + H_a\right) \tag{3.19}$$

Finally, we want to underline that ω_{res} depends on the anisotropy constant K_a and saturation magnetization M_s and is independent of the MNP-size, as it is can be noted by looking eq. (3.17).
In the most of FM material, the ferromagnetic resonances occurs at GHz frequencies.

3.1.5.4 Dynamic susceptibility of a ferrofluid

In Sec. 3.5.1.1 it has been noted that, as long as the amplitude of the applied MF is small enough to avoid saturation phenomena, a FF behaves as a linear system. Therefore, the magnetization dynamic of a FF, in a weak, time-varying, MF is completely described by its *step-function response* $f_\chi(t)$ or equivalently by its *magnetic susceptibility* $\chi(\omega)$, which is related to step-function response by a Fourier transformation.

As a matter of fact, the magnetization dynamic of a FF is nearly always described in terms of $\chi(\omega)$ in that frequency-domain measurements are easier to perform than the time-domain measurements. In addition, the knowledge of $\chi(\omega)$ allows to straightforwardly evaluate the magnetization response of a FF in an applied, oscillating, (ac) MF operating at the angular frequency ω.
Generally, a way to provide $\chi(\omega)$ of a FF is to directly measure it. However, the understanding of the physical mechanisms underlying the dynamic behaviour of FFs (i.e. relaxation mechanisms and ferromagnetic resonance) has led to the development of theoretical models that allow to derive $\chi(\omega)$, in a broad frequency range, from the knowledge of only the physical parameters of the FF.

These models, although approximated, are of great interest because they allow to predict the frequency behaviour of a FF without directly measuring $\chi(\omega)$. Furthermore, they represent useful tools to design FFs with a desired

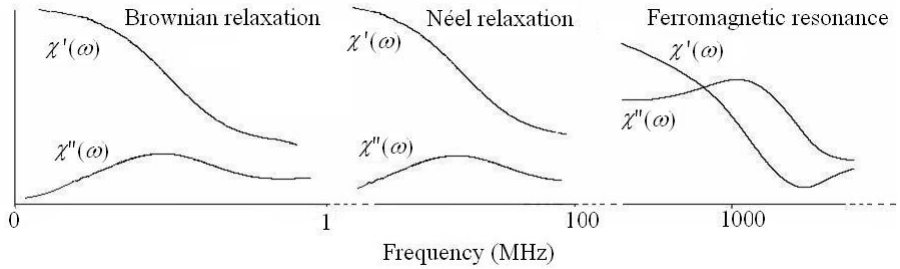

Fig. 3.7. Typical frequency response of a suspension of polydisperse magnetic nanoparticles. For each frequency region it is indicated the main mechanisms of magnetization decay.

frequency behaviour. In fact, these models allow to individuate the physical characteristics suspended MNPs must have in order that the FF exhibit a desired frequency-response. For instance, in the biomedical applications of MNPs, such as the remotely control of biological nanomachines, it is required that MNPs absorb a sufficient amount energy from the applied MF, in a frequency range biologically tolerable.

In the following, we will present the above-quoted models, i.e. the analytical expression for $\chi(\omega)$ in terms of FF-parameters.

Firstly we note that because of the different nature of the mechanisms of magnetization decay, a FF, generally, exhibits a wide and complex frequency response (see Fig. 3.7). More specifically, it can be distinguished a low frequency response (typically up to 100MHz), essentially related to Néel and Brownian relaxations, and an high frequency response (typically above 100MHz) essentially related to the ferromagnetic resonance.

Accordingly, $\chi(\omega)$ consists of two contributions: a *parallel susceptibility*, describing the part of frequency response due to relaxation mechanisms, and a *trasverse susceptibility* describing the part of frequency response due to ferromagnetic resonance [55, 60, 70].

Concerning the parallel susceptibility, $\chi_{\|}(\omega)$, it has the following expression [55, 70]:

$$\chi_{\|}(\omega) = \chi'_{\|}(\omega) - j\chi''_{\|}(\omega) = \chi_0 \frac{F_1(\sigma)}{F_0(\sigma)}\left(\frac{1}{1+j\omega\tau_{eff}}\right) = \chi_0 \frac{F_1(\sigma)}{F_0(\sigma)}\left(\frac{1-j\omega\tau_{eff}}{1+(\omega\tau_{eff})^2}\right) \quad (3.20)$$

where [60]:

$$F_n(\sigma) = \int_0^1 x^{2n} \mathrm{epx}(\sigma x^2)\mathrm{d}x \qquad n=0,\ 1,\ 2... \quad (3.21)$$

and where χ_0 and τ_{eff} are given in eqs. (3.10) e (3.16), respectively. As can be seen, $\chi_{\parallel}(\omega)$ displays a Debye-type profile, in agreement with the fact that $\chi_{\parallel}(\omega)$ describes relaxation mechanisms. In particular, $\chi'_{\parallel}(\omega)$ decreases monotonically with ω, whereas $\chi''_{\parallel}(\omega)$ has a maximum for $\omega = 1/\tau_{eff}$. Usually, when the dominant relaxation mechanisms is the Brownian one, the maximum of $\chi''_{\parallel}(\omega)$ occurs below 1MHz [29, 39-49], while when the dominant relaxation mechanisms is the Néel one, the maximum of $\chi''_{\parallel}(\omega)$ occurs above 1MHz [42, 51-57].

Concerning the trasverse susceptibility, $\chi_{\perp}(\omega)$, it is given by [55, 70]:

$$\chi_{\perp}(\omega) = \chi'_{\perp}(\omega) - j\chi''_{\perp}(\omega) = \chi_0\left(1 - \frac{F_1(\sigma)}{F_0(\sigma)}\right)\frac{1 + j\omega\tau_2 + \Delta}{1 + \Delta - \omega^2\tau_2\tau_{\perp} + j\omega(\tau_2 + \tau_{\perp})} = \chi_0\left(1 - \frac{F_1(\sigma)}{F_0(\sigma)}\right)\frac{(1+\Delta)^2 + \omega^2\tau_2(\tau_2 - \Delta\tau_{\perp}) - j\omega\tau_{\perp}\left((\omega\tau_2)^2 + (1+\Delta)\right)}{\left(1 + \Delta - \omega^2\tau_2\tau_{\perp}\right)^2 + \omega^2(\tau_{\perp} + \tau_2)^2} \tag{3.22}$$

where [60]:

$$\Delta = \sigma\tau_2\frac{(\sigma\tau_0 - \tau_{\perp})}{(\alpha\sigma\tau_0)^2} \tag{3.23}$$

$$\tau_1 = 2\sigma\tau_0\left(3 - \sigma + 2\sigma\frac{F_2(\sigma) - F_3(\sigma)}{F_1(\sigma) - F_2(\sigma)}\right) \tag{3.24}$$

$$\tau_{\perp} = 2\sigma\tau_0\left(\frac{F_0(\sigma) - F_1(\sigma)}{F_0(\sigma) + F_1(\sigma)}\right) \tag{3.25}$$

It can be proved that for $\omega \approx \omega_{res}$ $\chi'_{\perp}(\omega)$ becomes negative, whereas $\chi''_{\perp}(\omega)$ exhibits a maximum. In other words, $\chi_{\perp}(\omega)$ displays a resonant-like profile, which is in agreement with the fact that $\chi_{\perp}(\omega)$ takes in account the ferromagnetic resonance.

The complete expression of $\chi(\omega)$ is obtained by summing, eqs. (3.20) and (3.22) [55, 70], i.e.:

$$\chi(\omega) = \chi_{\parallel}(\omega) + \chi_{\perp}(\omega) = \chi'(\omega) - j\chi''(\omega) \tag{3.26}$$

It must be stressed that the expression (2.22) provides an accurate description of the frequency behaviour of a FF provided that σ is not in the

range 1-5, as discussed [70-71]. Moreover, for $1 < \sigma < 5$ the expression available for the Néel relaxation time, i.e. eq. (3.15), is not exact, but obtained by means of a fitting of the Brown's expression (3.12) (see Sec. 3.1.5.2). As a result, the model developed for the magnetic susceptibility of a FF could provide not reliable results for MNPs with $\sigma \in (1, 5)$.

From eq. (3.20), (3.22) and (3.26) it can be noted that: $\chi(0) = \chi_0$. Accordingly, the expression (3.26) for $\chi(\omega)$ is in agreement with the results obtained for the equilibrium magnetization. Moreover, for $\omega << \omega_{res}$ we have:

$$\chi_{\perp}(\omega) \cong \chi_0 \left(1 - \frac{F_1(\sigma)}{F_0(\sigma)}\right)\left(1 - j\frac{\omega\tau_{\perp}}{1+\Delta}\right) = \chi_{\infty}\left(1 - j\frac{\omega\tau_{\perp}}{1+\Delta}\right) \tag{3.27}$$

Thus, for $\omega << \omega_{res}$ it follows that:

$$\chi(\omega) = \chi_{\parallel}(\omega) + \chi_{\infty} = \frac{\chi_0 - \chi_{\infty}}{1 + j\omega\tau_{\text{eff}}} + \chi_{\infty}\left(1 - j\frac{\omega\tau_{\perp}}{1+\Delta}\right) \tag{3.28}$$

As can be seen from eq. (3.28), the total susceptibility exhibits a Debye-like profile. As a result, far from the resonance frequency, a FFs behaves like a polar liquids or a paramagnetic gas [35].

In conclusion, one wish to underline that eqs. (3.20), (3.22) and (3.26) hold for monodisperse FFs. They generalize to the case of polydisperse FFs, characterized by a joint size-anisotropy distribution function $g(r, K_a)$, by using the average formula:

$$\chi(\omega) = \iint \chi(\omega, r, K_a) g(r, K_a)\, \mathrm{d}r\mathrm{d}K_a \tag{3.29}$$

Eq. (3.29) results in a further frequency spreading of $\chi(\omega)$.

3.1.5.5 Magnetic power dissipation in a ferrofluid

An ac MF, when applied to a FF, dissipates energy as indicated by the non-zero imaginary part of the magnetic susceptibility $\chi(\omega)$.

From a physical point of view, the magnetic power dissipation in a FF is caused by the friction that the magnetic moments of suspended MNPs experience when rotating, subjected to the action of an applied ac MF. Due to the different nature of the relaxation mechanisms, the friction is either of mechanical or magnetic nature. Obviously, the friction is of mechanical nature when the involved dissipation mechanism is the Brownian relaxation,

while it is of magnetic nature when the involved losses mechanism is the Néel relaxation or the ferromagnetic resonance.

By using the Poyinting's theorem and noting that $\mu(\omega) = 1 + \chi(\omega)$, the expression of the magnetic power density absorbed by a FF immersed in an ac MF, operating at the angular frequency ω is given by:

$$p = \mu_0 \frac{\omega}{2} \chi''(\omega) |H|^2 \tag{3.30}$$

where $\chi''(\omega)$ is defined in (3.26) and H is the amplitude of the total MF acting inside the FF.

Ascribing the magnetic losses to the only suspended MNPs (this assumption is consistent with the non magnetic nature of the solvent and of the coating) the power density absorbed by the FM material dispersed into a FF is:

$$p_m = \frac{p}{c} = \mu_0 \frac{\omega}{2c} \chi''(\omega) |H|^2 \tag{3.31}$$

The magnetic power absorbed by a single suspended MNP it is obtained multiplying eq. (3.31) by the magnetic volume, V_m, of the MNP, i.e.:

$$P = p_m V_m = \mu_0 \frac{\omega}{2c} \chi''(\omega) V_m |H|^2 = \frac{p}{n} = \mu_0 \frac{\omega}{2n} \chi''(\omega) |H|^2 \tag{3.32}$$

Eq. (3.32) holds for monodisperse FFs. In the case of MNPs with different size and anisotropy constant, eq. (3.32) provide a mean magnetic power absorbed by a single dispersed MNP, if averaged over the distribution function $g(r, K_a)$.

As can be noted, eqs (3.30) to (3.32) relate the magnetic power absorbed by the suspended MNPs to parameters of the physical system, namely amplitude and frequency of the applied MF (i.e. H and ω), nature of the solvent (i.e. η), MNP-concentration (i.e. c or n), MNP-size (i.e. d_m and d_h), nature of the magnetic material composing the MNP (i.e. M_s and K_a) and temperature of the FF. Accordingly, they represent useful tools to design MNPs and exposition apparatuses, for biomedical applications of MNPs.

3.2 Experimental validation of the models proposed for the magnetic susceptibility of a ferrofluid

Broadband spectroscopy of the magnetic susceptibility, $\chi(\omega)$, of FFs represents an powerful and accurate way to characterize FFs. In fact, when measured over a frequency range from Hz to GHz, the experimental profile of $\chi(\omega)$ enables relaxation mechanisms, both Brownian and Néel, as well as ferromagnetic resonance to be identified and investigated. Moreover, from measurements of $\chi(\omega)$ one can investigate magnetic losses arising in the fluids.

For this reason in the open literature is available a satisfactory number of experimental data, over a wide frequency range, about the magnetic susceptibility $\chi(\omega)$ of commercial FFs.

In this section, we exploit some of these data to acquire, over a frequency range as large as possible, information about the actual magnetic power absorbed by a MNP in suspension. The aim is to establish whether the level of energy transferred from the applied ac MF to MNP is consistent with the biomedical applications of MNPs.

In addition, the obtained experimental values of the power are compared with those achieved theoretically by using the model for $\chi(\omega)$ previously discussed. The aim is to establish the degree of accuracy of the proposed model in estimating the magnetic power absorbed by MNPs in suspension.

3.2.1 Experimental values of the magnetic power absorbed by magnetite nanoparticles in suspension

The experimental data elaborated to estimate the actual magnetic power absorbed by MNPs in suspension are referred to magnetite (Fe_3O_4) NPs of 10nm in size, dispersed in hydrocarbons. They are reported in [54, 56].

We have considered Fe_3O_4-NPs because magnetite is biocompatible, hence exploitable in biomedical applications. Indeed, the biomedical applications of MNPs require also the biocompatibility of the carrier liquid. Accordingly, to obtain reliable data one should be deal with acqueous FFs. Unfortunately, in the open literature, apart from the data reported in [58], is not available an accurate characterization, over a wide frequency range, of water-based FFs. However, the choice to analyze Fe_3O_4-NPs of 10 nm in size (magnetic size) should provide reliable results, although the data examined are referred to suspensions in non biocompatible liquids. In fact, according to the

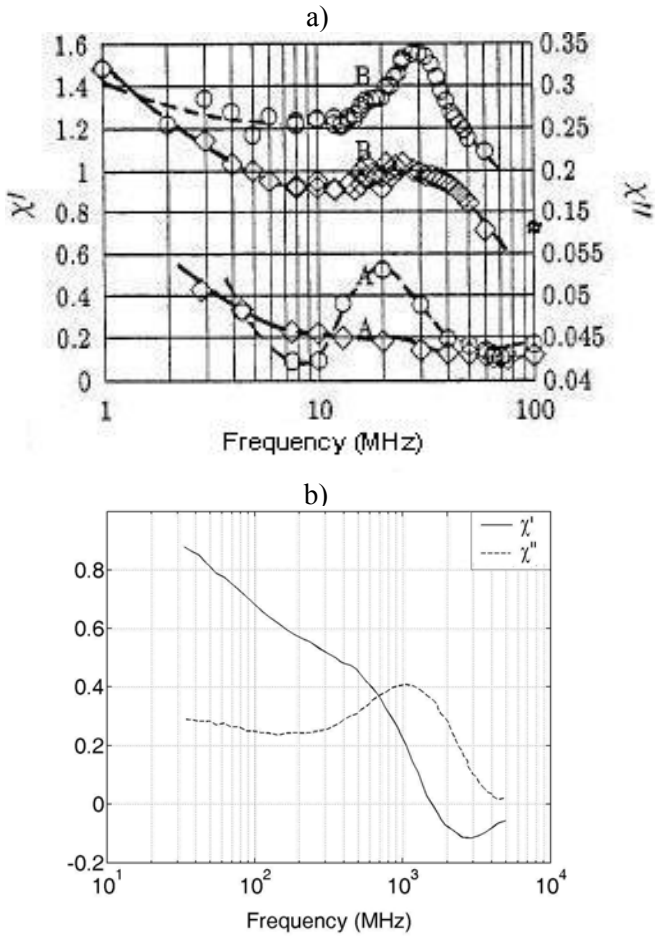

Fig. 3.8. a) frequency profiles of the real (◊) and the opposite of imaginary (o) parts of the magnetic susceptibility of FF-samples, A and B, investigated in [54]; b) frequency profiles of the real (solid line) and the opposite of imaginary (dashed line) parts of the magnetic susceptibility of FF-sample investigated in [56]

sample	FF	M_{oo}(kA/m)	M_s(kA/m)	d_m (nm)	c (%)
A [54]	Fe_3O_4 in kerosene	11.32	477.5	11.1	2.4
B [54]	Fe_3O_4 in kerosene	39.56	477.5	9.3	8.3
C [56]	Fe_3O_4 in paraffin	31.83	318.3	10	10

Tab. 3.1- values of the physical parameters of FF-samples investigated in [54] and in [56]

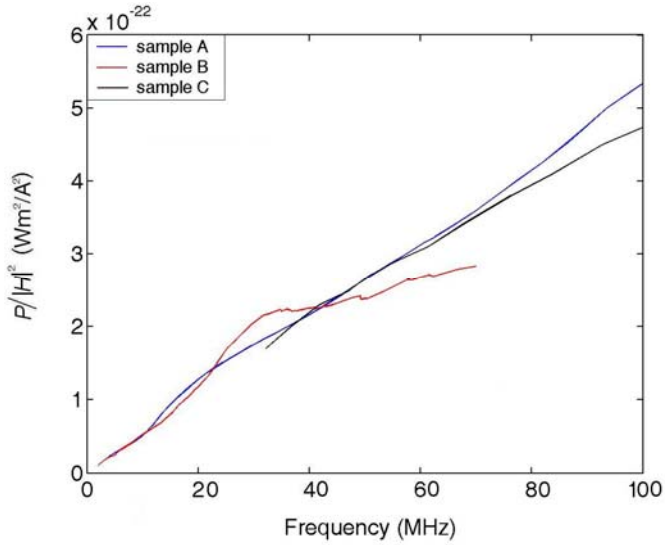

Fig. 3.9. Frequency profiles of the mean magnetic power absorbed by each Fe_3O_4-NP, dispersed in samples A (blue line), B (red line) and C (black line), investigated in [54] and [56], normalized to the square of magnetic field strength, $|H|^2$.

theoretical models previously introduced, Fe_3O_4-NPs of 10nm in size should be superparamagnetics, hence the losses mechanisms should be the Néel relaxation, which is independent of the nature of solvent.

In Tab. 3.1 are reported the values of the main physical parameters of the two FF-samples, A and B, investigated in [54] and of the FF-sample, say C, investigated in [56].

In Fig. 3.8a are shown the experimental profiles versus frequency of the complex magnetic susceptibility of FF-samples A and B, while in Fig. 3.8.b is displayed the susceptibility profile of the FF-sample C.

As can be seen from Fig. 3.8a-b, for all samples the imaginary parts of $\chi(\omega)$ exhibits an absorption peak at $f \approx 20$ - 30 MHz resulting in a effective relaxation time shorter than 7×10^{-9} sec. Since 10nm-Fe_3O_4-NPs, dispersed in oils, have a Brownian relaxation time much longer than 7×10^{-9} sec ($\tau_B \approx 7\times10^{-7}$, by assuming $\eta = 10^{-3}$ Pa sec and $\delta = 2$nm [54, 56]), one can conclude that the dominant relaxation mechanism for the analyzed Fe_3O_4-NPs is the Néel one. This result is in agreement with theoretical models which predict a superparamagnetic behaviour for Fe_3O_4-NPs of 10nm in size in suspension.

From Fig. 3.8b one can also note that at $f \approx 1.7$ GHz χ' change sign (χ' passes from positive to negative values), while at $f \approx 1$ GHz χ'' exhibits a maximum. Accordingly, the high frequency profile of the complex susceptibility of the FF-sample C is related to the phenomenon of ferromagnetic resonance.

One wish to point out that for Fe_3O_4-NPs, by assuming M_s = 318.3 kA/m and K_a = 11 kJ/m^3 (see Tab. 3.2), $\omega_{res}/2\pi \approx 1.9$ GHz that is in good agreement with the value at which χ' change sign. On the contrary $\omega_{res}/2\pi$ disagrees with the value at which χ'' has the maximum. This discrepancy is caused by the smallest Fe_3O_4-NPs in suspension, whose relaxation-absorption peaks, occurring at $f \sim 1$ GHz, determine a spreading of the resonance-absorption peak resulting in down-shift of the frequency at which χ'' has a maximum.

In Fig 4.9 are plotted the corresponding profiles, in the frequency range 1 – 100 MHz, of the mean magnetic power absorbed by each Fe_3O_4-NP, dispersed in samples A, B and C, normalized to the square of MF strength, $|H|^2$. In particular, the blue line is referred to the samples A, the red line is referred to the samples B and the black line is referred to the samples C. These profiles are obtained by exploiting eq. (3.32) and the values of d_m and c listen in Tab. 3.1.

As can be seen from Fig. 3.9, for all samples, above 20 MHz, the mean magnetic power absorbed by a single suspended NP is larger than 10^{-22} Jm^2/A^{2}sec. Therefore, it is sufficient a MF-amplitude of few tens of A/m to dissipate, in one second, an amount of energy of about 10^{-19} J, i.e. the energy required to dehybrydize the DNA molecule used in [5]. Accordingly, the data acquired over the frequency range 1 – 100 MHz show that the magnetic power absorbed by each suspended Fe_3O_4-NP should be sufficient for the biomedical applications of Fe_3O_4-NPs, in particular to remotely control biological nanomachines by means of radiofrequency MFs.

From Fig. 3.9 one can note also a satisfactory overlapping among the profiles of each sample, over the entire frequency range 1 – 100 MHz. Since FF-samples A, B and C substantially differ only for the carrier liquids (kerosene for samples A and B and isoparaffin for sample C) one can conclude that as long as the losses mechanism is the Néel relaxation, as happens for samples A, B and C, the power absorbed by each NP is independent of the nature of the carrier liquids. This result make the data illustrated in Fig. 3.9 reliable even if they are referred to a non water-based FFs.

As a matter of fact, experimental data on aqueous suspensions of Fe_3O_4-NPs, of 10nm in size, there exist and are reported in [58]. These data are directly provided in terms of the magnetic power absorbed by the FF-sample because they has been obtained by means of SLP measurements [58]. In particular, SLP measurements are performed by placing the FF-sample into

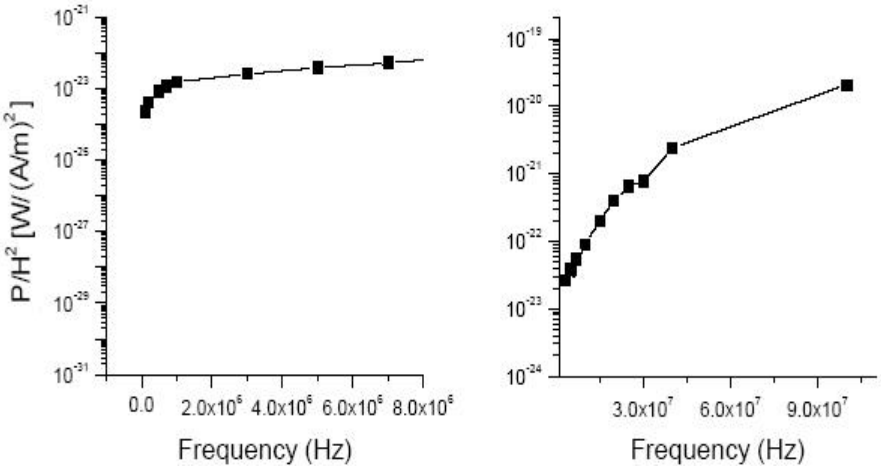

Fig. 3.10. Frequency profile of the mean magnetic power absorbed by each Fe_3O_4-NP, dispersed in the ferrofluid sample investigated in [58], normalized to the square of magnetic field strength, $|H|^2$.

a radiofrequency electromagnetic field produced by a in a coil of 25 turns [58].

The frequency-profile of the power absorbed by each suspended Fe_3O_4-NP, as reported as in [58], is shown in Fig. 3.10. As can be noted the value of power is about two order of magnitude larger than those achieved from the data reported in [54, 56]. The origin of such discrepancy could be the different nature of the carrier liquid (water), which in this case, unlike the ones used in [54, 56], is strongly polar. However, such hypothesis disagrees with theoretical models, previously discussed, which predict a superparamagnetic behaviour for 10nm-Fe_3O_4-NPs and consequently losses mechanisms that are independent of the nature of the solvent. A more realistic hypothesis could be the presence in the FF-sample of unexpected electric losses, which, due to the type of measurement, cannot be distinguished by the magnetic losses and so are erroneously ascribed to MF.
Nevertheless, the above incongruence make necessary a broadband spectroscopy of the magnetic susceptibility of water-based FFs, which will be presented in Chapter 5.

The mean magnetic power absorbed by a single 10nm Fe_3O_4-NPs in hydrocarbons, normalized to the square of MF strength $|H|^2$, has been estimated also over the frequency range wherein the dominant energy transfer mechanism is the ferromagnetic resonance. The results are reported in Fig. 3.11.
As it can be noted from Fig. 3.11, the mean magnetic power absorbed by each suspended Fe_3O_4-NPs is larger than 5×10^{-22} Jm^2/A^2sec over the whole

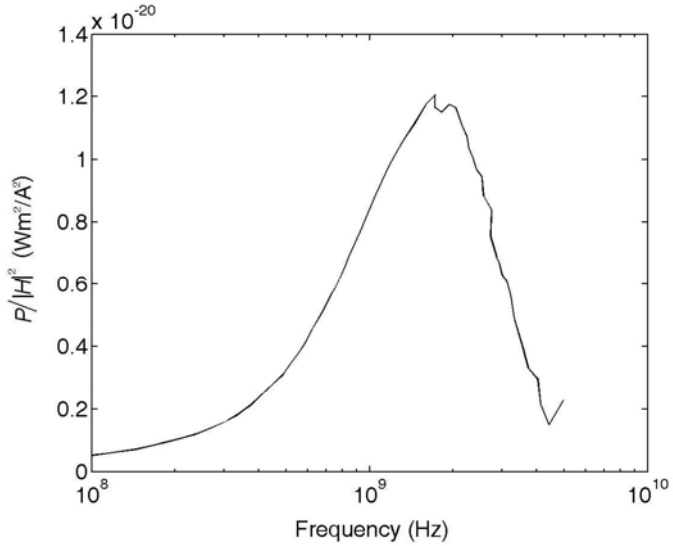

Fig. 3.11. Profile, over the frequency range 0.1 – 5 GHz, of the mean magnetic power absorbed by each Fe_3O_4-NP, dispersed in the ferrofluid sample investigated in [56], normalized to the square of magnetic field strength, $|H|^2$.

frequency range, furthermore, at $f \approx 2$ GHz, it displays a maximum of about 10^{-20} Jm^2/A^2sec. Thus, at $f \approx 2$ GHz it would be sufficient a MF-amplitude of almost 3 – 4 A/m to dissipate, in one second, the energy required to open the DNA molecule used in [5].

By comparing the profile in Fig. 3.11 with the profiles in Fig. 3.10 one can also note that the power dissipation related to the phenomenon of ferromagnetic resonance is much higher than the one related to the relaxation mechanisms. This result shows that the ferromagnetic resonance is an energy transfer mechanism more efficient than relaxation mechanisms. Therefore, for the biomedical applications of Fe_3O_4-NPs, it would seem convenient to operate at $f \approx 2$ GHz, i.e. to exploit the ferromagnetic resonance, even if the energy transfer associated to the relaxation mechanisms is high enough for these purposes. However, it is worth noting that the frequency f to be used to efficiently exploit the ferromagnetic resonance ($f \approx 2$ GHz) is too large to be biologically tolerable and to allow a sufficient penetration of the biological tissues. Therefore for the biomedical applications of Fe_3O_4-NPs it results more convenient to exploit the relaxation mechanisms.

solvent	d_m (nm)	c (%)	M_s(kA/m)	K_a(kJ/m^3)	ref.
kerosene	9.3	8.3	477.5	13.3	[29]
kerosene	11	2.4	477.5	12	[54]
kerosene	9	8.3	477.5	14.4	[54]
kerosene	10.8	?	477.5	13	[57]
isopar *M*	10	10	318.3	8.4 (12.3)	[63]
isopar *M*	9.4	10	318.3	9.4 (14.1)	[64]
isopar *M*	10	10	318.3	9.6 (14.4)	[67]
kerosene	9	5.3	477.5	13.7	[69]
kerosene	9	3.7	477.5	12.7	[69]

Tab. 3.2 Experimental values of the saturation magnetization, *Ms*, and anisotropy constant, *Ka*, for magnetite nanoparticles of about 10 nm in size.

3.2.2 Experimental values of M_s e K_a for magnetite nanoparticles

In order to estimate the power absorbed by a Fe_3O_4-NP in suspension through the theoretical expression for $\chi(\omega)$, it is needed to know the values of M_s and K_a for Fe_3O_4-NPs.

For bulk magnetite the quoted values for M_s and K_a are about 480 kA/m and 11 kJ/m^3 [27], respectively. However, these values could be unsuitable for Fe_3O_4-NPs because of the size-effects arising at nanometer scale. Therefore, it has been led an accurate research in literature about the experimental values of M_s, K_a for Fe_3O_4-NPs. The results are listen in Tab. 3.2.As can be seen from Tab. 3.2, in some cases the value adopted for M_s is smaller than the one quote for bulk magnetite. This assumption is justified by the spin disorder arising at the surface of MNP, which becomes important at nanometer scale. However, there are cases where the value used for M_s is assumed equal to the value quoted for the bulk magnetite. This assumption in [72] is explained by the presence of the coating, whose effect is to reduce the spin disorder at surface of the MNP.

Concerning the values of K_a, from the data reported in Tab. 3.2 one can note a discrepancy between the value quoted for bulk magnetite and those determined experimentally. This incongruence is caused by both the contributions of shape and surface anisotropy [26-29] and by dipole-dipole interactions. The latter contribution yields an increase of the value of K_a in that increases the local field acting on each NP and hence the effective anisotropy field acting on **m** [29, 53-54, 57, 66, 69].

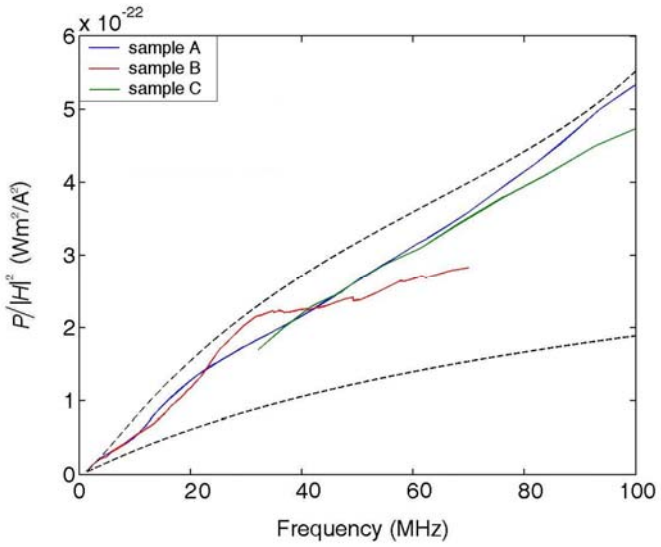

Fig. 3.12. Comparison between the experimental profiles of the mean magnetic power absorbed by each Fe_3O_4-NP, dispersed in the ferrofluid sample investigated in [54 ,56] (solid lines), and the theoretical data (region bounded by the dashed curves).

This explanation is in agreement with the experimental results reported in Tab. 3.2, where the measured values of K_a increase with the MNP-concentration.

As a matter of fact, the experimental values of K_a related to FFs with the highest MNP-concentration are the smallest reported in Tab. 3.2. This apparent inconsistency with the other values listen in Tab. 3.2 is explained by the different value of M_s used to evaluate K_a from the experimental data, i.e. M_s=318,3 kA/m, instead of M_s=480 kA/m. If it is assumed M_s=480 kA/m the corresponding values of K_a are those reported within brackets, which are consistent with the other ones.

In the following, the theoretical values of the power absorbed by a Fe_3O_4-NP in suspension will be estimated by assuming. M_s = 318.3-480 kA/m and K_a = 8-15 kJ/m^3, in agreement with the values reported in Tab. 3.2.

3.2.3 Comparison between experimental and theoretical values of the power absorbed by magnetite nanoparticles in suspension

In order to verify the reliability of the proposed models in estimating the magnetic power absorbed by Fe_3O_4-NPs in suspension, the experimental

values of the power shown in Fig. 3.9 are compared with those calculated by using the expression for $\chi(\omega)$ given in Sec. 3.1.5.4 and the values for M_s and K_a given in Sec. 3.2.2.

The analysis has been restricted to the data up to 100 MHz, in that, as pointed out is Sec. 3.2.1, higher frequencies are not exploitable in biomedical applications.

In Fig. 3.12 it is shown the comparison between the experimental profiles of the power, represented by the solid lines, and theoretical data, represented by the region bounded by the dashed curves. We have a band for theoretical values of the power in that it has been assumed M_s = 318.3 - 480 kA/m, K_a = 8 - 15 kJ/m^3 (see Tab. 3.2) and for d_m a lognormal distribution with a mean magnetic diameter of 10 nm and a standard deviation of 0.4 [54, 56].

From Fig. 3.12 one can note that the band of theoretical values of the power is sufficiently narrow over the whole frequency range analyzed, furthermore, the experimental profiles are entirely contained within it. Therefore, one can conclude that the theoretical expression for $\chi(\omega)$ given in Sec. 3.1.5.4 enables to obtain reliable estimations, at least of the order of magnitude, of the mean magnetic power absorbed by a Fe_3O_4-NP in suspension. Accordingly, it can be successfully exploited in designing Fe_3O_4-NPs and exposition apparatuses for specific biomedical applications.

As a concluding remark, it is worth noting that a more accurate theoretical estimation of the power absorbed by Fe_3O_4-NPs in suspension it is possible by providing a more careful estimation of M_s and K_a for the suspended Fe_3O_4-NPs. However, this task cannot be accomplished on the base of theoretical considerations because of the strong spreading characterizing the values of such parameters. In fact, the values of M_s and K_a depend, besides on the FM material composing the MNP, also on the size and shape of the MNP, nature of the coating, MNP-concentration in the FF, MNP-aggregation. Moreover, they could depend also on the nature of the solvent containing the Fe_3O_4-NPs. Accordingly, the only way to accurately evaluate M_s and K_a is to perform a wideband spectroscopy of the magnetic susceptibility of water-based FF. This experimental investigation will be given in Chapter 5.

3.3 Conclusions

In this Chapter the main mechanisms of interaction between MF and FFs together with the theoretical models developed to describe the dependence of the magnetic susceptibility, $\chi(\omega)$, on the physical features of dispersed MNPs have been presented.

Moreover, by exploiting some interesting experimental data, available in open literature, about the magnetic susceptibility of suspension of 10 nm magnetite-NPs, it has been estimated the actual magnetic power absorbed by magnetite-NPs in suspension, over a broad frequency range. The analysis has allowed to assess the real applicability of MNPs in biomedical applications and the degree of accuracy of the proposed model in estimating the power absorbed by MNPs in suspension.

The obtained results have shown that 10nm-magnetite-NPs are able to absorb an amount of energy large enough to activate the functions of the most of biological macromolecules. Therefore, magnetite-NPs are promising candidate to remotely control BNM. However, the cited data could be not reliable, since they are referred to MNP-suspensions in non biocompatible liquids, although magnetite NPs of 10nm in size are superparamagnetics and hence the losses mechanism should be independent of the nature of the solvent. Suitable data can be surely obtained through a wideband spectroscopy of $\chi(\omega)$ of magnetite NPs in water, never investigated till now in the open literature.

Also, the comparison between the experimental values of power and those calculated by using the theoretical expression for $\chi(\omega)$ and the experimental values of M_s and K_a has shown that the proposed models could provide reliable estimations of the power absorbed by MNP in liquids on the condition that the values of M_s and K_a are accurately known. Accordingly, they could represent useful tools to design MNPs and exposition apparatuses for biomedical applications. However, the values M_s and K_a cannot be derived on the base of theoretical considerations, due to the strong variability of such parameters with the size and shape of the MNP, nature of the coating, MNP-concentration in the FF, MNP-aggregation. Thus, the only way to accurately evaluate M_s and K_a is to perform a wideband spectroscopy of the magnetic susceptibility of water-based FF.

Chapter 4

Short/Open Coaxial Line multicells measurement technique

Wideband spectroscopy of the magnetic susceptibility, $\chi(\omega)$, of FFs represents an accurate and efficient tool to investigate the dynamic properties of these colloidal suspensions. In fact, when measured over a frequency spectrum from Hz to GHz, the experimental profile of $\chi(\omega)$ allows the investigation of both relaxation mechanisms and ferromagnetic resonance of FFs as well as the determination of some properties of suspended MNPs, such as the mean anisotropy constant, K_a, and the saturation magnetization, M_s. Moreover, from measurements of $\chi(\omega)$ one can also investigate magnetic losses arising in the fluids, as shown in Chapter 3. Accordingly, to fully characterize the magnetic properties of FFs, and hence of suspended MNPs, it is crucial to be able to measure $\chi(\omega)$ over a large frequency range, typically from Hz to GHz.

In the open literature the experimental profiles of the magnetic susceptibility of oil-based FFs (apolar FFs), in the range 1 MHz – 20 GHz, are successfully measured by using coaxial-cable measurements techniques [54, 73]. In particular, the most used techniques are: the T*ransmission/Reflection* (T/R) and the S*hort-Circuited-Coaxial-Line* (SCCL) methods [62, 74] in that they provide the best trade-off between bandwidth and accuracy. Moreover, they allow to manage small volumes of FF.

However, unlike apolar FFs, the open literature lacks for the experimental characterizations, over the band 1 MHz - 20 GHz, of Water-based FFs (WFF), although they are of interest, especially for the biomedical applications of MNPs, as stressed in Chapter 3. Likely, the reason is the difficulty to perform, with the existing measurement techniques, an accurate and broadband detection of the magnetic properties of substances with strong dielectric response and weak magnetic response, as it is expected for WFFs.

In this Chapter a measurement strategy improving the performance of T/R and SCCL techniques in estimating the magnetic susceptibility of liquids, like WFFs, together with the measurement apparatus purposely designed and realized to implement the approach, are presented.

Moreover, to show the reliability of the implemented strategy and apparatus in measuring the electromagnetic parameters of liquids, measurements on electromagnetically-known materials such as ethanol and water are presented.

4.1 Requirement for the measurement of the magnetic permeability of water-based ferrofluids

As briefly accounted in the introductory part, an accurate experimental investigation of the magnetic properties of WFFs, over a large frequency range, is a not easy task in that at the same time it is required:

1) a broadband spectroscopy, typically from Hz to GHz;
2) the capability to operate on small volumes of WFFs;
3) a high sensibility in determining $\chi(\omega)$.

Condition 1) is required to estimate, over a frequency spectrum as larger as possible, the absorbing power capabilities of MNPs in a solvent compatible with biological applications and to identify the frequency bandwidths wherein the energy exchange between the RF MF and MNPs is most efficient. Moreover, a broadband spectroscopy enables also to estimate the values of parameters, such as M_s and K_a, involved in the theoretical model for $\chi(\omega)$. Condition 2) is required because of the high complexity and cost for producing these colloidal suspensions. Finally, condition 3) is related to the need of detecting small values of the magnetic susceptibility in substances, as the WFFs, where the dielectric response is strong.

Measurement techniques able to meet requirement 1) are coaxial-cable measurement techniques such as T/R and SCCL methods, already fruitfully exploited in the literature to measure, over the frequency range 1MHz – 20 GHz, the magnetic susceptibility of apolar FFs [54, 73]. Moreover, they allow also to manage small volumes of WFFs and so to satisfy requirement 2).

However, the performance of T/R and SCCL techniques in determining $\chi(\omega)$ drastically decay when the substance under test (sample) is characterized by large values of the relative electric permittivity, ε_r, and small values of the relative magnetic permeability, μ_r ($\mu_r = 1 + \chi$), as it is expected for WFFs. In particular, as it will be shown in the following, the T/R method exhibit a significant accuracy reduction, whereas the SCCL

technique a significant bandwidth limitation. This aspect makes these techniques unsuitable to measure the permeability of WFFs in that they are not able to simultaneously satisfy requirements 1) and 3). Therefore, the measurement of the μ_r of WFF has required the implementation of a properly measurement strategy able to overcome the above limitation and consequently to meet requirements 1) and 3). This strategy is presented in Sec. 4.3.

4.2 Overview of the methods used in literature to measure the magnetic permeability of Ferrofluids

In this section one analyzes the performance of the main measurement techniques exploited in the open literature to measure the magnetic permeability of FFs: T/R and SCCL techniques. The aim is to establish the limits of these technique in measuring the magnetic permeability of samples like WFFs.

4.2.1 Transmission/Reflection measurement method

The T/R measurement technique determines the ε_r and μ_r of the sample by measuring the scattering parameters S_{11} and S_{21} at input ports of a section of coaxial cable (measurement cell) filled with the sample (see Fig. 4.1a) [74].
The basic equations of the T/R method are [74]:

$$S_{11} = \frac{\left(1-T^2\right)\Gamma}{1-T^2\Gamma^2} \tag{4.1a}$$

$$S_{21} = \frac{\left(1-\Gamma^2\right)T}{1-T^2\Gamma^2} \tag{4.1b}$$

where Γ is the reflection coefficient at the interface vacuum-sample (see Fig. 4.1a), i.e:

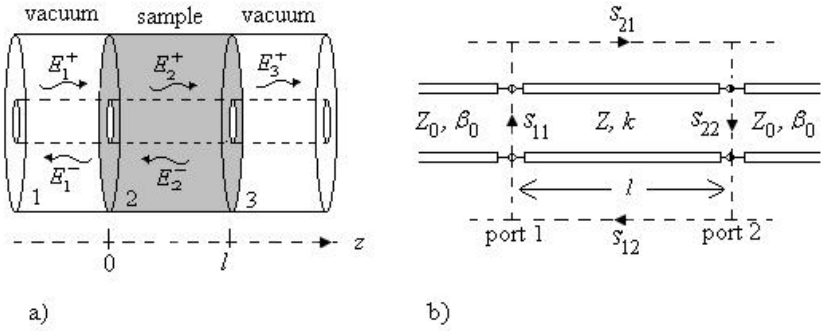

Fig. 4.1. a) Transmission/Reflection configuration; b) equivalent transmission line of the Transmission/Reflection configuration

$$\Gamma = \frac{\sqrt{\mu_r} - \sqrt{\varepsilon_r}}{\sqrt{\mu_r} + \sqrt{\varepsilon_r}} \tag{4.2}$$

and T is the propagation factor through the sample, namely:

$$T = \exp(-jkl) = \exp\left(-j\sqrt{\mu_r \varepsilon_r}\,\beta_0 l\right) \tag{4.3}$$

In eq. (4.3) k is the propagation constant in the sample, l is the sample-length and β_0 is propagation constant in vacuum.

Accordingly, to extract ε_r and μ_r from measurement data sets S_{11} and S_{21}, firstly, one has to evaluate Γ and T from eqs. (4.1). Once Γ and T have been determined, one can calculate $(\mu_r/\varepsilon_r)^{1/2}$ and $(\mu_r\varepsilon_r)^{1/2}$ by using eqs (4.2) and (4.3), i.e.:

$$\sqrt{\frac{\mu_r}{\varepsilon_r}} = \frac{1+\Gamma}{1-\Gamma} \tag{4.4}$$

$$\sqrt{\mu_r \varepsilon_r} = \frac{j}{\beta_0 l}\log T \tag{4.5}$$

Finally ε_r and μ_r are attained by multiplying and dividing eq. (4.4) by eq. (4.5).

It is worth noting that eq. (4.5) has an infinite number of root in that the imaginary part of $\log T$ is equal to the phase of the complex number T plus $2n\pi$, where n is a integer number. From a physical standpoint, eq. (4.5) is

ambiguous because the phase of the propagation factor T does not change when the sample length is increased by a multiple of wavelength in the sample, λ. However, the ambiguity in determining $(\mu_r\varepsilon_r)^{1/2}$ can be solved by measuring the group delay through the sample, which is strictly a function of the sample length.

Also, due to the measurement errors, a critical behaviour is exhibited by the T/R method at the frequencies corresponding to $n\lambda/2 = l$ specially when low-loss sample are considered. In fact at these frequency $T = \pm 1$, $S_{11} = 0$, $S_{21} = \pm 1$ (see eqs. (4.3) and (4.1)) and consequently any value for Γ satisfy eqs (4.1). Thus, a small error on measurement data sets S_{11} and S_{21} induces large error in determining Γ.

As a concluding remark, one wishes underline two important aspects of the T/R technique. First, the equations to be used to calculate ε_r and μ_r from measurement data S_{11} and S_{21}, i.e. eqs (4.1), (4.4) and (4.5), are exact and valid at any frequency. As a result, no limit on the analyzable frequency spectrum characterizes the T/R method within the exploitable bandwidth of a coaxial cable. Second, the separation between ε_r and μ_r does not take place at the measurement stage because ε_r and μ_r are inextricably mixed within the measurement data. Therefore, it is expected that the accuracy of T/R method in estimating μ_r (ε_r) decreases with increasing the dielectric (magnetic) response of the sample. The latter characteristic makes this technique unable to satisfy requirement 3) discussed in Sec. 4.1.

4.2.2 Short Circuited Coaxial Line measurement technique

Unlike T/R method, the SCCL technique operates on a single data set and allows to measure only the magnetic properties of the sample.

More specifically, the SCCL technique determines the $\mu_r = \mu_r' - j\mu_r''$ of the sample by measuring the reflection coefficient Γ_s at the input port of a section of a coaxial cable (measurement cell) filled with the sample and ended on a short load (see Fig. 4.2a) [62].

The equation to be considered to extract μ_r from the measurement data set Γ_s is (see Fig. 4.2b) [62]:

$$\Gamma_s = \frac{Z_{in} - Z_0}{Z_{in} + Z_0} = \frac{j\sqrt{\frac{\mu_r}{\varepsilon_r}}\tan(kl) - 1}{j\sqrt{\frac{\mu_r}{\varepsilon_r}}\tan(kl) + 1} = \frac{j\sqrt{\frac{\mu_r}{\varepsilon_r}}\tan\left(\sqrt{\mu_r\varepsilon_r}\beta_0 l\right) - 1}{j\sqrt{\frac{\mu_r}{\varepsilon_r}}\tan\left(\sqrt{\mu_r\varepsilon_r}\beta_0 l\right) + 1} \tag{4.6}$$

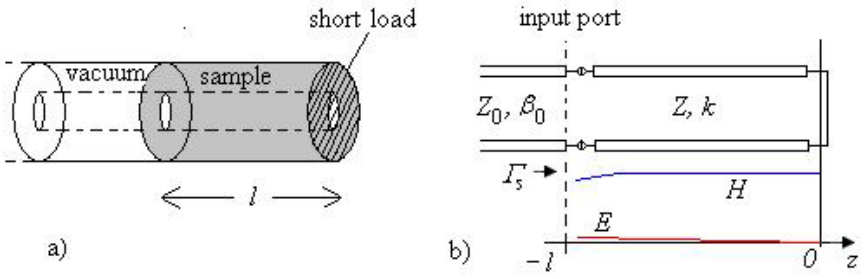

Fig. 4.2. a) Short Circuited Coaxial Line configuration; b) equivalent transmission line of the Short Circuited Coaxial Line configuration ($k|l << 1$)

where Z_{in} is the impedance measured at the input port of the measurement cell, Z_0 is the characteristic impedance of the empty cell, k is the propagation constant in the sample, and l the sample-length.

As can be seen from eq. (4.6), to obtain μ_r from Γ_s it is needed to know ε_r of the sample which, generally, is unknown as μ_r. However, if it is assumed: $|k|l << 1$ (electrically short sample) one can expand the tangent function in eq. (4.6) in Taylor series and retain only the lowest order term in kl. Accordingly, as long as $|k|l << 1$, eq. (4.6) becomes:

$$\Gamma_s \cong \frac{j\mu_r\beta_0 l - 1}{j\mu_r\beta_0 l + 1} \tag{4.7}$$

As can be noted, in this case Γ_s depends only on μ_r, thus, one can determine μ_r from Γ_s. This is the idea underlying the SCCL measurement technique [62].

From eq. (4.7) one obtains the following expressions for the real and the opposite of imaginary part of μ_r:

$$\mu_r' = \frac{2}{\beta_0 l}\left(\frac{|\Gamma_s|\sin\theta_s}{1+|\Gamma_s|^2-2|\Gamma_s|\cos\theta_s}\right) \tag{4.8a}$$

$$\mu_r'' = \frac{1}{\beta_0 l}\left(\frac{1-|\Gamma_s|^2}{1+|\Gamma_s|^2-2|\Gamma_s|\cos\theta_s}\right) \tag{4.8b}$$

where $|\Gamma_s|$ and θ_s are the magnitude and the phase of the complex data set Γ_s. Eqs (4.8a-b) represent the formulae to be used to calculate μ_r from measurement data Γ_s (the inversion procedure).

From a physical point of view, the measurement data set Γ_s, is independent of ε_r in that the presence of the short circuit and the condition $|k|l << 1$ make the EF negligible, as compared with the MF, over the entire sample-length (see the blue and red lines in Fig. 4.2b).

This feature makes the SCCL technique particularly sensitive in estimating μ_r, specially when samples with strong dielectric properties and weak magnetic properties are considered, as in the case of WFFs. For this reason the SCCL technique has been extensively exploited to measure the magnetic permeability of apolar FFs [54, 62, 65 56]. However, the condition: $|k|l << 1$ precludes a broadband spectroscopy of μ_r of the sample specifically when $|k|$ is much larger than β_0, as it happens for WFFs. Obviously, by reducing l the analysable spectral range increases, but the accuracy of the technique decreases due to the errors in estimating l (trade off between bandwidth and accuracy).

Accordingly, one can conclude that the SCCL technique display an high accuracy in determining the magnetic permeability of sample, but a significant bandwidth limitation, in particular when the sample has a strongly dielectric response. The latter characteristic makes this technique unsuitable to meet requirement 1) discussed in Sec. 4.1.

4.2.3 Open Ended Coaxial Line measurement technique

As previously pointed out, unlike T/R method, the SCCL technique does not allow to measure the electric permittivity of the sample. However, if one is interested to detect also the dielectric properties of the sample, it is sufficient to replace in the SCCL configuration the short load with an open load and measure the reflection coefficient, say Γ_o, at the input port of the measurement cell (see Fig. 4.3a). In fact, in this case the measurement data set, Γ_o, depends only on the ε_r, as shown by expression of the reflection coefficient in terms of admittance, Y_{in}, measured at the input port of the measurement cell (see Fig. 4.3b):

$$\Gamma_o = \frac{1 - Z_0 Y_{in}}{1 + Z_0 Y_{in}} = \frac{1 - j\sqrt{\frac{\varepsilon_r}{\mu_r}}\tan(kl)}{1 + j\sqrt{\frac{\varepsilon_r}{\mu_r}}\tan(kl)} = \frac{1 - j\sqrt{\frac{\varepsilon_r}{\mu_r}}\tan\left(\sqrt{\mu_r\varepsilon_r}\beta_0 l\right)}{1 + j\sqrt{\frac{\varepsilon_r}{\mu_r}}\tan\left(\sqrt{\mu_r\varepsilon_r}\beta_0 l\right)} \cong \frac{1 - j\varepsilon_r\beta_0 l}{1 + j\varepsilon_r\beta_0 l} \qquad (4.9)$$

(Obviously, it is assumed $|k|l << 1$).

Accordingly, by changing the short load in an open load and measuring Γ_o one can detect also the dielectric permittivity of the sample without changing approach and hence measurement setup.

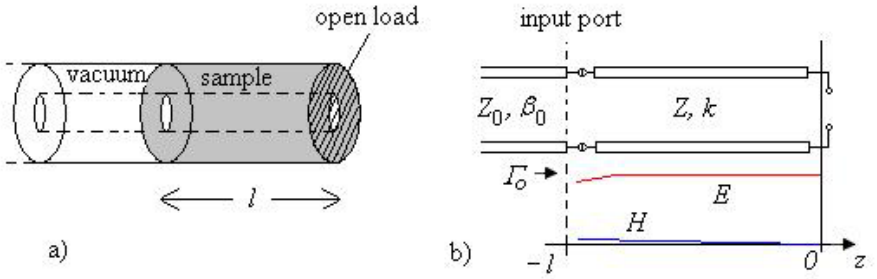

Fig. 4.3. a) Open Ended Coaxial Line configuration; b) Equivalent transmission line of the Open Ended Coaxial Line configuration ($k|l << 1$)

The basic equations to be used to determine the real and the opposite of imaginary part of ε_r from the measurement data set Γ_o are:

$$\varepsilon_r' = -\frac{2}{\beta_0 l}\left(\frac{|\Gamma_o|\sin\theta_o}{1+|\Gamma_o|^2+2|\Gamma_o|\cos\theta_o}\right) \tag{4.10a}$$

$$\varepsilon_r'' = \frac{1}{\beta_0 l}\left(\frac{1-|\Gamma_o|^2}{1+|\Gamma_o|^2+2|\Gamma_o|\cos\theta_o}\right) \tag{4.10b}$$

where $|\Gamma_o|$ and θ_o are the magnitude and the phase of the complex data Γ_o. Eqs. (4.10a-b) have been obtained from eq. (4.9).

The procedure just described represents the *Open Ended Coaxial Line* (OECL) measurement technique and it can be considered the dual of the of the SCCL technique. As a result, the OECL technique is characterized by a high sensibility in estimating ε_r and a significant bandwidth limitation, specially when samples with high permittivity are considered.

In conclusion, like T/R method, the use of SCCL and OECL techniques allows to determine both ε_r and μ_r, but with an accuracy and a bandwidth limitation higher than the T/R method.

4.2.4 Improvement of Short Circuited and Open Ended Coaxial Line measurement techniques

A source of error in estimating ε_r and μ_r by means of SCCL and OECL techniques is a non ideal behaviour of the terminal loads (open and short).

A way to remove this source of error is to characterize the actual behaviour of the loads, over the frequency range of interest, and properly

modify the inversion procedure in order to take in account for the non ideality of the loads. However, there exists a more convenient way to remove the error due to the non ideality of the loads, based on the following considerations.

The input impedance, Z_{in}, of the measurement cell filled with the sample and ended on a non ideal short load, of impedance Z_s, is given by:

$$Z_{in} = Z\frac{Z_s + jZ\tan(kl)}{Z + jZ_s\tan(kl)} \tag{4.11}$$

where Z is the characteristic impedance of the coaxial cell filled with the sample.

Similarly, the input impedance, Z^0_{in}, of the empty cell terminated on a non ideal short load, of impedance Z_s, is given by:

$$Z^0_{in} = Z_0\frac{Z_s + jZ_0\tan(\beta_0 l)}{Z_0 + jZ_s\tan(\beta_0 l)} \tag{4.12}$$

Now, if $|Z_s|$ is sufficient small to assume $|Z_s\tan(\beta_0 l)| << |Z_0|$ and $|Z_s\tan(kl)| << |Z|$, Z_{in} and Z^0_{in} can be simplified as follows:

$$Z_{in} \cong Z_s + jZ\tan(kl) \tag{4.13}$$

$$Z^0_{in} \cong Z_s + jZ_0\tan(\beta_0 l) \tag{4.14}$$

Thus, by subtracting eq. (4.14) to the eq. (4.13) and dividing by Z_0 one obtains:

$$\frac{Z_{in} - Z^0_{in}}{Z_0} = \frac{1+\Gamma_s}{1-\Gamma_s} - \frac{1+\Gamma^0_s}{1-\Gamma^0_s} \cong j\frac{Z}{Z_0}\tan(kl) - j\tan(\beta_0 l) \cong j\beta_0 l(\mu_r - 1) \tag{4.15}$$

where Γ^0_s is the reflection coefficient measured at the input port of the empty cell ended on a non ideal short circuited, of impedance Z_s.

As can be seen from eq. (4.15), the measurement data are proportional to μ_r and independent of Z_s. As a result, the determination of μ_r from the measurement data does not require the knowledge of the impedance of the used short load. The only conditions to be satisfied are $|Z_s\tan(\beta_0 l)| << |Z_0|$ and $|Z_s\tan(kl)| << |Z|$, which are quite verified if a well-designed short load ($|Z_s| \approx 0$), in the frequency range of interest, is used.

In similar way, for the OECL configuration it can be proved that:

$$Z_0\left(Y_{in}-Y_{in}^0\right)=\frac{1-\Gamma_o}{1+\Gamma_o}-\frac{1-\Gamma_o^0}{1+\Gamma_o^0}\cong j\frac{Z_0}{Z}\tan\left(kl\right)-j\tan\left(\beta_0 l\right)\cong j\beta_0 l\left(\varepsilon_r-1\right) \qquad (4.16)$$

if a well-designed open load, in the frequency range of interest, is exploited. In eq. (4.16) Y_{in} is the input admittances of the measurement cell filled with the sample and ended on a non ideal open load, while Y^0_{in} are Γ^0_o are the input admittances and the reflection coefficient of the empty cell terminated on a non ideal open load, respectively.

Accordingly, the error on the measurement data caused by the non ideal behaviour of the short and open loads can be removed by subtracting the measurement data sets obtained by measuring the reflection coefficient at the input port of both the empty cell and the cell filled with the sample.

As concluding remark, one note that the procedure just described enables to remove not only the error due to the non ideal behaviour of the terminal load, but any systematic error affecting the measurement data, as the error due to connector mismatching, the error related to the finite conductivity of the walls of the measurement cell, the errors introduced by measurement instrumentations and so forth.

4.2.5 Uncertainty analysis of Transmission/Reflection and Short Circuited Coaxial Line techniques

To investigate the performance of the T/R and SCCL techniques in measuring the magnetic permeability of samples like WFFs, an uncertainty analysis has been carried out.
The main sources of error, here considered, are:

- errors in measuring the real and imaginary parts of the scattering parameters, ($\Delta S'_{11}$, $\Delta S''_{11}$) and ($\Delta S'_{21}$, $\Delta S''_{21}$);
- error in estimating the sample-length, Δl;

for the T/R method, and:

- errors in measuring the real and imaginary parts of the reflection coefficient, ($\Delta\Gamma'_s$, $\Delta\Gamma''_s$);
- error in estimating the sample-length, Δl;

For the SCCL technique.

The analysis has been carried out by exploiting as nominal values for ε_r and μ_r the profiles in blue in Fig. 4.5a-b (they represent the profiles of ε_r

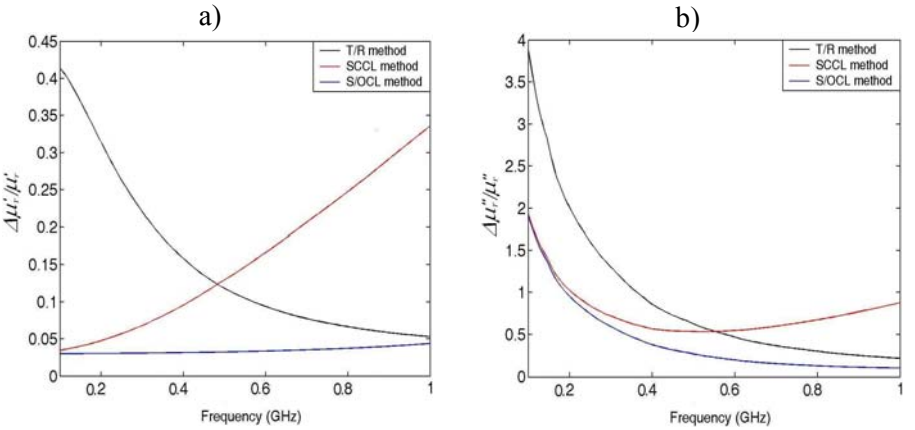

Fig. 4.4. Comparison between the frequency profiles of the relative uncertainty of the Transmission/Reflection (black lines) and Short Circuited Coaxial Line (red lines) measurement strategies in detecting μ'_r, μ''_r, for nominal values of ε_r and μ_r close to those expected for a WFF: a) relative uncertainty in estimating μ'_r; b) uncertainty in estimating μ''_r.

and μ_r expected for a WFFs) and assuming l = 5 mm, $\Delta l/l$ = 0.01 and a relative error in measuring the real and imaginary parts of S_{11}, S_{21} and Γ_s of 1%.

The expressions of the relative errors in $\Delta\mu'_r/\mu'_r$ and $\Delta\mu''_r/\mu''_r$ for both T/R and SCCL techniques are give in Appendix D.

The results are plotted in Fig. 4.4a-b. In particular, in Fig. 4.4a it is shown the comparison between the frequency-profiles of $\Delta\mu'_r/\mu'_r$, for the T/R method (black line) and SCCL technique (red line); in Fig. 4.4b it is shown the comparison between the frequency-profiles of $\Delta\mu''_r/\mu''_r$. The analyzed frequency spectrum is 0.1 – 1GHz..

From Fig. 4.4a-b, one can easily note that either T/R or SCCL methods are unable to guarantee an high level of accuracy over the entire frequency range of interest, and consequently to meet requirement 1) and 3) discussed in Sec. 4.1. In fact, for the T/R method the accuracy decreases with decreasing f, making the technique inaccurate at low frequencies. On the contrary for the SCCL technique the accuracy decreases with increasing f, making the technique inaccurate at high frequencies. Accordingly, neither T/R nor SCCL methods can be successfully exploited to measure the μ_r of WFFs on the entire frequency range of interest.

However, it is worth noting that for the SCCL technique the error on the measurement result is due not only to the errors on the measurement data, i.e. on Γ_s and l, but also to the error in approximating eq. (4.6) with eq. (4.7). The latter source of error increases with f, furthermore, it is the dominant contribution to the uncertainty on μ_r when $|k|l$ becomes comparable or larger than one. As a result, by reducing such source of error one could

significantly enhance the accuracy of the SCCL technique at high frequencies of the spectrum of interest and consequently to improve the bandwidth limitation characterizing the SCCL method. Fortunately, the error in approximating eq. (4.6) with eq. (4.7) can be eliminated by properly combining the measurement data of the SCCL technique with those of the OECL techniques, as it will be shown in the next section.

4.3 The Short/Open Coaxial Line multicells measurement technique

The limits of the SCCL measurement technique are essentially related to the use of a single data set and of approximated relations to calculate the frequency profile of μ_r from measurement data.

Such limits can be mitigated by using the *Short/Open circuited Coaxial* Line (S/OCL) measurement strategy, in the following described.

The S/OCL strategy determines the electromagnetic parameters ε_r and μ_r of the sample by processing together two data sets, obtained by measuring the reflection coefficients Γ_s and Γ_o at the input port of a coaxial cell filled with the sample and ended in turn on a short circuit (SCCL configuration in Fig. 4.2a) and on an open circuit (OECL configuration in Fig. 4.3a), respectively.

The basic equations to be used to determine ε_r and μ_r from the measurement data sets Γ_s and Γ_o are:

$$\frac{1+\Gamma_s}{1-\Gamma_s} = j\sqrt{\frac{\mu_r}{\varepsilon_r}}\tan\left(\sqrt{\mu_r\varepsilon_r}\,\beta_0 l\right) \tag{4.17}$$

$$\frac{1+\Gamma_o}{1-\Gamma_0} = j\sqrt{\frac{\mu_r}{\varepsilon_r}}\cot\left(\sqrt{\mu_r\varepsilon_r}\,\beta_0 l\right) \tag{4.18}$$

The approach determines both ε_r and μ_r from a SCCL and OECL configuration, but the simultaneous use of equations (4.17) and (4.18) allows to overcome the restriction $|k|l << 1$, characterizing the SCCL and OECL techniques. As a result, no limit on the analyzable frequency range exists and the measurement sensitivity is increased. Accordingly, the proposed technique can be considered an extension of SCCL and OECL techniques

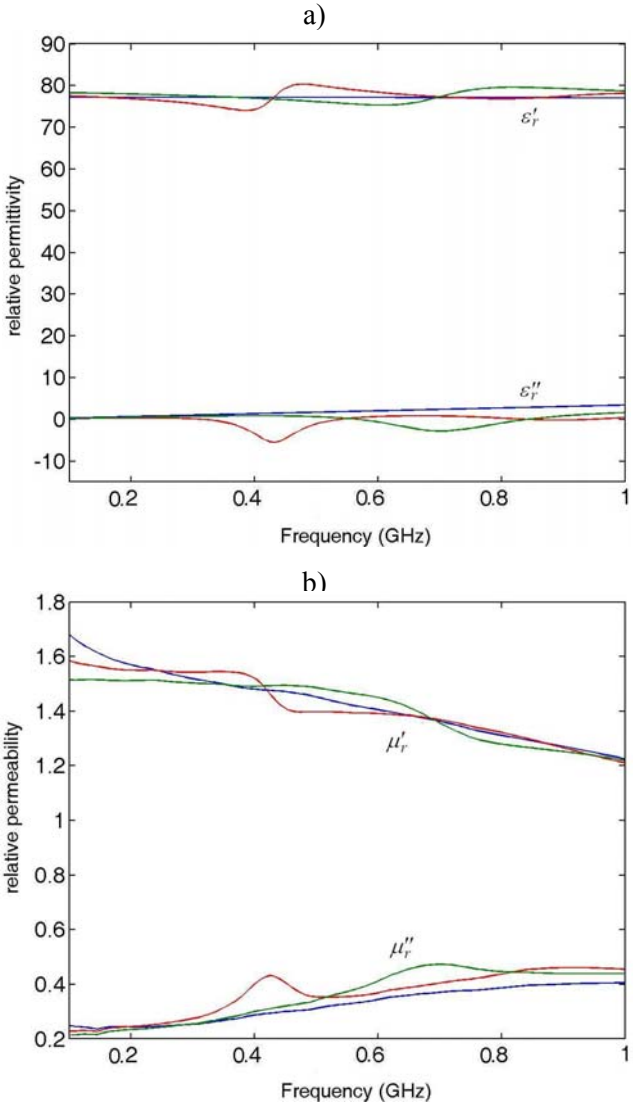

Fig. 4.5- Comparison among the expected profiles of ε_r and μ_r (blue lines) with the ones obtained from eqs. (4.17) and (4.18) when the input data are affected by errors. Red lines: l=16mm; and green line: l=10mm

that increases the performance in terms of accuracy and frequency bandwidth.

However, due to the measurement errors, the S/OCL technique exhibits a critical behaviour at frequencies corresponding to $n\lambda \approx 4l$, especially when low-loss sample are involved (n natural number) as shown by the numerical

example reported in Fig. 4.5. Here, the red lines represent the values for ε_r and μ_r which can be obtained from eqs (4.17) and (4.18) when the measured data are effected by errors on l, say Δl, on the magnitude and phase of Γ_s and Γ_o, say ($\Delta|\Gamma_s|$, $\Delta\theta_s$) and ($\Delta|\Gamma_o|$, $\Delta\theta_o$) respectively. The blue lines represent the profiles expected for ε_r and μ_r. As can be seen, a good agreement is achieved as long as the frequency f is far from 400 MHz, with a small discrepancy essentially related to the error on l. Instead, the discrepancy increases around $f \approx 400$ MHz corresponding to $\lambda \approx 4l$. As previously quoted, peaks of error occurs also at frequencies such that $\lambda \approx 4l/n$, with $n \geq 1$, however, these frequency fall out the frequency spectrum here investigated, namely (0.1-1GHz).

The described $n\lambda/4$-effect is related to the singular behaviour of either the tangent or cotangent functions, in eqs. (4.17) and (4.18), when their arguments approach $n\pi/2$, ie. when $\lambda \approx 4l/n$.

The above analysis has assumed $l = 16$mm, $\Delta l = 0.2$mm, $\Delta|\Gamma_s|_{\text{db}} = 0.02$ db $\Delta|\Gamma_o|_{\text{db}} = 0.02$dB, $\Delta\theta_s = 0.5°$, $\Delta\theta_o = 0.5°$. Furthermore, a large value of $|\varepsilon_r|$ compared with the value of $|\mu_r|$ has been chosen, in order to investigate the behaviour of the technique when samples like WFFs are involved.

Since the frequencies at which the described effect takes place are strongly sample-length dependent, it can be circumvented by using cells with different values of l in order to centre the resonant-like $n\lambda/4$-effects around different frequencies, suitably far from each other, as shown by the numerical example depicted in Fig. 4.5.

Here the resonant effect centred on $f \approx 400$ MHz (red lines) is compared to the one centred on $f \approx 700$ MHz (green lines). As can be seen, by comparing the red and green curves it can be established whether the observed resonant-like profiles exhibited is a property of the investigated sample or is related to $n\lambda/4$-effect (In the first case the resonant-like behaviour has to take place at the same frequency and with the same intensity in both profiles). Moreover, by combining the red and green lines it is possible to obtain a good accuracy in estimating μ_r over the entire analyzed frequency range.

This is the idea underlying the proposed measurement method, here referred to as S/OCL multi-cell, namely a S/OCL technique operating on two or more different values of l, properly chosen, in order to allow a broadband spectroscopy, with a good accuracy in estimating the μ_r, especially of substances with strong dielectric properties and weak magnetic properties.

4.4 Uncertainty analysis of the Short/Open Coaxial Line multicells measurement technique

By exploiting the values ε_r and μ_r in Fig. 4.5 (blue lines), an uncertainty analysis has been carried out to analyze the accuracy of the S/OCL multicells measurement strategy, in particular in estimating μ_r, for nominal values of ε_r and μ_r close to those expected for a WFF.
The main sources of error, here considered, are:

1. Errors in measuring the real and imaginary parts of the reflection coefficients: ($\Delta\Gamma_s'$, $\Delta\Gamma_s''$) and ($\Delta\Gamma_o'$, $\Delta\Gamma_o''$);
2. Error in estimating l: Δl;
3. A non ideal behaviour of the terminal loads (open and short).

As a matter of fact, the source of error 3 can be removed by characterizing the behaviour of the loads over the frequency range of interest and properly modifying the inversion procedure in order to take in account for the non ideality of the loads. Therefore, the analysis can be simplified by considering only the sources of errors 1 and 2.

The expressions of the relative errors in estimating the real and imaginary part of ε_r and μ_r are given in Appendix D.

The results of the uncertainty analysis are shown in Fig. 4.6a-d. Here each curve corresponds to a different value of l, namely l=6, 10, 14, 22, 30mm. The analysis has been carried out by assuming Δl = 0.2mm, $\Delta|\Gamma_s|_{\text{db}}$ = 0.02 db $\Delta|\Gamma_o|_{\text{db}}$ = 0.02dB, $\Delta\theta_s$ = 0.5°, $\Delta\theta_o$ = 0.5° corresponding to a maximum relative error on the real and imaginary parts of the reflection coefficients of about 1%.

As can be seen from Fig 4.6c-d, for each curve the relative errors in estimating the real and imaginary part of μ_r is sufficient small as far as f is different from $f_{n\lambda/4} \approx nv/4l$, with v the speed of light in the sample. On the contrary, the error significantly increases when f approaches $f_{n\lambda/4}$. However, as stressed in the Sec. 4.3, since $f_{n\lambda/4}$ depend on l, a properly choice of the number and the values of l allows to allocate the peaks of error around frequencies far from each other and attain a good level of accuracy over the entire frequency spectrum of interest.

As can be noted from Fig 4.6c-d, the chosen set of l allows an uncertainty lower than 3% in estimating μ'_r and lower than 10% in estimating μ''_r, over the whole analyzed frequency range, i.e. 0.1 – 1GHz..

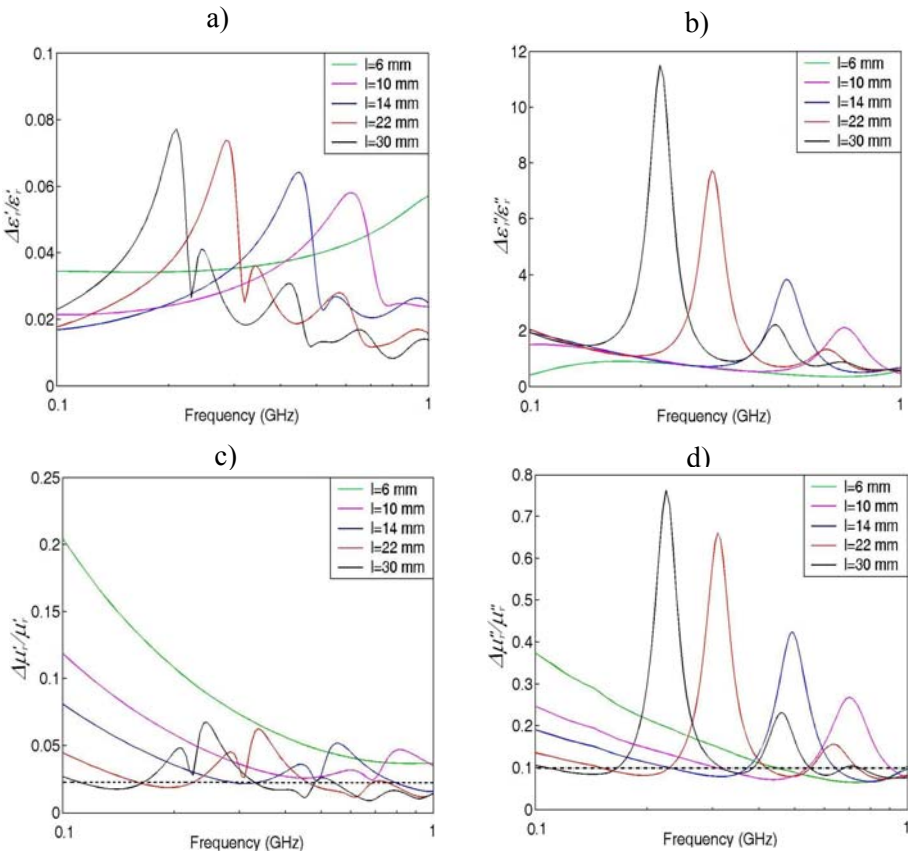

Fig. 4.6. Relative uncertainty of the S/OCL measurement strategy in detecting ε'_r, ε''_r, μ'_r, μ''_r for nominal values of ε_r and μ_r close to those expected for a WFF: a) relative uncertainty in estimating ε'_r; b) uncertainty in estimating ε''_r; c) uncertainty in estimating μ'_r; d) uncertainty in estimating μ''_r.

The results demonstrate a good sensitivity of the presented technique, on a large frequency range, in determining of μ_r of a sample with strong dielectric behaviour and slow magnetic losses that make it indicated to measure μ_r of WFFs.

4.5 Measurement apparatus

In order to implement the S/OCL multicells strategy, a specific measurement apparatus, made of coaxial cells and the terminal loads, has been designed and realized. In particular, the measurement equipment has

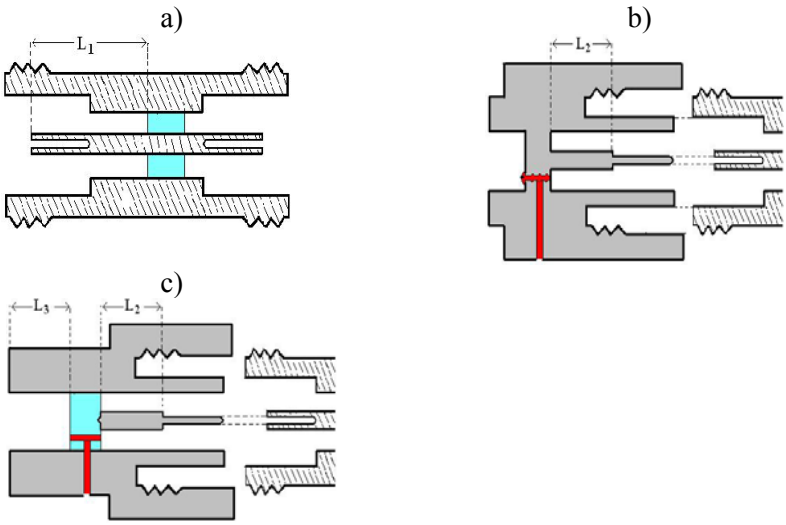

Fig. 4.7. A schematization of the measurement apparatus: a) coaxial cell; b) Short load; c)open load.

been realized paying attention to the following features, obviously entailed by the discussed strategy:

a) terminal loads with a behaviour very close to a short circuit and an open circuit, in the frequency range of interest;

b) same sample-length in both SCCL and OECL configurations;

c) cell of variable length.

Condition a) has been attained by realizing the short load by means of a metallic wall (Fig. 4.7b) and the open load by means of a section of circular waveguide of properly diameter and length (grey region in Fig. 4.7c). In particular, the diameter has been chosen in order that the smallest cut-off frequency of the circular waveguide is much larger than the maximum frequency of the analyzed spectrum. Moreover, the length of the waveguide has been chosen about 4 times larger than its diameter in order to allows the complete extinction of the excited evanescent modes. This solution, in fact, allow to obtain a device with a behaviour very close to an open circuits, over the entire frequency range of interest, as it is shown by numerical simulations(*) reported in Fig. 4.8.

Here the circles line represent the profiles, over the frequency spectrum 0.1 - 1GHz, of the magnitude of the reflection coefficient, computed at the

(*) The numerical simulations has been carried out by using a numerical simulator based on a Finite Element Method (FEM).

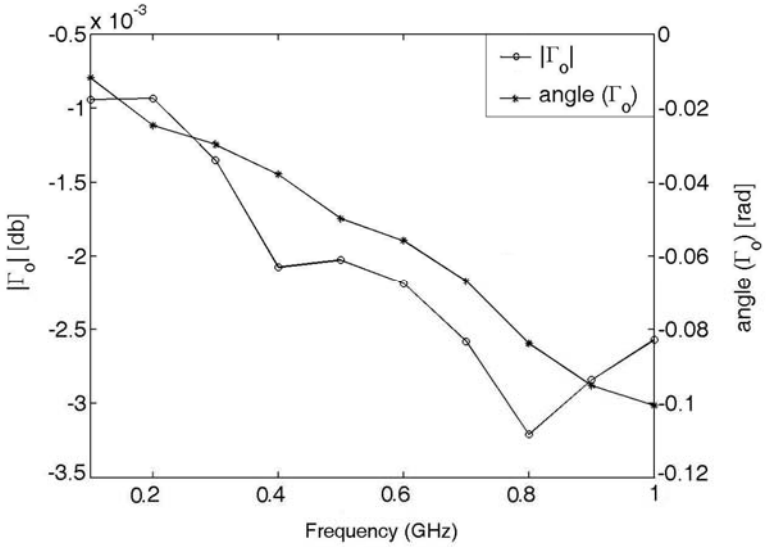

Fig. 4.8. Numerical characterization of the device used as open load over the frequency 0.1. – 1GHz range. The circles line represents the frequency-profile of the magnitude of reflection coefficient computed at the input of the device. The stars line represent profile of the phase of the reflection coefficient..

input section of the open load, while the stars represent line represent the profile of the phase of the reflection coefficient.

As it can be noted, they are very close to those of a open circuit, over the entire analyzed frequency range. The small discrepancy in the magnitude is essentially related to the losses on the walls of the waveguide, which increase with the frequency, whereas the small discrepancy in the phase is due to the electromagnetic energy stored in the waveguide, which increases with increasing frequency.

The simulations has been carried out by assuming for the circular waveguide a diameter of 7 mm, corresponding to a cut-off frequency of the dominant mode of about 25 GHz [75]., and a length of 3cm.

Requirement b) has been achieved by introducing inside the open load a teflon separator (cyan region in Fig. 4.7c) whose function is to close the cell in the OECL configuration as well as the metal wall of the short load closes the cell in the SCCL configuration. Moreover, to allow the introduction of the sample in the cell in both SCCL and OECL configurations, holes have been properly realized in the loads (red regions in Fig. 4.7b-c).

Finally, the feature c) is obtained by realizing more cells with different lengths (L_1 =6, 8, 22 mm in Fig. 4.7a) and more loads with different offset lengths (L_2 = 0, 2, 6, 8 mm in Fig. 4.7b-c).

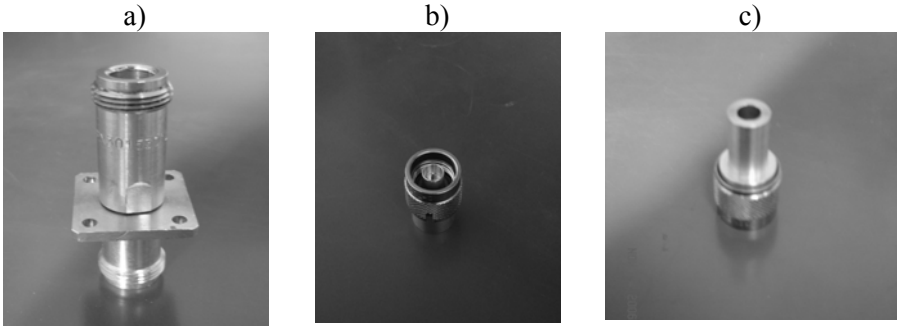

Fig. 4.9. A picture of some components of the measurement apparatus: a) coaxial cell; b) short load; c) open load

In Fig. 4.9 it is shown a picture of some components of the measurement apparatus. In particular, the N-Female N-Female connector (Fig. 4.9a) represents the measurement cell. The N-male terminations of Fig. 4.9b and Fig. 4.9c represent the short load and the open load, respectively. The measurement cell and load has been realized by using N-type connectors in that the dimension of N-type connectors (3 mm for the diameters of the inner conductor and 7mm for the diameter of the outer conductor) are large enough to allow the use of appreciable quantities of sample and small enough to meet requirement 2) discussed in Sec. 4.1.

4.6 Experimental validation of the Short/Open Coaxial Line multicells technique and apparatus

In order to verify the reliability of S/OCL strategy and the measurement apparatus in determining the electromagnetic parameters of liquids, in the frequency range 0.1 – 1 GHz, measurements on electromagnetically-known substances such as ethanol and bi-distilled water has been carried out. The results are plotted in Fig. 4.10a-b, Fig. 4.11a-b and Fig. 4.12.

Fig. 4.10a shows the comparison between Debye and experimental profiles (blue and red lines, respectively) of the relative permittivity of a sample of ethanol. The experimental profile has been obtained by using the S/OCL strategy and a measurement cell with a length l = 6mm. As can be noted, there is a satisfactory agreement between the two profiles, with a small discrepancy on ε''_r, at high frequencies of the analyzed spectrum, essentially related to the error on the sample-length and to the $\lambda/4$-effect,

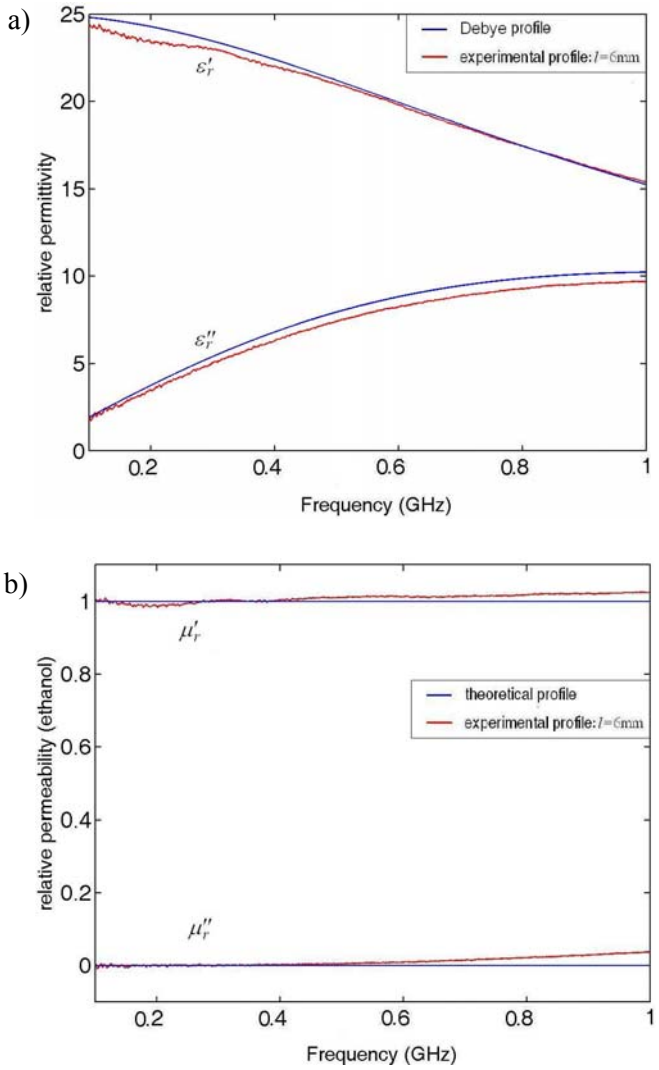

Fig. 4.10. Comparison between Debye and experimental profiles (blue and red lines, respectively) of the electromagnetic parameters of a sample of ethanol: a) the complex relative permittivity, ε_r; b) complex relative permeability, μ_r;

which for the chosen value of l occurs at a frequency higher 1 GHz.

In Fig. 4.10b the experimental profile (red lines) of the relative permeability of the investigated ethanol-sample is compared with the one expected for ethanol (blue lines). As can be seen, also for μ_r there is a satisfactory agreement between two profiles with a small discrepancy mainly due to the error on l and the $\lambda/4$-effect.

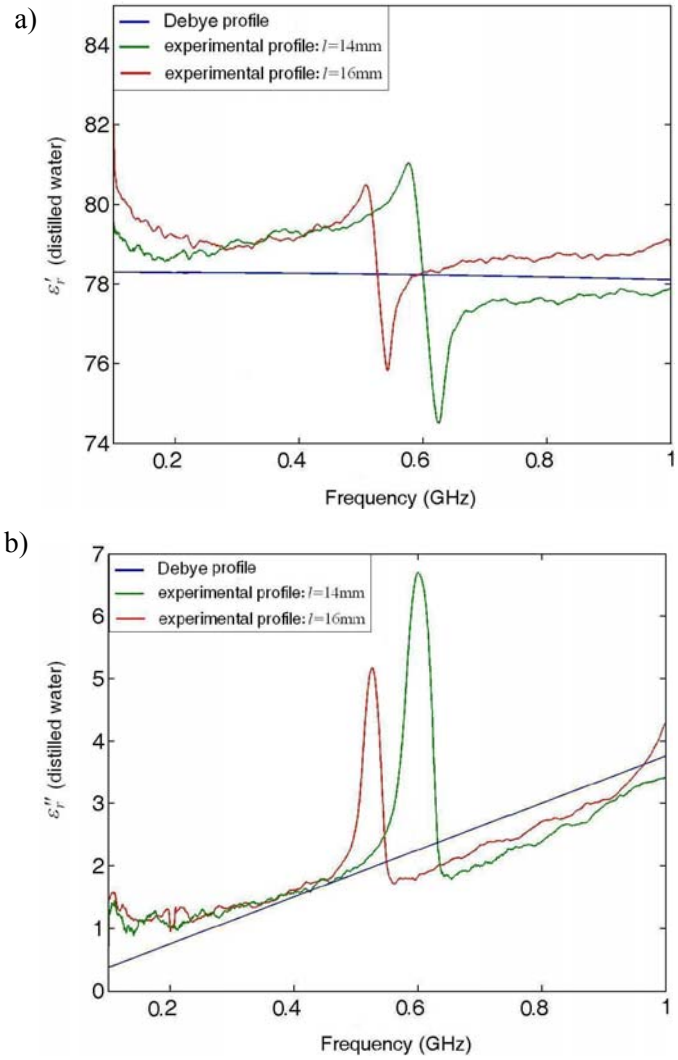

Fig. 4.11. Comparison between the Debye-profile (blue lines) and experimental profiles (red and green lines) of ε'_r (figure a) and ε''_r (figure b) of a sample of distilled water. In particular, the green curves has been achieved by using a sample length of 14mm, while the red curve has been obtained by using a sample length of 16mm.

To show the effects of the described $\lambda/4$-phenomenon, measurements on a sample of distilled water, by using measurement cells with l = 14, 16 mm, have been performed, as well. The results are shown in Fig. 4.11a-b and Fig. 4.12. In Fig. 4.11a-b it is displayed the comparison between the Debye profiles (blue lines) and the experimental profiles (green and red lines) of ε'_r (Fig. 4.11a) and ε''_r (Fig. 4.11b) of the investigated water-sample.

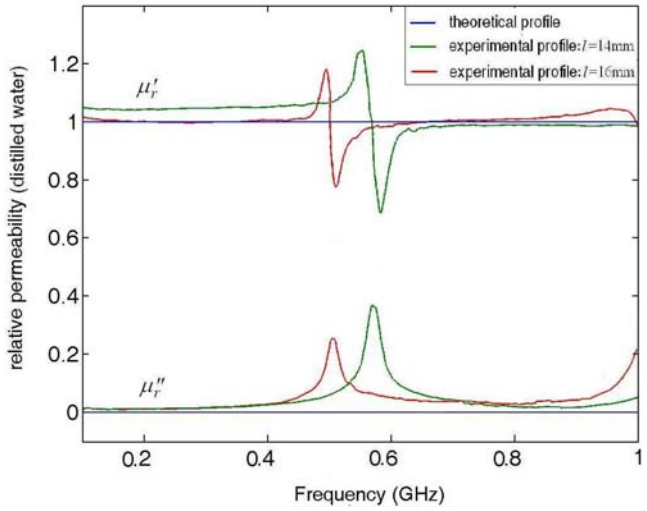

Fig. 4.12. Comparison between the theoretical profiles (blue lines) and experimental profiles (green and red lines) of the relative permeability of a sample of distilled water.

As can be seen, a good agreement between the theoretical and experimental profiles is achieved as long as the frequency f is far from 550 MHz, for l = 16 mm, and 600 MHz, for l = 14 mm, with a small discrepancy essentially related to the error on l. Instead, the discrepancy increases around $f \approx 550$ MHz corresponding to $\lambda \approx 4l$. However, by combining the two profiles it is possible to attain a good accuracy on the entire analyzed spectrum.

Fig. 4.12 shows the comparison between theoretical (blue lines) and experimental (green and red lines) profiles of the relative permeability of the investigated sample of water. As can be noted, for the experimental profile of μ_r one can draw the same conclusions drawn for the experimental profile of ε_r. The only difference is a more pronounced amplitude of the $n\lambda/4$-effect, due to the small values of μ_r compared with those of ε_r.

From the measurement results one can conclude that the presented S/OCL multicells strategy and the measurement apparatus allow the detection of the electromagnetic parameters of strongly polar liquids with an high accuracy, comparable with the one of the best measurement techniques available in literature.

4.7 Conclusions

In this chapter a new measurement strategy improving the performance of SCCL and OECL measurement techniques, in estimating the electromagnetic parameters of liquids, has been proposed.

In particular, as shown by the analysis of the uncertainties here reported, a better trade-off between the accuracy and the bandwidth limitations of the SCCL measurement technique is achieved in detecting the magnetic permeability of substances with a strong dielectric response and a weak magnetic response. Accordingly, the proposed strategy is particularly indicated to perform an accurate and broadband spectroscopy of the magnetic properties of WFFs, never investigated till now in the open literature and essential to establish the applicability of magnetic nanoparticles in the bio-medical application.

Also the measurement apparatus specifically designed and realized to implement the technique is presented and discussed.

Finally, the reliability of the proposed measurement strategy and apparatus, in detecting the electromagnetic parameters of liquids, have been tested on electromagnetically-known substances: ethanol and bi-distilled water. The measurement results have confirmed the result of the uncertainty analysis and have shown that the proposed strategy is able to detect the electromagnetic parameters of strongly polar liquids with an high accuracy, comparable with the one of the best measurement techniques available in literature.

Chapter 5

Wideband spectroscopy of a water-based ferrofluid and final considerations on the remote control of biological nanomachines

In this Chapter are presented and discussed the measurement results on the broadband spectroscopy of the complex permittivity and permeability of a commercial WFF, performed by exploiting the S/OCL multi-cells measurement strategy and the measurement apparatus described in Chapter 4.

Finally, by exploiting the results obtained until now and others available in literature, it is critically analyzed the possibility of using nanoparticle and radiofrequency electromagnetic fields to remotely control biological nanomachines, by exploiting the mechanism of interaction proposed in [5].

5.1 Main features of the investigated water-based ferrofluid

The investigated WFF is a colloidal suspension of Fe_3O_4-NPs of 10 nm in size (mean magnetic size) dispersed in water and stabilized with anionic surfactant (the product is delivered by Liquids Research Ltd, Limited kingdom). The main physical characteristics of the suspension are listen in Tab. 5.1.

In Fig. 5.1 it is shown a Transmission Electronic Microscopy picture of the investigated WFF.

We have investigated a suspension of Fe_3O_4-NPs with a mean magnetic diameter of 10 nm because they are the only commercially available aqueous solution with a NP-concentration high enough to make the magnetic susceptibility, $\chi(\omega)$, of the dispersion appreciably different from zero and

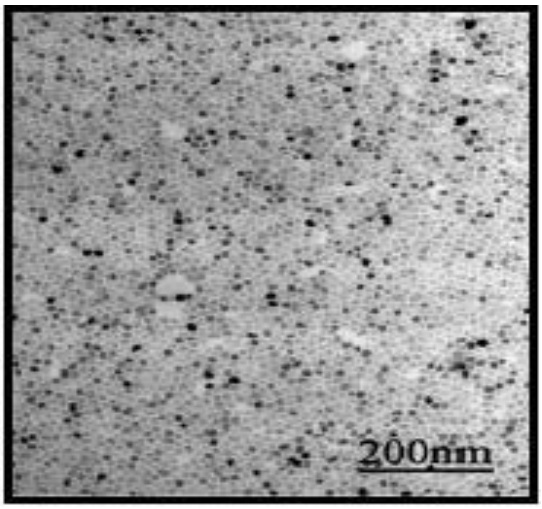

Fig. 5.1. A Transmission electronic Microscopy picture of the investigated water-based ferrofluid: WHKS 1S9-400Gauss supplied by Liquids Research Ltd, Limited Kingdom.

Magnetite nanoparticles in water **(W**HKS 1S9 – 400Gauss)					
M_∞ (kA/m)	K_a (kJ/ m^{-3})	M_s (kA/m)	d_m (nm)	size distribution (standard deviation)	coating
31.831	not supplied	318.310	10	lognormal (<0.4)	anionic

Tab. 5.1- Main physical features of the investigated water-based ferrofluid: WHKS 1S9-400 Gauss delivered by Liquids Research Ltd, Limited Kingdom.

consequently to allow a wideband spectroscopy of the magnetic permeability with an satisfactory degree of accuracy.

Furthermore, Fe_3O_4-NPs of 10 nm in size should be superparamagnetic therefore their magnetic losses and the frequencies at which the losses occur should be independent of the nature of the solvent containing the NPs and of the nature and thickness of the coating. This aspect is very important for biomedical applications of Fe_3O_4-NPs because the environment enclosing Fe_3O_4-NPs, the nature and thickness of the coating of NPs strongly vary depending on the type of biomedical application.

Moreover, d_m = 10 nm is the mean magnetic diameter of Fe_3O_4-NPs dispersed in the oil-based FFs investigated in literature (see Sec. 3.2). Accordingly, one can compare the measurement result reported in the next

section with experimental data reported in literature and so to investigate the influence of the solvent and the coating on the magnetic losses of superparamagnetic Fe_3O_4-NPs.

Finally, from theoretical considerations and the experimental data reported in literature it is expected that Fe_3O_4-NPs of 10 nm in size have the highest SLP in the frequency range 1 – 100 MHz, which is the range of interest for biomedical applications of Fe_3O_4-NPs.

5.2 Measurement results and discussion

The measurement results reported here have been obtained by using as measurement instrument a Vector Network Analser (VNA, Anritsu MS4623A/B). This instrument when operating in one-port mode enables to directly measure the magnitude and phase of the reflection coefficients required by the S/OCL multi-cells inversion procedure to extract the complex permittivity and permeability of the sample (see Sec. 4.3).

In order to reduce the measurement uncertainty, ε_r and μ_r of the sample have been estimated by performing an arithmetical average over six measurement data sets.

The frequency spectrum analyzed is 10 MHz – 2 GHz. However, preliminary measurements over the frequency range 10 – 100 MHz, by using an electrically short sample of 8mm, has been also carried out. The aim is to acquire information on the electromagnetic parameters of the samples in order to choose the sample lengths to be used when measuring on the frequency spectrum 10 MHz – 2 GHz.

The measurement results in the band 10 – 100 MHz are shown in Figs. 5.2 and 5.3.

As can be seen from Fig. 5.2, the experimental values of μ'_r and μ''_r (red lines) are appreciably different from the values of the free space relative permeability, indicating a significant response of the suspended Fe_3O_4-NPs over the analyzed frequency spectrum. Furthermore, the obtained profiles of μ'_r and μ''_r are suitably fitted by the following two poles Debye complex function (black lines in Fig.5.2):

$$\mu_r(f) = \mu_{r\infty} + \frac{\chi_{01}}{1 + j2\pi f\tau_1} + \frac{\chi_{02}}{1 + j2\pi f\tau_2} \tag{5.1}$$

where $j = \sqrt{-1}$, $\mu_{r\infty} = 1.39$, $\chi_{01} = 0.37$, $\chi_{02} = 0.32$, $\tau_1 = 7.2\times10^{-9}$ sec and $\tau_2 = 10^{-9}$ sec. The Debye fitting of eq. (5.1) is in full agreement with the

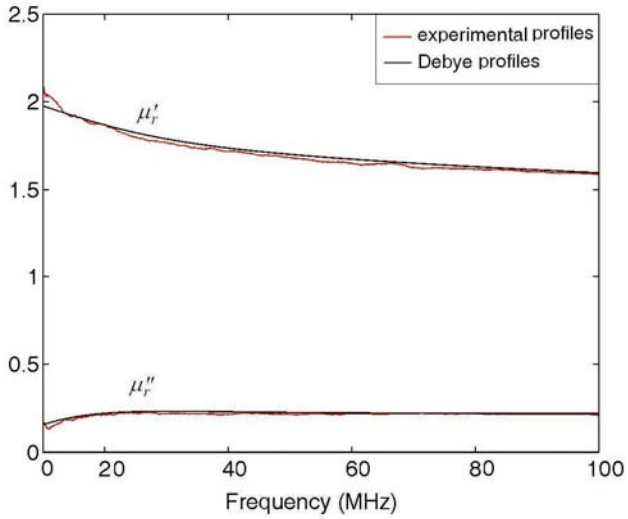

Fig. 5.2. Profile, over the frequency range 10 – 100 MHz, of μ'_r and μ''_r for the investigated water ferrofluid (red line) and comparison with two poles Debye complex function given in eq. (5.2) (black lines)

theoretical models discussed in Chapter 3, which predict a purely relaxation behaviour of a FF far from the frequency at which the ferromagnetic resonance occurs. Furthermore, according to eq. (5.1) the longest relaxation time of the suspended NP is 7.2×10^{-9}. Since the Brownian relaxation time of the suspended NP is much longer than 7.2×10^{-9} sec ($\tau_B \approx 7\times10^{-7}$, by assuming $\eta = 10^{-3}$ Pa sec and $\delta = 2$nm), one can conclude that the dominant relaxation mechanism for the analyzed WFF is the Néeel one. This result is consistent with theoretical models which predict a superparamagnetic behaviour for Fe_3O_4-NPs of 10nm in size in suspension.

Finally, it is worth noting that the obtained Debye fitting allows also to estimate μ'_r and μ''_r for frequencies below 10 MHz (10 MHz is the value of the minimum frequency analyzable by the used VNA), which are the most interesting frequencies in biomedical applications.

Concerning the profiles of the complex permittivity, from Fig. 5.3b (red line) one can note that the investigated WFF exhibits strong and unexpected dielectric losses over the entire analyzed frequency range, suitably fitted by the following hyperbolic function (black line in Fig. 5.3b):

$$g(f) = \frac{\sigma}{2\pi f \varepsilon_0} \tag{5.2}$$

where f is the frequency, ε_0 is the free space permittivity ($\varepsilon_0 = 8.85\times10^{-12}$

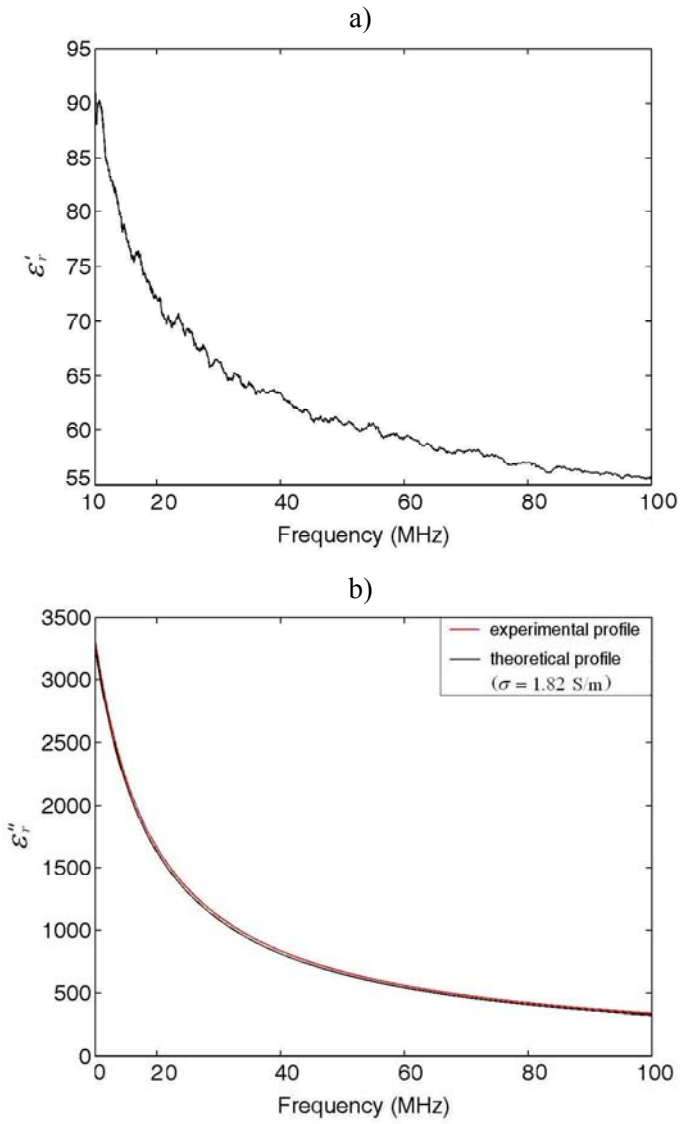

Fig. 5.3. a) Profile, over the frequency range 10 – 100 MHz, of ε'_r for the investigated water ferrofluid; b) comparison between the frequency profile of ε''_r for the investigated water ferrofluid (red line) and the hyperbolic function given in eq. (5.1) (black line)

Farad/m) and σ = 1.82 Siemens/m. Accordingly, the experimental investigation has highlighted a conductive behaviour of WFF, likely due to the presence of salts dispersed in solution.

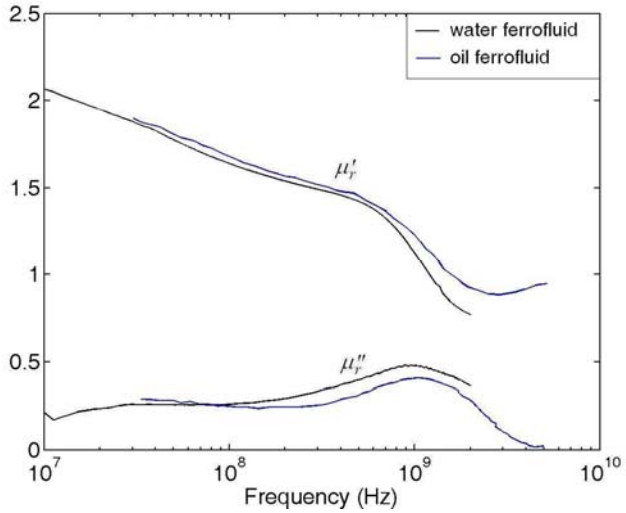

Fig. 5.4. Profiles, over the frequency range 10 MHz – 2 GHz, of μ'_r and μ''_r for the investigated water ferrofluid (black lines) and comparison with the profiles of μ'_r and μ''_r for the oil ferrofluid investigated in [56] (blue lines).

From the experimental data over the frequency range 10 – 100 MHz one can conclude that the investigated FF is characterized by strong dielectric losses. Moreover, from the fitting of the experimental profile of ε''_r it is expected that high dielectric losses occur also over the frequency spectrum 100 MHz – 2 GHz. Since the resonant-like behaviour characterizing the S/OCL technique takes place only for lossless or low losses samples, it is expected that this effect does not occur in the case of the investigated WFF. Therefore, the measurement over the frequency band 10 MHz – 2 GHz has been carried out by using one sample length, of 16mm. The results are reported in Figs. 5.4 and 5.5.

Fig. 5.4 shows the frequency profiles of μ'_r and μ''_r (black lines). As can be seen, up to 100 MHz it is confirmed the behaviour shown in Fig. 5.2 and hence the considerations on the dissipation mechanisms previously discussed. Above 100 MHz, one can note that at $f \approx 1.5$ GHz μ'_r becomes lesser than one, while at $f \approx 1$ GHz μ''_r exhibits a maximum. This resonant-like behaviour is indubitably related to the phenomenon of ferromagnetic resonance, which for Fe_3O_4-NPs occurs at 1 – 2 GHz. Accordingly, the profile of the magnetic permeability of the investigated WFF is in full agreement with the theoretical models discussed in Chapter 3.

In Fig. 5.4 it is also shown the comparison between the frequency profiles of μ'_r and μ''_r for the investigated WFF (black lines) and those reported in Fig. 3.8 (blue lines) and referred to a FF consisting of the same Fe_3O_4-NPs

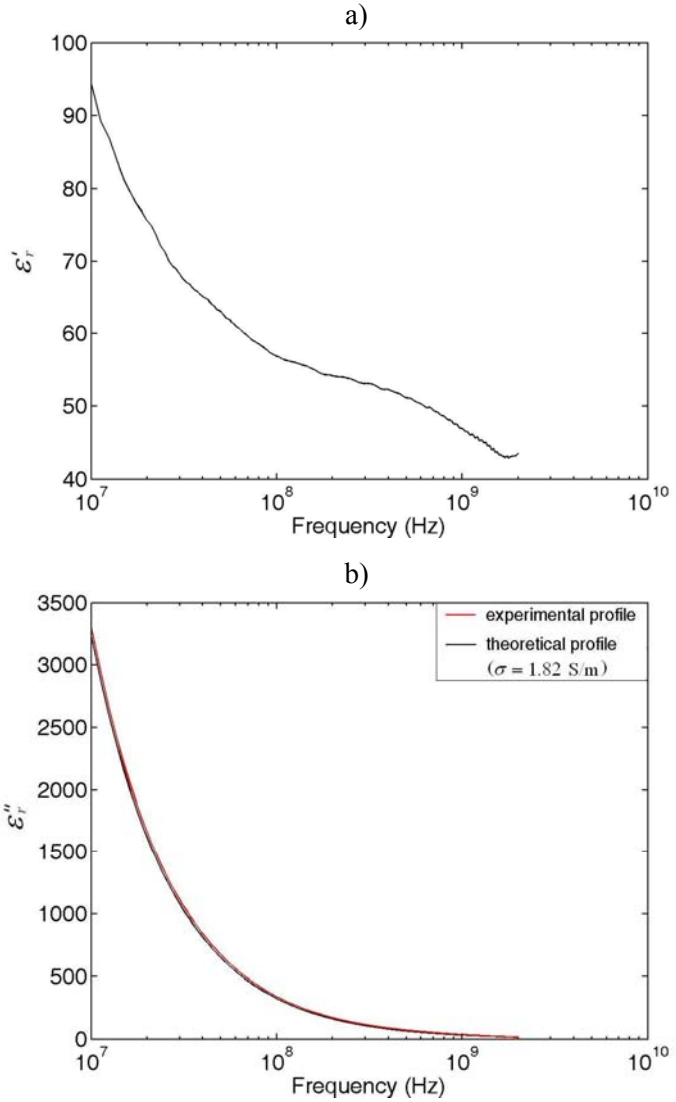

Fig. 5.5. a) Profile, over the frequency range 10 MHz – 2 GHz, of ε'_r for the investigated water ferrofluid; b) comparison between the frequency profile of ε''_r for the investigated water ferrofluid (red line) and the hyperbolic function given in eq. (5.1) (black line)

(the volumetric concentration of magnetite in solution is 10%), but dispersed in iso-paraffin [56]. As can be noted, there is a satisfactory overlapping between the profiles for both μ'_r and μ''_r, with a small discrepancy likely due to a small difference in the particle size distribution. Since the two FFs

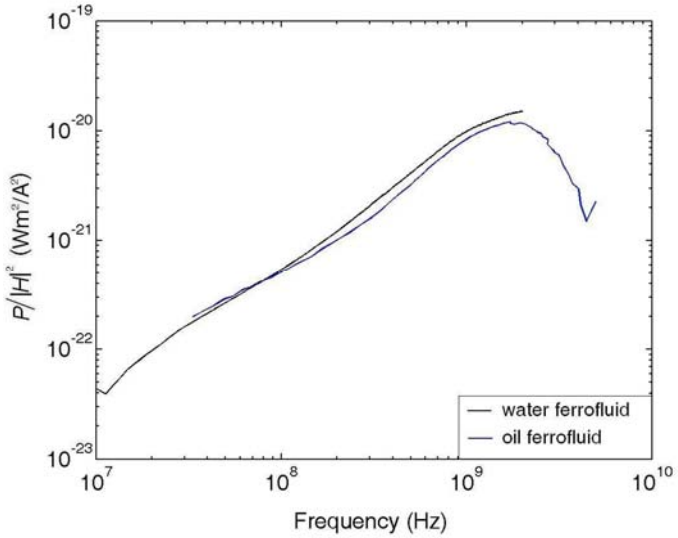

Fig. 5.6. Profiles, over the frequency range 10 MHz – 2 GHz, of the mean magnetic power absorbed by each Fe_3O_4-NP dispersed in the investigated water ferrofluid, normalized to the square of magnetic field strength, $|H|^2$.

substantially differ only for the carrier liquids (water and iso-paraffin), this result confirms that as long as the suspended NP are superparamagnetic, their magnetic properties are independent of the nature of the solvent and coating.

Fig. 5.5a-b show the frequency profiles of ε'_r and ε''_r, respectively. As can be seen from Fig. 5.5b, it is confirmed the existence of strong dielectric losses in solution up to 2 GHz, well fitted by the function given in eq. (5.2). This result consolidates the hypothesis of the presence of salts dispersed in solution, which make the solution conductive.

Finally, in Fig. 5.6 it is plotted the profile of the mean magnetic power absorbed by each Fe_3O_4-NP dispersed in the investigate WWF (black line), normalized to the square of MF strength, $|H|^2$. As can be seen from Fig. 3.9, also for the analyzed WFF, above 20 MHz, the mean magnetic power absorbed by a single suspended NP is larger than 10^{-22} Jm^2/A^{2}sec. Therefore, it is sufficient a MF-amplitude of few tens of A/m to dissipate, in one second, an amount of energy of about 10^{-19} J, i.e. the energy required to dehybrydize the DNA molecule used in [5]. Accordingly, it is confirmed the high capabilities of Fe_3O_4-NPs to absorb the energy transported by an applied MF, also in the case of solvents compatible with the biological applications like water.

5.3 Conclusions on the measurement results

In this Chapter the results of a broadband spectroscopy, over the frequency range 10 MHz - 2 GHz, of the electromagnetic parameters of a suspension of 10 nm Fe_3O_4-NPs in water are presented and discussed.

The used measurement method and equipment are the S/OCL multicells technique and apparatus presented in Chapter 4.

The aim of the experimental investigation has been to acquire information, over a frequency spectrum as large as possible, on the magnetic properties of Fe_3O_4-NPs dispersed in a biocompatibile solvent, never investigated till now in literature.

The investigation has highlighted the existence of strong and unexpected dielectric losses over the entire analyzed frequency spectrum, well fitted by an hyperbole, likely caused by the presence in solution of salts which make the suspension conductive.

Concerning the magnetic permeability, the investigation has shown a Debye-like profile up to 100 MHz and a resonant-like profile at about 1 GHz. The low frequency profile is essentially due to the Néel relaxation of the suspended NP, while the high frequency profile is mainly related to the phenomenon of ferromagnetic resonance. Moreover, the frequency at which the peaks of μ''_r occur are consistent with the theoretical predictions.

To investigate the influence of the solvent and the coating on the magnetic properties of superparamagnetic Fe_3O_4-NPs, a comparison between the profiles of μ'_r and μ''_r for the investigated WFF and those referred to a suspension of same Fe_3O_4-NPs but dispersed in iso-paraffin has been performed. The comparison has shown that for superparamagnetic NP the magnetic properties are actually independent of the nature of the solvent and coating, as predicted by the theoretical models.

In addition, the comparison has highlighted the high accuracy of the S/OCL technique and apparatus in estimating of the magnetic permeability of WFF, also in presence of strong dielectric losses as happens in this case.

Finally, from the measurement result has been estimated the mean magnetic power absorbed by each dispersed Fe_3O_4-NP of the investigate WFF, normalized to the square of MF strength, $|H|^2$. The estimation has confirmed the high capabilities of Fe_3O_4-NPs to absorb the energy transported by an applied MF, also in the case of biocompatible solvents like water and so the possibility to exploit them in biomedical applications.

5.4 Final considerations on the remote control of biological nanomachines

The theoretical and experimental investigations led in Chapters 2, 3 and 5 have shown that, unlike AuNPs used in [5], Fe_3O_4-NPs are able to dissipate an amount of energy sufficient to activate the function of most of biological macromolecules (including the DNA molecule used in [5]) at more biologically tolerable frequencies and MF amplitudes.

Accordingly, Fe_3O_4-NPs could be fruitfully used to remotely control BNMs, by exploiting the interaction mechanism proposed in [5].

However, even exploiting this type of NPs, the thermal mechanism proposed in [5] remains unable to induce the observed phenomenon. In fact, as shown in [76], the heat dissipation by nanometer size objects, like Fe_3O_4-NPs, is so efficient to produce a negligible heating outside the object.
Hypotheses of a direct heat transfer from the NP to bio-molecule, via linker, or a global hating of the bio-molecule are also to be rejected because the relaxation times by which the DNA dissipates the thermal energy in the solvent are too short [77] to allow a storage of energy large enough to dehybridize the DNA. Finally, a direct action on the groups involved in the bindings is also improbable, being hardly supposed a significant coupling at the exploitable frequencies and intensities of the field [77].

Accordingly, from the above results one can conclude that to concretely realize remotely controlled BNMs, by means of RF EMFs, other interaction mechanisms, different from the one proposed in [5], must be exploited.

Chapter 6

Electromagnetic field and magnetic nanoparticle design for applications in anticancer hyperthermia

As discussed in Chapter 1, one of main aims in MFH is to minimize the amount of Fe_3O_4-NPs to be administered in the treatment (therapeutic dose) to reach the therapeutic temperature distribution inside and outside the tumour.

The main benefits obtainable by minimizing the therapeutic dose of Fe_3O_4-NPs are:

a) a smaller amount of Fe_3O_4-NPs to be administered and consequently to be expelled after MFH treatment.

b) possibility of using techniques of MNP-targeting more efficient than the intra-tumoural injection, but able to deliver a smaller amount of Fe_3O_4-NPs.

Concerning point b), currently, the most used technique of NP administration is the direct injection of Fe_3O_4-NPs inside the diseased tissue (intra-tumoural injection). Although this approach allows to concentrate a large amount of Fe_3O_4-NPs at the cancer site (up to some hundreds of milligram per millilitre [13]), it is applicable only to well-localized and easily-accessible tumours in the body. Moreover, once injected, Fe_3O_4-NPs do not keep localized at the target site, but spread toward the surrounding healthy tissue [14]. The latter aspect drastically reduces the heating-selectivity of MFH.

An emerging and promising way to deliver Fe_3O_4-NPs to the cancer site is to functionalize them with specific bio-molecules (like proteins, peptides, nucleic acid, hormones, antibodies etc), able to bind only to target cells, and to administer them via intravenous injection [2].

This modality of targeting is very attractive because enables to selectively accumulate Fe_3O_4-NPs only at the cancer sites and to keep them therein localized. Furthermore, by exploiting the cardiovascular system it is possible to transport Fe_3O_4-NPs anywhere in the body.

Accordingly, the MFH could be notably improved by adopting the described modality of MNP-targeting. However, this method does not allow to accumulate in the tumour the high NP-concentrations reachable in the case of intra-tumoural injection [9]. Therefore, to exploit this approach it is crucial to reduce as much as possible the effective therapeutic dose of Fe_3O_4-NPs to be supplied to the cancer to obtain the required temperature raise.

A way to reduce the therapeutic dose of Fe_3O_4-NPs is to increase their SLP. According to the theoretical and experimental results reported in Chapters 3 and 5, the SLP can be enhanced by increasing the amplitude, $|H|$, and/or frequency, f, of the applied MF. However, the product $|H|f$ cannot be arbitrary large since higher the product $|H|f$ larger the intensity of the EF component, $|E|$, of the applied EMF and consequently the heating, produced via Joule effect, in the healthy tissues surrounding the tumour. This fact can be noted by considering, for example, the relationship between the axial components of the EMF produced by a coil: $|E| = \zeta\gamma(\omega)|H| = a(|H|f)$ (**) (see Appendix C). As can be seen from the formula, $|E|$ linearly increase with $|H|f$, although a coil is considered a "only magnetic field applicator".

In the open literature the values of f and $|H|$ are chosen by assuming that the product $|H|f$ does not exceed the safety value 4.85×10^8 A/ms, obtained through clinical trials. In fact, it has been experimentally found that below 4.85×10^8 A/ms the induced EF produces a tolerable heating in the surrounding healthy tissue [15]. However, this semi-empirical condition is much more restrictive than the one actually required in MFH, therefore it strongly reduces the range of values of f and $|H|$ exploitable in the treatment and consequently the possibility of reducing the therapeutic dose of magnetite by increasing SLP of Fe_3O_4-NPs.

Accordingly, from the above considerations one can conclude that to minimize the therapeutic dose of Fe_3O_4-NPs to be administered in MFH two points have to be addressed:

1) designing of exposition apparatuses with a proportionality factor, a, between the EF intensity and $|H|f$ as small as possible in order to minimize the heating produced by the EF in the healthy tissues, fixed a value for $|H|f$.
2) Development of criterions to individuate the actual constraint on the product $|H|f$.

In this Chapter the attention has been focused on point 2). In particular, by exploiting a thermal approach it has been developed a criterion that

(**) The quantity a represents the coefficient of the linear term of the MacLaurin series expansion of the function $\zeta\gamma(\omega)$, defined in Appendix C

allows to determine the actual levels of the mean magnetic and electric power densities, say p_m and p_e, to be dissipated in diseased and neighbouring healthy tissues to reach the therapeutic pattern of temperature inside and outside the diseased tissue. These quantities are of interest in that, as it will be shown in Sec. 6.2, their knowledge allows to determine the actual constraint on the product $|H|f$ and consequently the values of $|H|$, f, d (d is the magnetic size of the Fe_3O_4-NPs) minimizing the therapeutic dose of Fe_3O_4-NPs to be administered in MFH.

6.1 Criterion to selectively heat cancer in hyperthermia

As discussed in Chapter 1, MFH treatment should assure the therapeutic temperature enhancement only within the diseased area leaving unaffected the surrounding healthy tissue. In other words, a temperature distribution where all the diseased tissue is at a therapeutic temperature and all the healthy tissue is at the normal body temperature of 37 °C should be attained.

Accordingly, the ideal temperature pattern in MFH should have the red profile shown in Fig. 6.1. (for the sake of simplicity, the plots in Fig. 6.1 refer to the case of a spherical geometry for the tumour and surrounding healthy tissue, where R_1 and R_0 represent the radii of the tumour and the neighbouring healthy tissue, respectively). However, due to the finite thermal conductivity of biological tissues and the heating generated by the unavoidable presence of the EF in the healthy tissue, the actual profile of the temperature, T, achievable in MFH is always characterized by a non uniform value in the tumour and by a non null transition region, $\Delta r = R_2 - R_1$, wherein T decreases from a therapeutic value T_1 ($T_1 \geq 42$ °C) to a smaller, safety, value T_2 (blue line in Fig. 6.2). Accordingly, p_m and p_e should be determined by requiring that T is as much as possible close to the ideal profile (red line in Fig. 6.2).

As a matter of fact, although a uniform temperature in the tumour is desirable in order to have the same therapeutic conditions in all the diseased area, this requirement is not strictly needed in MFH. Much more important is to reduce the transition region width in order to increase the heating

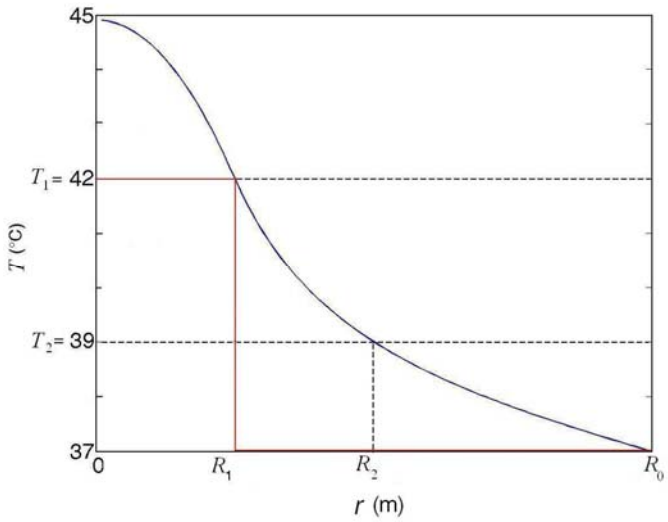

Fig. 6.1. Ideal (red line) and real (blue line) profiles versus radius, r, of the temperature in magnetic fluid hyperthermia. The plots refer to the case of a spherical geometry for the tumour and surrounding healthy tissue (see Fig. 6.2).

selectivity of the treatment. Therefore, p_m and p_e can be determined by requiring only that the transition region width, Δr, has an assigned value, i.e. by imposing that: $T \geq T_1$ for $r \leq R_1$ and $T \leq T_2$ for $r \geq R_2$, where the value of Δr depends on the desired degree of heating selectivity of the MFH treatment. This is the criterion proposed here to estimate the values of p_m and p_e. More specifically, the proposed criterion estimates p_m and p_e by modelling the tumour and the surrounding healthy tissues as two finite concentric regions and assuming a time-constant and spatial-uniform value for the temperature outside these regions. The first assumption is consistent with the finite size of the human body; the second assumption is consistent with the thermo-regulating action of the body outside the region exposed to the applied field and/or with the use in the treatment of thermostatic baths to limits the heating in the healthy tissues.

It is worth noting that the determination of p_m and p_e for a tumour of arbitrary shape is, generally, not a easy task and the solution should not be expressible in an analytical form. In these cases a numerical solution, by using properly numerical simulator, is needed.

An analytical expression or p_m and p_e can be obtained only when particular geometry for the diseased and healthy tissues are considered. This happens, for example, for a spherical or cylindrical geometry and when a step-like heat generation is assumed.

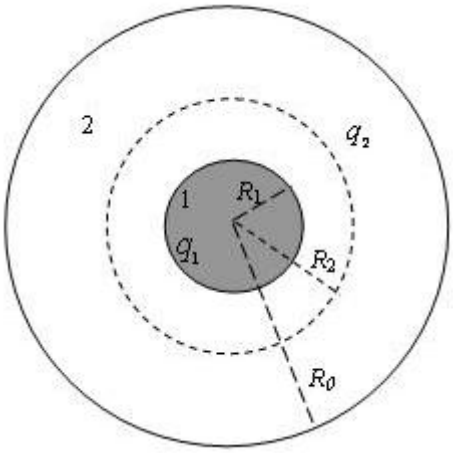

Fig. 6.2. Geometry of the tumour (gray region) and surrounding healthy tissue (white region)

As an example, in the next section are derived the analytical expressions of p_m and p_e in the case of a spherical geometry and a step-like heat generation. This example is of interest because in many practical cases, tumours have a shape close to a sphere.

6.1.1 Expression of p_m and p_e in the case of a spherical geometry and a step-like heat generation

In Fig. 6.2 it is shown a schematization of the geometry assumed for the tumour and the surrounding healthy tissue. In particular, the inner sphere, of radius R_1, represents the tumour (gray region), while the outer sphere, of radius R_0, represents the neighbouring healthy tissue (white region). The region between the spheres of radii R_1 and R_2 represents the transition region. The first step to determine the expressions of p_m and p_e such that $T \geq T_1$ for $r \leq R_1$ and $T \leq T_2$ for $r \geq R_2$ is to derive the expression of, T, in both diseased and neighbouring healthy tissues, as a function of p_m and p_e.

Here this task is accomplished by describing the thermal balance therein by means of the Pennen's Bio-Heat transfer Equation (PBHE), in spherical symmetry [78]:

$$\rho c \frac{\partial T(r,t)}{\partial t} = k \frac{1}{r^2} \frac{\partial}{\partial r}\left(r^2 \frac{\partial T(r,t)}{\partial r} \right) - w_b c \left(T(r,t) - T_0 \right) + q \tag{6.1}$$

In eq. (6.1) t is the time ([t] = sec), r is the radius ([r] = m), ρ is the human-tissue density ([ρ] = kg/m^3), c is the specific heat capacity of human tissues ([c] = J/°C kg), k is thermal conductivity of human tissues ([k] = watt/°C m), w_b is the blood perfusion ([w_b] = kg/m^{3}sec), T_0 is the normal human-body temperature (T_0 = 37 °C) and q is the power density generation ([q] = watt/m^3).

PBHE differs from the standard heat transfer equation for the presence of the convection term, $w_b c(T-T_0)$, which takes in account of the heat carried away from tissues by the bloodstream. Accordingly, PBHE describe the heat transfer *in vivo* much more accurately than the standard heat transfer equation.

The thermal analysis here presented has also assumed:

1) same values for k, ρ, c and w_b for both diseased and healthy tissues (homogenous medium);
2) A time-constant and spatial-uniform value of T, equal to T_0, over the spherical surface of radius R_0;

Condition 1) is quite verified as long as the therapeutic concentration of Fe_3O_4-NPs in the tumour is small enough to not significantly affect the thermal properties of the tissue. Condition 2) is consistent with the modelling of the tumour and neighbouring healthy tissue adopted by the proposed criterion.

Accordingly, the thermal problem to be solved to determine the temperature field within the diseased and healthy tissues (regions 1 and 2 of Fig. 6.2), as a function of p_m and p_e, consists of the equation (6.1), with the following step-like heat generation:

$$q = \begin{cases} p_e + p_m & 0 \le r \le R_1,\ t \ge 0 \\ p_e & R_1 \le r \le R_0,\ t \ge 0 \end{cases} \tag{6.2}$$

and the following initial and boundary conditions:

$$T(r,0) = T_0 \tag{6.3}$$

$$T(R_0,t) = T_0 \tag{6.4}$$

From eq. (6.2) one can note that the magnetic power dissipation is assumed localized only within the diseased area, whereas the electric power dissipation is present in both the diseased and healthy tissues. These assumptions are consistent with the presence of Fe_3O_4-NPs only within the

tumour and the presence of a finite electric conductivity in both cancerous and normal tissues.

Concerning the initial and boundary conditions, eq. (6.3) (initial condition) is derived by noting that before MFH treatment all the body is at $T = T_0$; eq. (6.4) (boundary condition) is consistent with assumption 2).

It can be proved that the solution of the set of eqs. (6.1) – (6.4) has the expression (see Appendix E):

$$\begin{aligned} &T(\xi,\tau) = T_0 + T_0 p'_m \sum_{n=1}^{+\infty} \frac{q_{m,n}}{n^2\pi^2+\beta}\left(1-\exp\left(-\left(n^2\pi^2+\beta\right)\tau\right)\right)\sin\left(n\pi\xi\right)/\xi + \\ &T_0 p'_e \sum_{n=1}^{+\infty} \frac{q_{e,n}}{n^2\pi^2+\beta}\left(1-\exp\left(-\left(n^2\pi^2+\beta\right)\tau\right)\right)\sin\left(n\pi\xi\right)/\xi = \\ &T_0\left(1+p'_m f_m(\xi,\tau)+p'_e f_e(\xi,\tau)\right) \end{aligned} \tag{6.5}$$

where:

$$q_{m,n} = \frac{2}{(n\pi)^2}\left(\sin\left(n\pi\frac{R_1}{R_0}\right) - n\pi\frac{R_1}{R_0}\cos\left(n\pi\frac{R_1}{R_0}\right)\right) \tag{6.6}$$

$$q_{e,n} = (-1)^{n+1}\frac{2}{n\pi} \tag{6.7}$$

and where: $\xi = r/R_0$, $\tau = (\alpha/R_0)^2 t$, $\alpha=(k/\rho c)^{1/2}$, $\beta = w_b c R_0^2/k$, $p'_{m[e]} = (R_0^2/kT_0)p_{m[e]}$.

As can be noted, eq. (6.5) directly relates the temperature field in the regions 1 and 2 to p'_m and p'_e, therefore, it can be successfully exploited to determine p'_m and p'_e such that: $T(\xi, \tau) \geq T_1$ for $\xi \leq \xi_1$ and $T(\xi, \tau) \leq T_2$ for $\xi \geq \xi_2$,

Since the temperature field $T(\xi, \tau)$ given in eq. (6.5), at any normalized time τ, monotonically decreases with ξ (see Appendix E), the values of p'_m and p'_e, satisfying the above inequalities, are obtained by simply solving the following set of linear equations:

$$\begin{cases} T(\xi_1,\tau) = T_0\left(1+f_m(\xi_1,\tau)\,p'_m + f_e(\xi_1,\tau)\,p'_e\right) = T_1 \\ T(\xi_2,\tau) = T_0\left(1+f_m(\xi_2,\tau)\,p'_m + f_e(\xi_2,\tau)\,p'_e\right) = T_2 \end{cases} \tag{6.8}$$

where $f_m(\xi,\tau)$ and $f_e(\xi,\tau)$ are given in eq. (6.5).

From eqs. (6.8) one obtains the following expressions for p'_m and p'_e:

$$p'_m = \frac{1}{T_0}\frac{(T_1 - T_0) f_e(\xi_2, \tau) - (T_2 - T_0) f_e(\xi_1, \tau)}{f_m(\xi_1, \tau) f_e(\xi_2, \tau) - f_e(\xi_1, \tau) f_m(\xi_2, \tau)} \tag{6.9}$$

$$p'_e = \frac{1}{T_0}\frac{(T_2 - T_0) f_m(\xi_1, \tau) - (T_1 - T_0) f_m(\xi_2, \tau)}{f_m(\xi_1, \tau) f_e(\xi_2, \tau) - f_e(\xi_1, \tau) f_m(\xi_2, \tau)} \tag{6.10}$$

Fixed τ, eqs. (6.9) and (6.10) provide the actual levels of p'_m and p'_e to be dissipated in the diseased and surrounding healthy tissues to obtain, on an exposition time τ, a value of temperature larger than T_1 for $\xi \le \xi_1$ and smaller than T_2 in $\xi \ge \xi_2$. In other word, eqs. (6.9) and (6.10) provide the mean values of the magnetic and electric power densities required to reach in $t = (R_0/\alpha)^2 \tau$ seconds the therapeutic pattern of temperature inside and outside the tumour.

Fig. 6.3a shows the time-profiles of p'_m and p'_e obtained by assuming T_1 = 42 °C, T_2 = 39 °C, ξ_1 = 1/4, $\Delta\xi$ = 1/4, and by adopting for k, ρ, c, w_b the typical values of human tissues, i.e. $\rho \approx 1000$ kg/m^3, $c \approx 4200$ J/°C kg, $k \approx 0.5$ watt/°C m, $w_b \approx 1$ kg/m^{3}sec [78]. In Fig. 6.3b it is plotted the corresponding time-profiles of the ratio p'_m/p'_e.

As can be seen from Fig. 6.3 the minimum values of p'_m and p'_e are assumed when τ approaches infinity (steady regime). On the contrary, the minimum value of the ratio p'_m/p'_e is assumed when τ approaches zero. As a results, it is convenient to work on long exposition times if the objective is to minimize the values of p'_m and p'_e, whereas it is convenient to work on short exposition times and large values of p'_m and p'_e if the aim is to minimize the ratio p'_m/p'_e.

As a matter of fact, in MFH the optimal treatment duration is the one that minimize the therapeutic dose of Fe_3O_4-NPs.

6.2 Electromagnetic field and nanoparticle design

In this section it is shown how to use the values of p'_m and p'_e, achieved from the criterion discussed in Sec. 6.1, to identify the actual constraints on the product $|H|f$, required in MFH, and the optimal values for f, $|H|$ and d to

a)

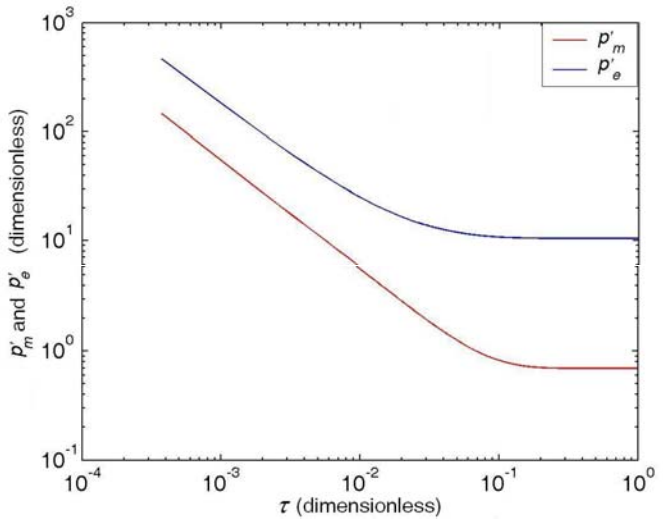

b)

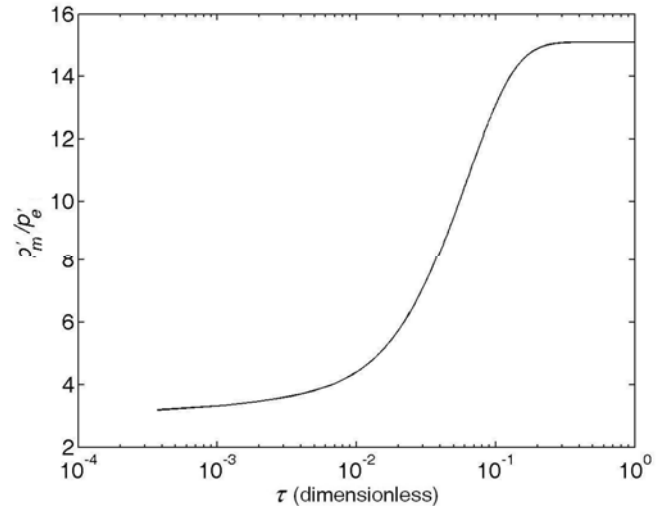

Fig. 6.3. a) Time-profiles of p'_m (blue line) and p'_e (red line); b) time-profile of the ratio p'_m/p'_e. The profiles have been obtained for the geometry depicted in Fig. 6.2 and by setting T_1 = 42 °C, T_2 = 39 °C, ξ_1 = 1/4, $\Delta\xi$ = 1/4, $\rho \approx 1000$ kg/m^3, $c \approx 4200$ J/°C kg, $k \approx 0.5$ watt/°C m, $w_b \approx 1$ kg/m^{3}sec [78].

be used in the treatment (i.e. the values of f, $|H|$ and d minimizing the therapeutic dose of Fe_3O_4-NPs).

Concerning the constraints on the product $|H|f$, once the exposition apparatus to be used in the treatment has been defined, i.e. once the

proportionality factor, $a(\mathbf{r})$, between $|E|$ and $|H|f$ has defined, the mean power density dissipated by the EF inside and outside the diseased tissue is given by:

$$\frac{1}{V}\iiint_V \frac{\sigma_t}{2}\left|E(\mathbf{r})\right|^2 dV = \frac{1}{V}\iiint_V \frac{\sigma_t}{2} a^2(\mathbf{r})\left|H(\mathbf{r})\right|^2 f^2 dV = \frac{\sigma_t}{2} A\left|H_0\right|^2 f^2 \tag{6.11}$$

where:

$$A = \frac{1}{V}\iiint_V a^2(\mathbf{r})\frac{\left|H(\mathbf{r})\right|^2}{\left|H_0\right|^2} dV \tag{6.12}$$

and where V is the volume of regions exposed to the EF, $|H_0|$ is the MF-amplitude acting on the tumour(*) and σ_t is the electric conductivity of the biological tissues ($\sigma_t \approx 0.5$ Siemens/m for muscles [79]).

Accordingly, to guarantee the desired temperature enhancement inside and outside the tumour, one has to impose:

$$\frac{\sigma_t}{2} A\left|H_0\right|^2 f^2 = p_e = p'_e \frac{kT_0}{R_0^2} \tag{6.13}$$

where p'_e is obtained by imposing the criterion described in Sec. 6.1. Eq. (6.13) represents the constraint required in MFH on the product $|H|f$.

It must be stressed that smaller the value of A larger the value of $|H|f$ exploitable in the treatment and consequently the SLP of Fe_3O_4-NPs. Accordingly, to reduce the therapeutic dose of Fe_3O_4-NPs to be used in the MFH, a crucial step is to design exposition apparatuses with a proportionality factor, a, as small as possible.

As an example, in Fig. 6.4 it is plotted the time profile of $R_0^2|H|f$, obtained by exploiting the profile of p'_e shown in Fig. 6.3a (red line), by assuming uniform the MF inside and outside the tumour (i.e. regions 1 and 2 in Fig. 6.2) and by adopting the following expression for a, in spherical coordinates (r, θ, ϕ):

$$a(r,\theta,\phi) = \pi\mu_0(r\sin\theta) \tag{6.14}$$

For every τ, the plot in Fig. 6.4 gives the value for $|H|f$ (normalized to the

(*) It is assumed a uniform MF over the entire diseased area. This assumption is quite verified as long as the tumour-size is much smaller than the wavelength of the applied field

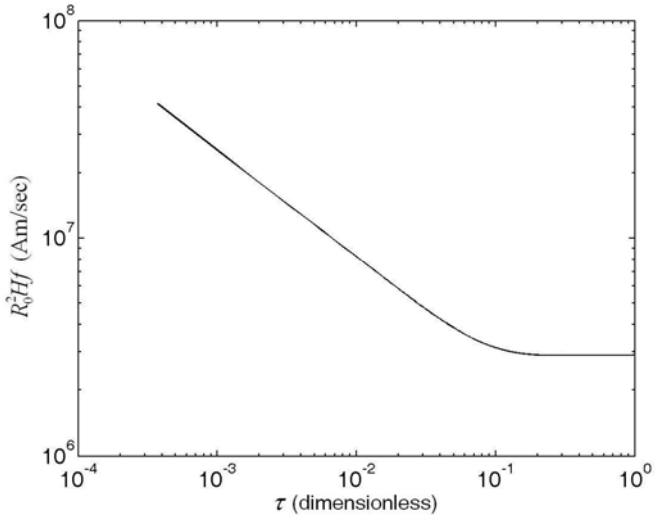

Fig. 6.4. Time-profile of Hf, normalized to the quantity $1/R_0^2$. The profile has been obtained for the geometry depicted in Fig. 6.2 and by setting $T_1 = 42$ °C, $T_2 = 39$ °C, $\xi_1 = 1/4$, $\Delta\xi = 1/4$, $\rho \approx 1000$ kg/m^3, $c \approx 4200$ J/°C kg, $k \approx 0.5$ watt/°C m, $w_b \approx 1$ kg/m^{3}sec [78].

quantity $1/R_0^2$) to be exploited in MFH to reach, on an exposition time τ, the desired temperature rise in the region 1 and 2 of Fig. 6.2.

Concerning the optimal values for f, $|H|$ and d, say $|H|_{opt}$, f_{opt} and d_{opt},, the theoretical expression of the mean magnetic power density absorbed by a suspension of Fe_3O_4-NPs, when immersed in a uniform MF of magnitude $|H_0|$ and frequency f, is given by (see Chapter 3):

$$\mu_0 \pi f \chi''(f,\sigma)\left|H_0\right|^2 = C\frac{\left(\mu_0 M_s\right)^2}{6K_a}\frac{\left(2\pi f\left|H_0\right|\right)^2}{1+\left(2\pi f\tau_{eff}(\sigma)\right)^2}\frac{F_1(\sigma)}{F_0(\sigma)}\sigma\tau_{eff}(\sigma) \tag{6.15}$$

where C is the volumetric concentration of Fe_3O_4-NPs (for the other quantities involved in eq. (6.15) let us refer to the definitions given in Chapter 3).

Accordingly, to assure the desired temperature enhancement inside and outside the tumour one has to impose:

$$C\frac{\left(\mu_0 M_s\right)^2}{6K_a}\frac{\left(2\pi f\left|H_0\right|\right)^2}{1+\left(2\pi f\tau_{eff}(\sigma)\right)^2}\frac{F_1(\sigma)}{F_0(\sigma)}\sigma\tau_{eff}(\sigma) = p_m = p'_m\frac{kT_0}{R_0^2} \tag{6.16}$$

where p'_m is obtained from the criterion described in Sec. 6.1.
From eq. (6.16) it follows that:

$$C = \frac{6K_a}{\left(\mu_0 M_s\right)^2} \frac{1+\left(2\pi f \tau_{eff}\left(\sigma\right)\right)^2}{\left(2\pi f \left|H_0\right|\right)^2 \sigma \tau_{eff}\left(\sigma\right)} \frac{F_0\left(\sigma\right)}{F_1\left(\sigma\right)} p'_m \frac{kT_0}{R_0^2} \tag{6.17}$$

Eq. (6.17) provides the values of C required in MFH treatment to reach the therapeutic pattern of temperature inside and outside the tumour.
Accordingly, $|H|_{opt}$, f_{opt} and d_{opt} (*) to be used in MFH treatment are obtained by minimizing the quantity on the right hand of eq. (6.17).

Obviously, the values f and $|H_0|$ in eq. (6.17) cannot be arbitrary but they must satisfy the constraint (6.13).

By taking in account eq. (6.13), the expression (6.17) becomes:

$$C = \frac{3A\sigma_t K_a}{4\left(\pi\mu_0 M_s\right)^2} \frac{1+\left(2\pi f \tau_{eff}\left(\sigma\right)\right)^2}{\sigma \tau_{eff}\left(\sigma\right)} \frac{F_0\left(\sigma\right)}{F_1\left(\sigma\right)} \frac{p'_m}{p'_e} \tag{6.18}$$

From eq. (6.18) one can easily note that, fixed σ, C monotonically increases with f. Since f is proportional to $1/|H_0|$ (see eq. (6.13)), it follows that C decreases monotonically with $|H_0|$. As a result, the optimal value for $|H|$ coincides with the maximum value achievable for $|H|$, namely the maximum value reachable by exposition apparatuses (this value typically does not exceed 10-11 kA/m [8]).

Concerning the optimal value for f, once $|H|_{opt}$ has been identified, f_{opt} is obtained by putting $|H_0| = |H|_{opt}$ in eq. (6.13) and calculating the corresponding value of f.

Finally, the optimal value of d is obtained by putting $f = f_{opt}$ in eq. (6.18) and searching the value of σ, say σ_{opt}, minimizing the quantity on the right hand of eq. (6.18).

As an example, in Fig. 6.5a-b are plotted the time profiles of f_{opt} and d_{opt} obtained by setting $|H|_{opt} \approx 7$ kA/m ($|H| = 7$ kA/m is the typical value for the MF amplitude quoted in open literature [8]), $R_0 = 4$ cm, and by exploiting the profile of p'_m/p'_e shown in Fig. 6.3b and the profile of $R_0^2 |H|f$ shown in Fig. 6.4. For every τ, the plots in Fig. 6.5a-b provide the value for f and d to be exploited in MFH to reach, on an exposition time interval τ, the therapeutic temperature rise in the region 1 and 2, with the minimum dose of magnetite, C_{min}. The corresponding values of C_{min} are shown in Fig. 6.6.
magnetite per cubic As can be seen from Fig. 6.6, the time profile of C_{min} exhibits a minimum at $\tau \approx 0.03$, whose value is about 2×10^{-4} corresponding

(*) the optimal value for d is achieved by determining the optimal value for the ratio $\sigma = K_a V_m / k_b T$, where V_m is the magnetic volume of the Fe_3O_4-NPs (see Chapter 3).

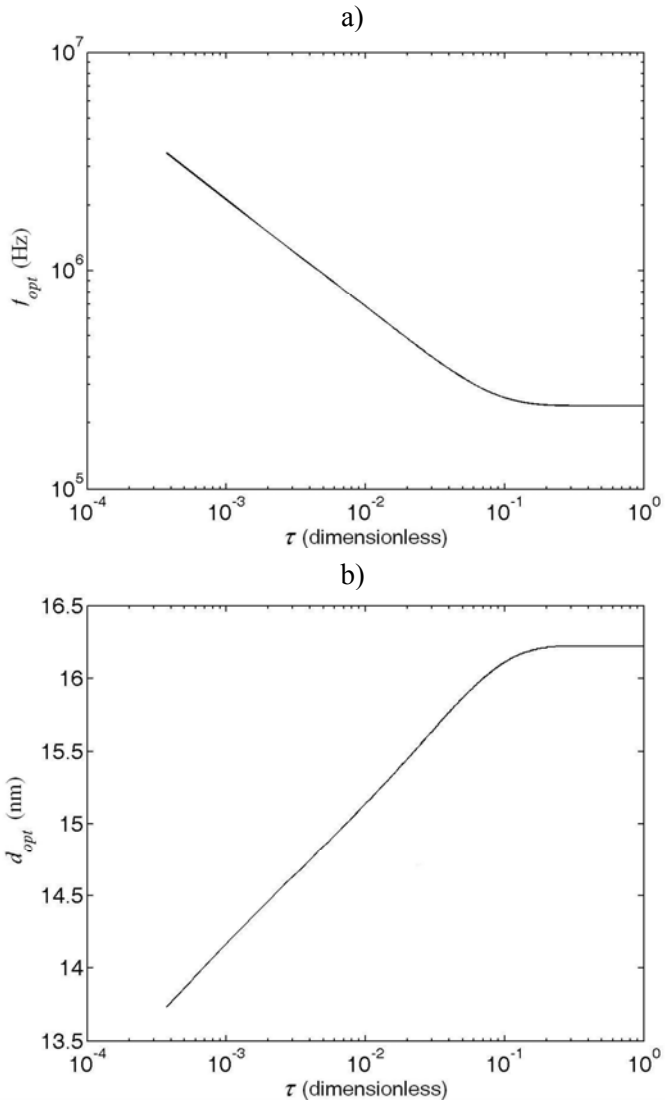

Fig. 6.5. a) Time-profile of the optimal frequency to be used in MFH treatment; b) time-profile of the optimal diameter of Fe_3O_4-NPs to be used in MFH treatment. The profiles have been obtained for the geometry depicted in Fig. 6.2 and by setting $T_1 = 42$ °C, $T_2 = 39$ °C, $\xi_1 = 1/4$, $\Delta\xi = 1/4$, $\rho \approx 1000$ kg/m^3, $c \approx 4200$ J/°C kg, $k \approx 0.5$ watt/°C m, $w_b \approx 1$ kg/m^{3}sec [78], $|H|_{opt} = 7$ kA/m, $R_0 = 4$ cm

to 1 milligram of magnetite per centimetre of tumour (the mass density of magnetite is about 5g/cm^3). The corresponding values of f_{opt} and d_{opt} are 400 kHz and 15.6 nm, respectively.

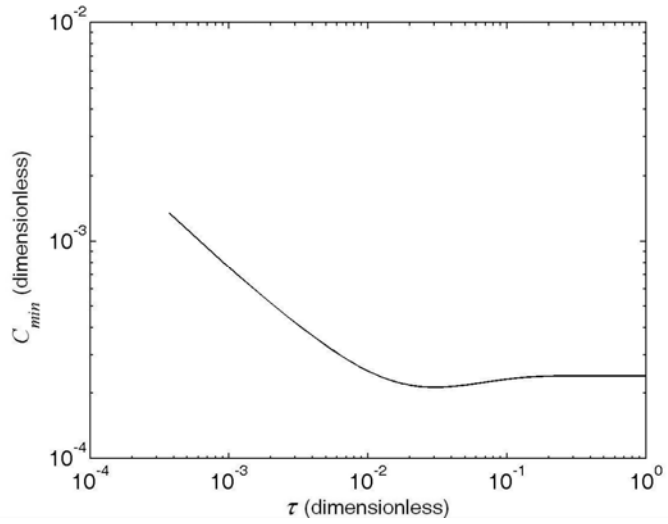

Fig. 6.6. Time-profile of C_{min} to be used in MFH treatment. The profile has been obtained for the geometry depicted in Fig. 6.2 and by setting $T_1 = 42$ °C, $T_2 = 39$ °C, $\xi_1 = 1/4$, $\Delta\xi = 1/4$, $\rho \approx 1000$ kg/m^3, $c \approx 4200$ J/°C kg, $k \approx 0.5$ watt/°C m, $w_b \approx 1$ kg/m^{3}sec [78], $|H|_{opt} = 7$ kA/m, $R_0 = 4$ cm

Accordingly, the therapeutic dose of magnetite can be further reduced by properly choosing the exposition time interval, namely the MFH treatment duration.

As a concluding remark, let us note that for the example here analyzed the minimum therapeutic dose of magnetite, 1 milligram per cubic centimetre of tumour, is much smaller than the ones usually used in open literature, which, for applied MF of comparable amplitude, are of order of tens milligram per cubic centimetre of tumour.

6.3 Conclusions

In this Chapter a criterion to estimate the levels of magnetic and electric power densities to be supplied in MFH treatment to reach the therapeutic temperature enhancement inside and outside the tumour has been presented. Furthermore, by exploiting the results of the criterion has been shown how to identify the actual constraints on *Hf*, required by MFH, and the values of *f*, *H* and *d* that minimize the therapeutic dose of Fe_3O_4-NPs.

Summary and Conclusions

In this final section are summarized and discussed the most interesting results obtained in this thesis on the possibility of using NPs and non optical EMF to:

- remotely control BNMs.
- selective heating cancerous tissues by means of hyperthermia.

Moreover, it is also provided a brief discussion on the future research in these fields.

Concerning the remotely control of BNMs, in this thesis, by using a classical macroscopic approach, it has been derived a simple and accurate expression quantifying the energy exchange between EMF and BNM. This expression represents an useful tool either to analyze the energy transfer mechanisms between applied field and BNM or in designing remotely controlled BNMs and the relative control equipments, for bio-medical applications.

By exploiting the obtained expression it has been analyzed the energy transfer mechanism proposed to explain the first and only experimental results, reported in literature, on the use of NPs and RF EMFs to remotely control BNMs: the Hamad-Schifferli's experiment [5]. The analysis has shown that the physical mechanism proposed in [5] to justify the experimental results, i.e. the local heating produced via Joule effect by the conduction currents induced on the AuNP, is unable to induce the observed effect because the corresponding energy transfer is many orders lower than the one required to effectively dehybridize the DNA molecule. This result has made questionable the possibility of using AuNPs to remotely control BNMs by means of RF EMFs. Therefore, the attention has been turned to MNPs, which seem to have such potentialities as suggested by their application in anticancer hyperthermia.

From an accurate analysis of the theoretical and experimental results available in literature on the magnetic properties of colloidal suspension of MNPs in oils, it has been shown that, unlike AuNPs used in [5], Fe_3O_4-NPs, of 10 nm in size, are able to absorb an amount of energy large enough to activate the functions of most of biological macromolecules. Therefore, magnetite-NPs seem to be promising candidates to remotely control BNMs.

However, the cited data could be not reliable, since they are referred to MNP-suspensions in non biocompatible liquids (oils), Suitable data can be surely obtained through a wideband spectroscopy of the magnetic susceptibility of Fe_3O_4-NPs in water (WFF), never investigated until now in open literature. Therefore, the attention has been addressed to the wideband spectroscopy of the magnetic properties of colloidal suspensions of WFFs. Preliminary measurements, performed with existing coaxial cable techniques like T/R or SCCL, have shown that the these methods are unable to accurately measure, on a wide frequency range, the magnetic properties of WFFs, because of the strongly dielectric response characterizing these substances compared with the magnetic one. Therefore, it has been needed to develop and realize a new measurement technique and apparatus able to overcome the bandwidth-accuracy limitations characterizing the existing coaxial cable techniques in measuring the permeability of substances like WFFs.

By exploiting this new measurement technique, a wideband spectroscopy of the magnetic permeability of commercially available WFF, consisting of Fe_3O_4-NPs of 10 nm in size, has been carried out. The measurement results have confirmed the high capabilities of Fe_3O_4-NPs to absorb the energy transported by an applied MF, also in the case of biocompatible solvents like water.

Accordingly, from the above analysis it is came out that, unlike AuNPs used in [5], Fe_3O_4-NPs are able to dissipate an amount of energy sufficient to activate the function of most of biological macromolecules (including the DNA molecule used in [5]) at more biologically tolerable frequencies and MF amplitudes. As a result, Fe_3O_4-NPs could be fruitfully used to remotely control BNMs, by exploiting the interaction mechanism proposed in [5]. However, even exploiting this type of NPs, the thermal mechanism proposed in [5] remains unable to induce the observed phenomenon. In fact, as shown in [76], the heat dissipation by nanometer size objects is so efficient to produce a negligible heating outside the object. Moreover, it must be excluded also a direct heat transfer from the NP to bio-molecule, via linker, or a global hating of the bio-molecule, since the relaxation times by which the DNA dissipates the thermal energy in the solvent are too short [76] to allow a storage of energy large enough to dehybridize the DNA. Accordingly, from the above analysis, it has been concluded that to concretely realize remotely controlled BNMs, by means of RF EMFs, other interaction mechanisms, different from the one proposed in [5], must be exploited.

The future research in this field will concern with the identification of the mechanisms of interaction EMF-BNMs which can be successfully exploited to remotely control BNMs, by means of EMFs

Concerning the application hyperthermia, by exploiting a thermal-electromagnetic approach and the theoretical models available in literature on the magnetic losses of MNPs dispersed in liquids, it has been developed a criterion that allows to identify the MNP-size, amplitude and frequency of the applied MF minimizing the therapeutic dose of magnetite NPs to be administered in MFH to have the therapeutic temperature rise in the tumour, with a fixed degree of heating selectivity.

By applying the criterion to a tumour of spherical shape, with a radius of 2cm, it has been founded that the amount of magnetite require to elevate the temperature of the tumour above 42 °C is lesser than 1mg per cubic centimetre of tumour. An amount about 10-15 times smaller than those usually used in literature to heat tumour of comparable dimension in animals.

This results confirm the possibility to significantly improve MFH by choosing properly NP and MF parameters.

Concerning the future research in this area, one of the most ambitious goals is to make biocompatible MNP, like cobalt or Nickel NPs, which are more efficient than Fe_3O_4-NPs, but toxics for the human organism.

Appendix A

Derivation of the expression for P_D

In this Appendix it is provided the mathematical derivation of the expression for P_D presented in Chapter 2. For the basics, let us refer to the definitions introduced in Chapter 2

A.1 Spherical waves expansion of a radiation field

In this section one provides some results useful in the following to derive the expression for $P_{s,}$

Let us be $\psi(\mathbf{r})$ a scalar function that satisfies the homogeneous Helmholtz equation and obeys to the Sommerfeld radiation condition. Then, it can be proved that the vector function defined as:

$$\mathbf{A}(\mathbf{r}) = \vec{\nabla} \times (\mathbf{r}\psi(\mathbf{r})) \tag{A.1}$$

satisfies the homogeneous Helmholtz equation and obeys to the radiation condition [24]. As a consequence, the pairs of vectors:

$$\begin{aligned} \mathbf{E}(\mathbf{r}) &= \frac{1}{k}\vec{\nabla} \times \vec{\nabla} \times (\mathbf{r}\psi(\mathbf{r})) \\ \mathbf{H}(\mathbf{r}) &= \frac{j}{\zeta}\vec{\nabla} \times (\mathbf{r}\psi(\mathbf{r})) \end{aligned} \tag{A.2}$$

and:

$$\begin{aligned} \mathbf{E}(\mathbf{r}) &= -j\zeta\vec{\nabla} \times (\mathbf{r}\psi(\mathbf{r})) \\ \mathbf{H}(\mathbf{r}) &= \frac{1}{k}\vec{\nabla} \times \vec{\nabla} \times (\mathbf{r}\psi(\mathbf{r})) \end{aligned} \tag{A.3}$$

are solution of homogeneous Maxwell's equations.

In spherical coordinates (r,ϑ,ϕ), the factorized solutions of the homogeneous, scalar, Helmholtz equation, that satisfy the Sommerfeld radiation condition, have the form [24]:

$$u_{nm}(r,\vartheta,\phi) = h_n^{(2)}(kr)\sin m\phi P_n^m(\cos\vartheta) \tag{A.4}$$

$$w_{nm}(r,\vartheta,\phi) = h_n^{(2)}(kr)\cos m\phi P_n^m(\cos\vartheta) \tag{A.5}$$

where n, m are integer numbers and $h_n^{(2)}(kr)$ and $P_n^m(\cos\vartheta)$ are the spherical Hankel functions of the second kind and the associated Legendre functions of the first kind, respectively [80]. Accordingly, the vector fields obtained by substituting in eqs. (A.2) and (A.3) the function $\psi(\mathbf{r})$ with the functions $u_{nm}(r,\vartheta,\phi)$ and $w_{nm}(r,\vartheta,\phi)$ are solutions of homogeneous Maxwell's equations. These particular EMFs are referred to as *spherical E and H waves*. In particular, the fields derived by applying eq. (A.2) to eqs. (A.4) and (A.5) represent the *odd spherical E waves* and the *even spherical E waves* and are denoted with $(\mathbf{E}_{\mathbf{nm}}^{\mathbf{eo}},\mathbf{H}_{\mathbf{nm}}^{\mathbf{eo}})$ and $(\mathbf{E}_{\mathbf{nm}}^{\mathbf{ee}},\mathbf{H}_{\mathbf{nm}}^{\mathbf{ee}})$, respectively. The fields obtained by applying eq. (A.3) to eqs. (A.4) and (A.5) are the *odd spherical H waves* and the *even spherical H waves* and are indicated with $(\mathbf{E}_{\mathbf{nm}}^{\mathbf{eo}},\mathbf{H}_{\mathbf{nm}}^{\mathbf{eo}})$ and $(\mathbf{E}_{\mathbf{nm}}^{\mathbf{ee}},\mathbf{H}_{\mathbf{nm}}^{\mathbf{ee}})$, respectively.

The components of $(\mathbf{E}_{\mathbf{nm}}^{\mathbf{eo}},\mathbf{H}_{\mathbf{nm}}^{\mathbf{eo}})$ in spherical coordinates are given by [24]:

$$\begin{aligned}
\left(E_{n,m}^{eo}\right)_r &= \frac{n(n+1)}{kr}h_n^{(2)}(kr)\sin m\phi P_n^m(\cos\vartheta)\\
\left(E_{n,m}^{eo}\right)_\vartheta &= \frac{1}{kr}\frac{\partial}{\partial r}\left(rh_n^{(2)}(kr)\right)\sin m\phi\frac{\partial}{\partial\vartheta}\left(P_n^m(\cos\vartheta)\right)\\
\left(E_{n,m}^{eo}\right)_\phi &= \frac{m}{kr\sin\vartheta}\frac{\partial}{\partial r}\left(rh_n^{(2)}(kr)\right)\cos m\phi P_n^m(\cos\vartheta)\\
\left(H_{n,m}^{eo}\right)_\vartheta &= \frac{jm}{\zeta\sin\vartheta}h_n^{(2)}(kr)\cos m\phi P_n^m(\cos\vartheta)\\
\left(H_{n,m}^{eo}\right)_\phi &= -\frac{j}{\zeta}h_n^{(2)}(kr)\sin m\phi\frac{\partial}{\partial\vartheta}\left(P_n^m(\cos\vartheta)\right)
\end{aligned} \tag{A.6}$$

whereas, the components of $(\mathbf{E}_{\mathbf{nm}}^{\mathbf{ho}},\mathbf{H}_{\mathbf{nm}}^{\mathbf{ho}})$ in spherical coordinates are given by [24]:

$$
\begin{aligned}
\left(E_{n,m}^{ho}\right)_{\vartheta} &= -\frac{j\zeta m}{\sin\vartheta} h_n^{(2)}(kr)\cos m\phi P_n^m(\cos\vartheta) \\
\left(E_{n,m}^{ho}\right)_{\phi} &= j\zeta h_n^{(2)}(kr)\sin m\phi \frac{\partial}{\partial\vartheta}\left(P_n^m(\cos\vartheta)\right) \\
\left(H_{n,m}^{ho}\right)_{r} &= \frac{n(n+1)}{kr} h_n^{(2)}(kr)\sin m\phi P_n^m(\cos\vartheta) \\
\left(H_{n,m}^{ho}\right)_{\vartheta} &= \frac{1}{kr}\frac{\partial}{\partial r}\left(rh_n^{(2)}(kr)\right)\sin m\phi \frac{\partial}{\partial\vartheta}\left(P_n^m(\cos\vartheta)\right) \\
\left(H_{n,m}^{ho}\right)_{\phi} &= \frac{m}{kr\sin\vartheta}\frac{\partial}{\partial r}\left(rh_n^{(2)}(kr)\right)\cos m\phi P_n^m(\cos\vartheta)
\end{aligned}
\tag{A.7}
$$

Concerning the expressions of $\left(\mathbf{E}_{\mathbf{nm}}^{\mathbf{ee}}, \mathbf{H}_{\mathbf{nm}}^{\mathbf{ee}}\right)$ and $\left(\mathbf{E}_{\mathbf{nm}}^{\mathbf{he}}, \mathbf{H}_{\mathbf{nm}}^{\mathbf{he}}\right)$, they can be obtained from eqs. (A.6) and (A.7) by replacing $\sin m\phi$ with $\cos m\phi$ and $\cos m\phi$ with $-\sin m\phi$, respectively [24].

The spherical E and H waves are of interest because they are a complete set of orthogonal vector functions for the EMF in a source-free region between two concentric spherical surfaces [81]. In other words, every EMF, outside a sphere containing all the sources, **J**, can be written as:

$$
\begin{aligned}
\mathbf{E} &= \sum_{n=1}^{\infty}\sum_{m=0}^{n} A_{nm}\mathbf{E}_{\mathbf{nm}}^{\mathbf{eo}} + B_{nm}\mathbf{E}_{\mathbf{nm}}^{\mathbf{ee}} + C_{nm}\mathbf{E}_{\mathbf{nm}}^{\mathbf{ho}} + D_{nm}\mathbf{E}_{\mathbf{nm}}^{\mathbf{he}} \\
\mathbf{H} &= \sum_{n=1}^{\infty}\sum^{n} A_{nm}\mathbf{H}_{\mathbf{nm}}^{\mathbf{eo}} + B_{nm}\mathbf{H}_{\mathbf{nm}}^{\mathbf{ee}} + C_{nm}\mathbf{H}_{\mathbf{nm}}^{\mathbf{ho}} + D_{nm}\mathbf{H}_{\mathbf{nm}}^{\mathbf{he}}
\end{aligned}
\tag{A.8}
$$

where [24]:

$$
\begin{aligned}
A_{nm} = \frac{-jk^2}{4\pi\varepsilon}\frac{(2n+1)}{n(n+1)}\frac{(n-m)!}{(n+m)!}(2-\delta_m)\times \\
\left(\frac{1}{j\omega}\iiint_V \mathbf{J}(\mathbf{r})\cdot\vec{\nabla}\times\vec{\nabla}\times\left(rj_n(kr)\sin m\phi P_n^m(\cos\vartheta)\mathbf{i}_{\mathbf{r}}\right)\mathrm{d}V\right)
\end{aligned}
\tag{A.9a}
$$

$$
\begin{aligned}
B_{nm} = \frac{-jk^2}{4\pi\varepsilon}\frac{(2n+1)}{n(n+1)}\frac{(n-m)!}{(n+m)!}(2-\delta_m)\times \\
\left(\frac{1}{j\omega}\iiint_V \mathbf{J}(\mathbf{r})\cdot\vec{\nabla}\times\vec{\nabla}\times\left(rj_n(kr)cos m\phi P_n^m(\cos\vartheta)\mathbf{i}_{\mathbf{r}}\right)\mathrm{d}V\right)
\end{aligned}
\tag{A.9b}
$$

$$C_{nm} = \frac{-jk^2}{4\pi}\frac{(2n+1)}{n(n+1)}\frac{(n-m)!}{(n+m)!}(2-\delta_m)\times \iiint_V \mathbf{r}\times\mathbf{J}(\mathbf{r})\cdot\vec{\nabla}\left(j_n(kr)\sin m\phi P_n^m(\cos\vartheta)\right)\mathrm{d}V \tag{A.9c}$$

$$D_{nm} = \frac{-jk^2}{4\pi}\frac{(2n+1)}{n(n+1)}\frac{(n-m)!}{(n+m)!}(2-\delta_m)\times \iiint_V \mathbf{r}\times\mathbf{J}(\mathbf{r})\cdot\vec{\nabla}\left(j_n(kr)cosm\phi P_n^m(\cos\vartheta)\right)\mathrm{d}V \tag{A.9d}$$

(In eqs. (A.9), $\delta_m = 1$ for $m = 0$ and 0 for $m \neq 0$ and $j_n(kr)$ is the spherical Bessel function of order n [80]).

Eqs (A.8) represent the *expansion in spherical waves* of the field radiated (**E**, **H**).

Moreover, due to orthogonality of the spherical waves of different kind (E or H) and order, the power radiated by (**E**, **H**) is the sum of the power radiated by each spherical wave of its expansion. In particular, from eqs. (A.6) and (A.7) it results:

$$P_{nm}^{eo} = \frac{1}{2}\oiint_S \mathbf{E}_{\mathbf{nm}}^{\mathbf{eo}}\times\mathbf{H}_{\mathbf{nm}}^{\mathbf{eo*}}\cdot\mathbf{i}_{\mathbf{r}}\mathrm{d}S = \frac{j\pi}{\zeta^*}r^2\left(h_n^{(2)}(kr)\right)^*\left(\frac{1}{kr}\frac{\partial}{\partial r}\left(rh_n^{(2)}(kr)\right)\right)\frac{n(n+1)}{(2n+1)}\frac{(n+m)!}{(n-m)!}(1-\delta_m) \tag{A.10a}$$

$$P_{nm}^{ee} = \frac{1}{2}\oiint_S \mathbf{E}_{\mathbf{nm}}^{\mathbf{ee}}\times\mathbf{H}_{\mathbf{nm}}^{\mathbf{ee*}}\cdot\mathbf{i}_{\mathbf{r}}\mathrm{d}S = \frac{j\pi}{\zeta^*}r^2\left(h_n^{(2)}(kr)\right)^*\left(\frac{1}{kr}\frac{\partial}{\partial r}\left(rh_n^{(2)}(kr)\right)\right)\frac{n(n+1)}{(2n+1)}\frac{(n+m)!}{(n-m)!}(1+\delta_m) \tag{A.10b}$$

$$P_{nm}^{ho} = \frac{1}{2}\oiint_S \mathbf{E}_{\mathbf{nm}}^{\mathbf{ho}}\times\mathbf{H}_{\mathbf{nm}}^{\mathbf{ho*}}\cdot\mathbf{i}_{\mathbf{r}}\mathrm{d}S = -j\zeta\pi r^2 h_n^{(2)}(kr)\left(\frac{1}{k^*r}\frac{\partial}{\partial r}\left(rh_n^{(2)}(kr)\right)^*\right)\frac{n(n+1)}{(2n+1)}\frac{(n+m)!}{(n-m)!}(1-\delta_m) \tag{A.10c}$$

$$P_{nm}^{he} = \frac{1}{2}\oiint_S \mathbf{E}_{\mathbf{nm}}^{\mathbf{he}} \times \mathbf{H}_{\mathbf{nm}}^{\mathbf{he}*} \cdot \mathbf{i}_{\mathbf{r}} \mathrm{d}S = \\ -j\zeta\pi r^2 h_n^{(2)}(kr)\left(\frac{1}{k^* r}\frac{\partial}{\partial r}\left(rh_n^{(2)}(kr)\right)^*\right)\frac{n(n+1)}{(2n+1)}\frac{(n+m)!}{(n-m)!}(1+\delta_m) \tag{A.10d}$$

where "*" denotes the complex conjugation.

As a concluding remark, let us note that the spherical H waves of order *n, m* can be achieved from the spherical H waves of the same order, and viceversa, by applying a duality transformation. Accordingly, EMFs radiated by two dual sources have dual expansions in spherical waves. i.e. the expansion of the first EMFs can be obtained from the expansion of the second one, and viceversa, by changing the spherical H waves of order *n, m* in spherical E waves of same order, and viceversa.

A.2 Multipole expansion of a radiation field

Let us assume that in a bounded volume, V', there is an arbitrary currents density distribution, **J**. Then, the Lorentz vector potential of the EMF radiated by **J** is given by [81]:

$$\mathbf{A}(\mathbf{r}) = \frac{\mu}{4\pi}\iiint_{V'} \mathbf{J}(\mathbf{r}')\frac{\mathrm{e}^{-jk|\mathbf{r}-\mathbf{r}'|}}{|\mathbf{r}-\mathbf{r}'|}\mathrm{d}V' \tag{A.11}$$

In eq. (A.11) by expanding the Green's function in Taylor series, i.e. [81]:

$$\frac{\mathrm{e}^{-jk|\mathbf{r}-\mathbf{r}'|}}{|\mathbf{r}-\mathbf{r}'|} = \sum_n^{\infty}\frac{1}{n!}\left(-\mathbf{r}'\cdot\vec{\nabla}\right)^n\frac{\mathrm{e}^{-jkr}}{r} \qquad (\mathbf{r} \notin V') \tag{A.12}$$

and integrating by series, one obtains:

$$\mathbf{A}(\mathbf{r}) = \mu\frac{\mathrm{e}^{-jkr}}{4\pi r}\iiint_{V'}\mathbf{J}(\mathbf{r}')\mathrm{d}V' - \mu\left(\iiint_{V'}\mathbf{J}(\mathbf{r}')\mathbf{r}\mathrm{d}V'\right)\cdot\vec{\nabla}\left(\frac{\mathrm{e}^{-jkr}}{4\pi r}\right) + \bullet\bullet\bullet \tag{A.13}$$

By exploiting the conservation of the charge, it results [81]:

$$\iiint_{V'}\mathbf{J}(\mathbf{r}')\mathrm{d}V' = j\omega\mathbf{p} \tag{A.14}$$

$$\iiint_{V'} \mathbf{r}'\mathbf{J}(\mathbf{r}')\,\mathrm{d}V' = \frac{j\omega}{2}\underline{\underline{\mathbf{Q}}} - \underline{\underline{\mathbf{M}}} \tag{A.15}$$

where **p** is the electric dipole moment, $\underline{\underline{\mathbf{M}}}$ is the magnetic dipole moment **m** expressed in dyadic form and $\underline{\underline{\mathbf{Q}}}$ is the quadrupole moment of **J**, respectively. By replacing eqs. (A.14) and (A. 3.5) in eq. (A.13) one has:

$$\mathbf{A}(\mathbf{r}) = j\omega\mu\frac{\mathrm{e}^{-jkr}}{4\pi r}\mathbf{p} - \frac{j\omega\mu}{2}\underline{\underline{\mathbf{Q}}}\cdot\vec{\nabla}\left(\frac{\mathrm{e}^{-jkr}}{4\pi r}\right) - \mu\underline{\underline{\mathbf{M}}}\cdot\vec{\nabla}\left(\frac{\mathrm{e}^{-jkr}}{4\pi r}\right) + \text{ higher order multipoles} \tag{A.16}$$

Eq. (A.16) represents the expansion of the Lorentz vector potential **A** in terms of multipoles moments of the source **J**. The corresponding expansion for the EMF radiated by **J** is obtained by applying the well known relationship relating **A** to the EMF.

According to eq. (A.16), outside V', the Lorentz vector potential **A** produced by **J,** and so the EMF, can be described as a superposition of the vector potentials produced by an elementary electric dipole, an elementary magnetic dipole, an elementary electric quadrupole and so forth, located at the origin of the fixed reference system.

In conclusion, it is worth noting that to evaluate the EMF radiated by **J** one should consider all the multipole moments of **J**. However, as far as the size of V' is small compared with the wavelength, λ, and the only radiative component of the EMF is of interest, the EMF can be estimated by retaining only the lowest order terms of the expansion (A.16). This can be easily proved by considering the expansions (A.12) and (A.13) for kr goes to infinity:

$$\frac{\mathrm{e}^{-jk|\mathbf{r}-\mathbf{r}'|}}{|\mathbf{r}-\mathbf{r}'|} = \sum_{n}^{\infty}\frac{1}{n!}\left(jk\mathbf{r}'\cdot\mathbf{i}_{\mathrm{r}}\right)^{n}\frac{\mathrm{e}^{-jkr}}{r} \qquad (kr\to\infty) \tag{A.17}$$

$$\mathbf{A}(\mathbf{r}) = \frac{\mu}{4\pi}\frac{\mathrm{e}^{-jkr}}{r}\sum_{n=1}^{\infty}\frac{j^{n}}{n!}\iiint_{V'}\mathbf{J}(\mathbf{r}')\left(k\mathbf{r}'\cdot\mathbf{i}_{\mathrm{r}}\right)^{n}\mathrm{d}V' \quad (kr\to\infty) \tag{A.18}$$

As can be seen from eq. (A.18), when the size of V' is much smaller than λ, i.e. $kr' << 1$ for every $r'\in V'$, the amplitude of the n-th term of the expansion decreases rapidly with n. As a result, one can evaluate the far field, by retaining only the first terms of the expansion (A.18). Obviously, smaller the size of the source smaller the number of multipole to be retained.

A.3 Expression of P_t in absence of losses in the background medium

Let us denote with $\mathbf{J_s}$ an equivalent macroscopic currents density distribution, with support V contained in S, whose radiating EMF on S coincides with the one scattered by the BNM, i.e. ($\mathbf{E_s}$, $\mathbf{H_s}$). By applying the divergence theorem and exploiting the Maxwell's equations, the P_t contribution in eq. (2.1) can be written as:

$$P_{\mathrm{t}} = \Re\mathrm{e}\left\{\frac{1}{2}\iiint_V \mathbf{E}_{\mathbf{i}}(\mathbf{r})\cdot\mathbf{J}_{\mathbf{s}}^{*}(\mathbf{r})\,\mathrm{d}V\right\} = \Re\mathrm{e}\left\{\frac{1}{2}\sum_{h=1}^{3}\iiint_V E_{ih}(x_1,x_2,x_3)J_{sh}^{*}(x_1,x_2,x_3)\,\mathrm{d}V\right\} \tag{A.19}$$

where J_{sh} and E_{ih} denote the components of $\mathbf{J_s}$ and $\mathbf{E_i}$ along the x_h-direction, respectively. Since $\mathbf{J_s}$ can be assumed as regular function in V and $\mathbf{E_i}$ is an analytical function in V [82], in eq. (A.19) one can replace $E_{ih}(x_1, x_2, x_3)$ with its MacLaurin series expansion and to integrate by series.

As far as $R << \lambda$, only the lowest order terms are significantly different from zero. In particular, the terms to be taken in account should provide a result in agreement with the dipolar and quadrupolar approximation of ($\mathbf{E_s}$, $\mathbf{H_s}$) on S. Accordingly, only the zero and first order terms should be retained, corresponding to the electric dipole, magnetic dipole and electric quadrupole moments of $\mathbf{J_s}$ [81].

From the above considerations, one gets:

$$P_t \cong \Re\mathrm{e}\left\{\frac{1}{2}\sum_{h=1}^{3}E_{ih}(\mathbf{0})\iiint_V J_{sh}^{*}(\mathbf{r})\,\mathrm{d}V\right\} + \Re\mathrm{e}\left\{\frac{1}{2}\sum_{h=1}^{3}\left(\vec{\nabla}E_{ih}(\mathbf{0})\right)\cdot\iiint_V\left(\mathbf{r}J_{sh}^{*}(\mathbf{r})\right)\mathrm{d}V\right\} \tag{A.20}$$

Moreover, by exploiting eqs. (A.14) and (A.15) one obtains:

$$P_{\mathrm{t}} \cong \Re\mathrm{e}\left\{-\frac{j\omega}{2}\mathbf{E_{i0}}\cdot\mathbf{p}^{*}\right\} + \Re\mathrm{e}\left\{-\frac{1}{2}\sum_{h=1}^{3}\left(\vec{\nabla}E_{ih}(\mathbf{0})\right)\cdot\left(\underline{\underline{\mathbf{M}}}^{*}\cdot\mathbf{i_h}\right)\right\} + \Re\mathrm{e}\left\{-\frac{j\omega}{4}\sum_{h=1}^{3}\left(\vec{\nabla}E_{ih}(\mathbf{0})\right)\cdot\left(\underline{\underline{\mathbf{Q}}}^{*}\cdot\mathbf{i_h}\right)\right\} \tag{A.21}$$

where $\mathbf{E_{i0}} = \mathbf{E_i}(\mathbf{0})$ represents the Electric Field (EF) in the origin and $\mathbf{i_h}$ is the unit vector along the x_h direction of the fixed reference system (h = 1, 2, 3).

Concerning the magnetic dipole term in eq. (A.21), by exploiting the relationship between the elements, M_{nh}, (n, h = 1, 2, 3) of $\underline{\underline{\mathbf{M}}}$ and the Cartesian components of $\mathbf{m}$:

$$\begin{aligned} M_{hh} &= 0 \qquad \text{per } h=1, 2, 3 \\ M_{32} &= -M_{23} = \mathbf{m} \cdot \mathbf{i_1} = m_1 \\ M_{13} &= -M_{31} = \mathbf{m} \cdot \mathbf{i_2} = m_2 \\ M_{21} &= -M_{12} = \mathbf{m} \cdot \mathbf{i_3} = m_3 \end{aligned} \tag{A.22}$$

one has:

$$\begin{aligned} &\Re\mathrm{e}\left\{-\frac{1}{2}\sum_{h=1}^{3}\left(\vec{\nabla}E_{ih}(\mathbf{0})\right)\cdot\left(\underline{\underline{\mathbf{M}}}^{*}\cdot\mathbf{i_h}\right)\right\} = \\ &\Re\mathrm{e}\left\{-\frac{1}{2}\sum_{n=1}^{3}\sum_{\substack{h=1\\(h\neq n)}}^{3}\frac{\partial E_{ih}}{\partial x_n}M_{nh}^{*}\right\} = \Re\mathrm{e}\left\{\frac{1}{2}\left(\vec{\nabla}\times\mathbf{E_i}(\mathbf{0})\right)\cdot\mathbf{m}^{*}\right\} = \Re\mathrm{e}\left\{\frac{j\omega\mu}{2}\mathbf{H_{i0}^{*}}\cdot\mathbf{m}\right\} \end{aligned} \tag{A.23}$$

where $\mathbf{H_{i0}} = \mathbf{H_i}(\mathbf{0})$ represents the MF in the origin.
From eqs. (A.21) and (A.23), P_t assumes the following form:

$$P_t = \Re\mathrm{e}\left\{\frac{j\omega}{2}\mathbf{E_{i0}^{*}}\cdot\mathbf{p}\right\} + \Re\mathrm{e}\left\{\frac{j\omega\mu}{2}\mathbf{H_{i0}^{*}}\cdot\mathbf{m}\right\} + \Re\mathrm{e}\left\{\frac{j\omega}{4}\sum_{h=1}^{3}\left(\vec{\nabla}E_{ih}^{*}(\mathbf{0})\right)\cdot\left(\underline{\underline{\mathbf{Q}}}\cdot\mathbf{i_h}\right)\right\} \tag{A.24}$$

As a concluding remark, it is provided a briefly justification of the eq. (2.5), between the quadrupolar moment and the impinging EMF, exploited in Sec. 2.1.

As discussed in Sec. 2.1, if linearity and isotropy are assumed one can put: $\mathbf{m} = \alpha_m \mathbf{H_{i0}}$. Such expression in term of $\underline{\underline{\mathbf{M}}}$ becomes:

$$\underline{\underline{\mathbf{M}}} = -j\frac{2}{\omega\mu}\alpha_m\left(\vec{\partial}\mathbf{E_{i0}}\right)^{A} \tag{A.25}$$

where $(\partial\mathbf{E_{i0}})^{A}$ is the anti-symmetric part of the matrix $\partial\mathbf{E_{i0}}$, whose h-th column is the gradient of E_{ih}, calculated at the origin O. According to eq (A.25), the anti-symmetric part of the matrix defined in eq. (A.15) depends only on the anti-symmetric of $\partial\mathbf{E_{i0}}$. As a result, for the symmetric part of the matrix defined in eq. (A.15), i.e. the quadrupolar moment, it is expected that:

$$\frac{j\omega}{2}\underline{\underline{\mathbf{Q}}} = j\frac{2}{\omega\mu}\alpha_Q\left(\partial\mathbf{E}_{\mathbf{i0}}\right)^S \tag{A.26}$$

where α_Q is a complex quantity depending only on the properties of BNM and $(\partial\mathbf{E}_{\mathbf{i0}})^S$ is the symmetric part of the matrix $\partial\mathbf{E}_{\mathbf{i0}}$.

A.4 Expression of P_s in absence of losses in the background medium

A discussed in Sec. 2.1, since $a << \lambda$ and BM is lossless, ($\mathbf{E_s}$, $\mathbf{H_s}$) can be assumed on S as the superposition of the EMFs radiated by an elementary electric dipole with moment **p**, an elementary magnetic dipole with moment **m**, and an electric quadrupole with moment $\underline{\underline{\mathbf{Q}}}$, located at the origin of the fixed reference system. Therefore, in order to evaluate P_s, one firstly has to derive the expression of the EMF radiated by such elementary sources.

From eq. (A.16), the EMF radiated by an elementary electric dipole is:

$$\mathbf{H}_{\mathbf{p}}\left(\mathbf{r}\right) = \frac{j\omega}{4\pi}\vec{\nabla}\times\frac{\mathrm{e}^{-jkr}}{r}\mathbf{p} \tag{A.27}$$

$$\mathbf{E}_{\mathbf{p}}\left(\mathbf{r}\right) = \frac{1}{j\omega\varepsilon}\vec{\nabla}\times\mathbf{H}_{\mathbf{p}}\left(\mathbf{r}\right) = \frac{1}{4\pi\varepsilon}\vec{\nabla}\times\vec{\nabla}\times\frac{\mathrm{e}^{-jkr}}{r}\mathbf{p} \tag{A.28}$$

By developing ($\mathbf{E_p}$, $\mathbf{H_p}$) in eqs. (A.27) and (A.28) in spherical components and comparing them with eqs. (A.6) and (A.7) one obtains the following expansion in spherical waves for ($\mathbf{E_p}$, $\mathbf{H_p}$):

$$\begin{aligned}\mathbf{E}_{\mathbf{p}} &= \frac{-jk^3}{4\pi\varepsilon}\left(p_1\mathbf{E}_{\mathbf{11}}^{\mathbf{ee}} + p_2\mathbf{E}_{\mathbf{11}}^{\mathbf{eo}} + p_3\mathbf{E}_{\mathbf{10}}^{\mathbf{ee}}\right)\\ \mathbf{H}_{\mathbf{p}} &= \frac{-jk^3}{4\pi\varepsilon}\left(p_1\mathbf{H}_{\mathbf{11}}^{\mathbf{ee}} + p_2\mathbf{H}_{\mathbf{11}}^{\mathbf{eo}} + p_3\mathbf{H}_{\mathbf{10}}^{\mathbf{ee}}\right)\end{aligned} \tag{A.29}$$

where p_1, p_2 and p_3 are the Cartesian component of **p**.

Concerning the EMF, ($\mathbf{E_m}$, $\mathbf{H_m}$), radiated by an elementary magnetic dipole, since **m** is the dual magnetic source of **p**, its expansion in spherical waves can be obtained from eq. (A.29) by replacing p_i/ε with m_i and changing the spherical E waves in spherical H waves. Thus:

$$\begin{aligned}\mathbf{E}_{\mathbf{m}} &= \frac{-jk^3}{4\pi}\left(m_1\mathbf{E}_{\mathbf{11}}^{\mathbf{he}} + m_2\mathbf{E}_{\mathbf{11}}^{\mathbf{ho}} + m_3\mathbf{E}_{\mathbf{10}}^{\mathbf{he}}\right)\\ \mathbf{H}_{\mathbf{m}} &= \frac{-jk^3}{4\pi}\left(m_1\mathbf{H}_{\mathbf{11}}^{\mathbf{he}} + m_2\mathbf{H}_{\mathbf{11}}^{\mathbf{ho}} + m_3\mathbf{H}_{\mathbf{10}}^{\mathbf{he}}\right)\end{aligned} \tag{A.30}$$

Finally, from eq. (A.16), the EMF radiated by an elementary electric quadrupole, is given by:

$$\mathbf{H}_{\mathbf{Q}}(\mathbf{r}) = -\frac{j\omega}{8\pi}\vec{\nabla}\times\left(\underline{\underline{\mathbf{Q}}}\cdot\vec{\nabla}\left(\frac{\mathrm{e}^{-jkr}}{r}\right)\right) \tag{A.31}$$

$$\mathbf{E}_{\mathbf{Q}}(\mathbf{r}) = \frac{1}{j\omega\varepsilon}\vec{\nabla}\times\mathbf{H}_{\mathbf{Q}}(\mathbf{r}) = -\frac{1}{8\pi\varepsilon}\vec{\nabla}\times\vec{\nabla}\times\left(\underline{\underline{\mathbf{Q}}}\cdot\vec{\nabla}\left(\frac{\mathrm{e}^{-jkr}}{r}\right)\right) \tag{A.32}$$

Similarly, by developing ($\mathbf{E_Q}$, $\mathbf{H_Q}$) in eqs. (A.31) and (A.32) in spherical components and comparing them with eqs. (A.6) and (A.7) one attains the following expansion in spherical waves for $\mathbf{E_Q}$, $\mathbf{H_Q}$):

$$\begin{aligned}\mathbf{E}_{\mathbf{Q}} &= \frac{-jk^4}{96\pi\varepsilon}\left(2\left(2Q_{33}-Q_{22}-Q_{11}\right)\mathbf{E}_{\mathbf{20}}^{\mathbf{ee}} + \left(Q_{11}-Q_{22}\right)\mathbf{E}_{\mathbf{22}}^{\mathbf{ee}} + 2Q_{12}\mathbf{E}_{\mathbf{22}}^{\mathbf{eo}} + 4Q_{23}\mathbf{E}_{\mathbf{21}}^{\mathbf{eo}} + 4Q_{31}\mathbf{E}_{\mathbf{21}}^{\mathbf{ee}}\right)\\ \mathbf{H}_{\mathbf{Q}} &= \frac{-jk^4}{96\pi\varepsilon}\left(2\left(2Q_{33}-Q_{22}-Q_{11}\right)\mathbf{H}_{\mathbf{20}}^{\mathbf{ee}} + \left(Q_{11}-Q_{22}\right)\mathbf{H}_{\mathbf{22}}^{\mathbf{ee}} + 2Q_{12}\mathbf{H}_{\mathbf{22}}^{\mathbf{eo}} + 4Q_{23}\mathbf{H}_{\mathbf{21}}^{\mathbf{eo}} + 4Q_{31}\mathbf{H}_{\mathbf{21}}^{\mathbf{ee}}\right)\end{aligned} \tag{A.33}$$

where Q_{nh}, (n, h = 1, 2, 3) is the nh-th element of $\underline{\underline{\mathbf{Q}}}$.
Now, one can derive the expression for P_s. Due to the power orthogonality of the multipoles fields, P_s is the sum of the active power radiated by each spherical wave in eqs. (A.29), (A.30) and (A.33). Therefore:

$$\begin{aligned}P_s = &-\left|\frac{k^3}{4\pi}\right|^2 \Re\mathrm{e}\left\{\left|\frac{p_1}{\varepsilon}\right|^2 P_{11}^{ee} + \left|\frac{p_2}{\varepsilon}\right|^2 P_{11}^{eo} + \left|\frac{p_3}{\varepsilon}\right|^2 P_{10}^{ee} + \right\} -\\ &\left|\frac{k^3}{4\pi}\right|^2 \Re\mathrm{e}\left\{|m_1|^2 P_{11}^{he} + |m_2|^2 P_{11}^{ho} + |m_3|^2 P_{10}^{he}\right\} -\\ &\left|\frac{k^4}{96\pi\varepsilon}\right|^2 \Re\mathrm{e}\left\{4\left|2Q_{33}-Q_{22}-Q_{11}\right|^2 P_{20}^{ee} + \left|Q_{11}-Q_{22}\right|^2 P_{22}^{ee}\right\} -\\ &\left|\frac{k^4}{96\pi\varepsilon}\right|^2 \Re\mathrm{e}\left\{4\left|Q_{12}\right|^2 P_{22}^{eo} + 16\left|Q_{23}\right|^2 P_{21}^{eo} + 16\left|Q_{31}\right|^2 P_{21}^{ee}\right\}\end{aligned} \tag{A.34}$$

where $P_{10}^{ee}, P_{11}^{ee}, P_{11}^{eo}, P_{10}^{he}, P_{11}^{he}, P_{11}^{ho}, P_{20}^{ee}, P_{21}^{ee}, P_{21}^{eo}, P_{22}^{ee}, P_{22}^{eo}$ are given in eqs (A.10). Moreover, as far as BM is lossless, as in the case considered in Sec. 2.1, P_s can be evaluated as:

$$\begin{aligned} P_s = -\lim_{kr\to\infty}\Bigg\{ & \left|\frac{k^3}{4\pi}\right|^2 \left(\left|\frac{p_1}{\varepsilon}\right|^2 P_{11}^{ee} + \left|\frac{p_2}{\varepsilon}\right|^2 P_{11}^{eo} + \left|\frac{p_3}{\varepsilon}\right|^2 P_{10}^{ee} \right) + \\ & \left|\frac{k^3}{4\pi}\right|^2 \left(|m_1|^2 P_{11}^{he} + |m_2|^2 P_{11}^{ho} + |m_3|^2 P_{10}^{he} \right) + \\ & \left|\frac{k^4}{96\pi\varepsilon}\right|^2 \left(4|2Q_{33} - Q_{22} - Q_{11}|^2 P_{20}^{ee} + |Q_{11} - Q_{22}|^2 P_{22}^{ee} \right) + \\ & \left|\frac{k^4}{96\pi\varepsilon}\right|^2 \left(4|Q_{12}|^2 P_{22}^{eo} + 16|Q_{23}|^2 P_{21}^{eo} + 16|Q_{31}|^2 P_{21}^{ee} \right) \Bigg\} \end{aligned} \tag{A.35}$$

From eqs (A.10), (A.35) and by noting that [80]:

$$\lim_{kr\to\infty} \frac{r^2}{kr}\left(h_n^{(2)}(kr)\right)^* \frac{\partial}{\partial r}\left(rh_n^{(2)}(kr)\right) = -\lim_{kr\to\infty} \frac{r^2}{kr} h_n^{(2)}(kr) \frac{\partial}{\partial r}\left(rh_n^{(2)}(kr)\right)^* = -\frac{j}{k^2} \tag{A.36}$$

one obtain the following expression for P_s when a lossless BM is involved:

$$P_s = -\frac{vk^4|\mathbf{p}|^2}{12\pi\varepsilon} - \frac{\mu v k^4 |\mathbf{m}|^2}{12\pi} - \frac{vk^6}{160\pi\varepsilon}\left(\sum_{n,h=1}^{3} |Q_{nh}|^2 - \frac{1}{3}\left| \sum_{n=1}^{3} Q_{nn} \right|^2 \right) \tag{A.37}$$

Appendix B

Expression of the polarization coefficients for a metallic sphere with radius much smaller than the wavelength

In this section are derived the expressions of the polarization coefficients α_e, α_m and α_Q (see Sec. 2.1) for a metallic sphere with radius $a << \lambda$.
Since α_e, α_m and α_Q are independent of the characteristics of the field incident on the sphere, the analysis is carried out by assuming as incident field a linearly polarized plane wave.

Let us consider a metallic sphere, of radius a, on which acts an incident plane wave, linearly polarized, ($\mathbf{E_i}$, $\mathbf{H_i}$). Chosen a Cartesian reference system, (O, x_1, x_2, x_3), centred on the sphere and such that: $\mathbf{E_i} = E_{i0} e^{-jkx_3} \mathbf{i_1}$, $\mathbf{H_i} = H_{i0} e^{-jkx_3} \mathbf{i_2}$, the expansion in spherical wave of the EMF scattered by the sphere is given by [24]:

$$\begin{aligned} \mathbf{E_s} &= E_{i0} \sum_{n=1}^{\infty} (-j)^{n+1} \frac{2n+1}{n(n+1)} \left(a_n \mathbf{E_{n1}^{ee}} + \frac{b_n}{\zeta} \mathbf{E_{n1}^{ho}} \right) \\ \mathbf{H_s} &= E_{i0} \sum_{n=1}^{\infty} (-j)^{n+1} \frac{2n+1}{n(n+1)} \left(a_n \mathbf{H_{n1}^{ee}} + \frac{b_n}{\zeta} \mathbf{H_{n1}^{ho}} \right) \end{aligned} \tag{B.1}$$

where a_n and b_n are complex quantities, depending on the electromagnetic and geometrical properties of the sphere, whose expressions are given in [24].

By comparing the coefficients of the expansion (B.1) with eqs. (A.9b) and (A.9c) one obtains the following relations for the current density distribution **J** induced on the sphere by the incident EMF:

$$\frac{1}{j\omega} \iiint_V \mathbf{J}(\mathbf{r}) \cdot \vec{\nabla} \times \vec{\nabla} \times \left(\frac{r j_n(kr)}{k} cos\phi P_n^1(\cos\vartheta) \mathbf{i_r} \right) dV = (-j)^n \frac{2\pi\varepsilon}{k^3} n(n+1) a_n E_{i0} \tag{B.2}$$

$$\iiint_V \mathbf{r}\times\mathbf{J}(\mathbf{r})\cdot\vec{\nabla}\left(\frac{j_n(kr)}{k}\sin\phi P_n^1(\cos\vartheta)\right)\mathrm{d}V = (-j)^n\frac{2\pi}{k^3}n(n+1)\frac{b_n}{\zeta}E_{i0} \tag{B.3}$$

Since $j_n(kr)$ is an analytical function, in eqs. (B.2) and (B.3) one can replace $j_n(kr)$ with its Taylor series expansion [80] and to integrate by series. Furthermore, as far as $a << \lambda$ ($ka << 1$) one can retain only the lowest order term in kr.
Thus, for a small metallic sphere the relations (B.2) and (B.3) become:

$$\frac{1}{j\omega}\iiint_V \mathbf{J}(\mathbf{r})\cdot\vec{\nabla}\times\vec{\nabla}\times\left(\frac{2^n n!}{(2n+1)!}\frac{r}{k}(kr)^n cos\phi P_n^1(\cos\vartheta)\mathbf{i}_r\right)\mathrm{d}V = (-j)^n\frac{2\pi\varepsilon}{k^3}n(n+1)a_n E_{i0} \tag{B.4}$$

$$\iiint_V \mathbf{r}\times\mathbf{J}(\mathbf{r})\cdot\vec{\nabla}\left(\frac{1}{k}\frac{2^n n!}{(2n+1)!}(kr)^n\sin\phi P_n^1(\cos\vartheta)\right)\mathrm{d}V = (-j)^n\frac{2\pi}{k^3}n(n+1)\frac{b_n}{\zeta}E_{i0} \tag{B.5}$$

As can be noted, the integral on the left side of eq. (B.4) is related to the spatial moment of order n-1 of **J**, while the integral on the left side of eq. (B.5) is related to the patial moment of order n of **J**. Accordingly, eqs. (B.4) and (B.5) allow to derive the expressions of the multipoles moments induced on a metallic sphere, of radius $a << \lambda$, by a linearly polarized wave plane.
For $n = 1$ the integral on the left hand of eq. (B.4) takes the form:

$$\frac{1}{j\omega}\iiint_V \mathbf{J}(\mathbf{r})\cdot\vec{\nabla}\times\vec{\nabla}\times\left(\frac{2^n n!}{(2n+1)!}\frac{r}{k}(kr)^n cos\phi P_n^1(\cos\vartheta)\mathbf{i}_r\right)\mathrm{d}V \underset{(n=1)}{=} \frac{4}{6}\frac{1}{j\omega}\iiint_V \mathbf{J}(\mathbf{r})\cdot\left(cos\phi\sin\vartheta\mathbf{i}_r + cos\phi\cos\vartheta\mathbf{i}_\vartheta - \sin\phi\mathbf{i}_\phi\right)\mathrm{d}V = \frac{2}{3}\mathbf{p}\cdot\mathbf{i}_1 \tag{B.6}$$

whereas, for $n = 2$ has the form:

$$\begin{aligned}
&\frac{1}{j\omega}\iiint_V \mathbf{J}(\mathbf{r})\cdot\vec{\nabla}\times\vec{\nabla}\times\left(\frac{2^n n!}{(2n+1)!}\frac{r}{k}(kr)^n\, cos\phi P_n^1(\cos\vartheta)\mathbf{i}_r\right)\mathrm{d}V \underset{(n=2)}{=} \\
&\frac{3}{5j\omega}\iiint_V \mathbf{J}(\mathbf{r})\cdot kr\cos\vartheta\left(\sin\vartheta cos\phi\,\mathbf{i}_r+\cos\vartheta cos\phi\,\mathbf{i}_\vartheta-\sin\phi\,\mathbf{i}_\phi\right)\mathrm{d}V+ \\
&\frac{3}{5j\omega}\iiint_V \mathbf{J}(\mathbf{r})\cdot kr\left(\sin\vartheta cos\phi\left(\cos\vartheta\,\mathbf{i}_r-\sin\vartheta\,\mathbf{i}_\vartheta\right)\right)\mathrm{d}V= \\
&\frac{3k}{5j\omega}\iiint_V \left(\mathbf{i}_1\cdot\mathbf{J}(\mathbf{r})\right)\left(\mathbf{r}\cdot\mathbf{i}_3\right)r+\left(\mathbf{i}_1\cdot\mathbf{r}\right)\left(\mathbf{J}(\mathbf{r})\cdot\mathbf{i}_3\right)\mathrm{d}V=\frac{3k}{5}\mathbf{i}_1\cdot\underline{\underline{\mathbf{Q}}}\cdot\mathbf{i}_3
\end{aligned} \tag{B.7}$$

Finally, for $n = 1$, the integral on the left hand of eq. (B.5) takes the form:

$$\begin{aligned}
&\iiint_V \mathbf{r}\times\mathbf{J}(\mathbf{r})\cdot\vec{\nabla}\left(\frac{1}{k}\frac{2^n n!}{(2n+1)!}(kr)^n\sin\phi P_n^1(\cos\vartheta)\right)\mathrm{d}V \underset{(n=1)}{=} \\
&\iiint_V \mathbf{r}\times\mathbf{J}(\mathbf{r})\cdot\frac{2}{6}\left(\sin\phi\sin\vartheta\,\mathbf{i}_r+\sin\phi\cos\vartheta\,\mathbf{i}_\vartheta+\cos\phi\right)\mathrm{d}V=\frac{2}{3}\mathbf{m}\cdot\mathbf{i}_2
\end{aligned} \tag{B.8}$$

By substituting in eqs. (B.4) and (B.5) one obtains the following expressions for the multipole moments **p**, **m** and $\underline{\underline{\mathbf{Q}}}$ induced on a small metallic sphere, immersed in a linearly polarized plane wave:

$$\mathbf{p}\cdot\mathbf{i}_1=-j\frac{6\pi\varepsilon}{k^3}a_1E_{i0}=-j\frac{6\pi\varepsilon}{k^3}a_1\mathbf{E}_{\mathbf{i0}}\cdot\mathbf{i}_1 \tag{B.9}$$

$$\mathbf{m}\cdot\mathbf{i}_2=-j\frac{6\pi}{k^3}\frac{b_1}{\zeta}E_{i0}=-j\frac{6\pi}{k^3}b_nH_{i0}=-j\frac{6\pi}{k^3}b_1\mathbf{H}_{\mathbf{i0}}\cdot\mathbf{i}_2 \tag{B.10}$$

$$\begin{aligned}
&\mathbf{i}_1\cdot\underline{\underline{\mathbf{Q}}}\cdot\mathbf{i}_3=-j\frac{40\pi\varepsilon}{k^5}a_2\left(-\frac{jk}{2}E_{i0}\right)= \\
&-j\frac{40\pi\varepsilon}{k^5}a_2\left(\frac{1}{2}\frac{\partial E_{i3}}{\partial x_1}+\frac{1}{2}\frac{\partial E_{i1}}{\partial x_3}\right)=-j\frac{40\pi\varepsilon}{k^5}a_2\mathbf{i}_1\cdot\left(\vec{\partial}\mathbf{E}_\mathbf{i}\right)_\mathbf{0}^S\cdot\mathbf{i}_3
\end{aligned} \tag{B.11}$$

By comparing eq. (B.9) with eq. (2.3), eq. (B.10) with eqs. (2.4) and eq. (B.11) with eq (2.5) one has:

$$\alpha_e=-j\frac{6\pi}{k^3}a_1 \tag{B.12}$$

$$\alpha_m = -j\frac{6\pi}{k^3}b_1 \tag{B.13}$$

$$\alpha_Q = -j\frac{10\pi}{k^3}a_2 \tag{B.14}$$

where a_1, a_2 and b_1, are given in [24]. Since a_n and b_n depend only on the electromagnetic and geometrical properties of the sphere and on the electromagnetic parameters of the BM, it follows that α_e, α_m and α_Q are independent of the characteristics of the incident field. Accordingly, as expected, the obtained result is completely general. i.e. it holds for any incident field.

For a small metallic sphere with radius much smaller than the skin depth, as in the case of AuNP used in [5], the coefficients a_1, a_2 and b_1 take the following, simple, form [24]:

$$a_1 = j\frac{2}{3}\frac{\varepsilon_D - \varepsilon}{\varepsilon_D + 2\varepsilon}(ka)^3 \tag{B.15}$$

$$b_1 = j\frac{1}{45}\frac{(\varepsilon_D - \varepsilon)}{\varepsilon}(ka)^5 \tag{B.16}$$

$$a_2 = j\frac{1}{15}\frac{\varepsilon_D - \varepsilon}{2\varepsilon_D + 3\varepsilon}(ka)^5 \tag{B.17}$$

where:

$$\varepsilon_D = \varepsilon_0\left(1 - j\frac{\sigma_D}{\omega\varepsilon_0}\right) \tag{B.18}$$

Thus, polarization coefficients become:

$$\alpha_e = 4\pi a^3\frac{\varepsilon_D - \varepsilon}{\varepsilon_D + 2\varepsilon} = 4\pi a^3\frac{\varepsilon_0\left(1 - j\frac{\sigma_D}{\omega\varepsilon_0}\right) - \varepsilon}{\varepsilon_0\left(1 - j\frac{\sigma_D}{\omega\varepsilon_0}\right) + 2\varepsilon} \tag{B.19}$$

$$\alpha_m = \frac{2\pi}{15} a^3 \frac{(\varepsilon_D - \varepsilon)}{\varepsilon} (ka)^2 = \frac{2\pi}{15} a^5 \omega^2 \varepsilon \mu \left(\frac{\varepsilon_0 - \varepsilon}{\varepsilon} - j \frac{\sigma_D}{\omega \varepsilon} \right) \tag{B.20}$$

$$\alpha_Q = \frac{2\pi}{3} a^3 \frac{\varepsilon_D - \varepsilon}{2\varepsilon_D + 3\varepsilon} (ka)^2 = \frac{2\pi}{3} a^5 \omega^2 \varepsilon \mu \frac{\varepsilon_0 \left(1 - j \frac{\sigma_D}{\omega \varepsilon_0} \right) - \varepsilon}{2\varepsilon_0 \left(1 - j \frac{\sigma_D}{\omega \varepsilon_0} \right) + 3\varepsilon} \tag{B.21}$$

As a concluding remark, it is worth noting that the expressions of the coefficients α_e, and α_Q can be further simplified by exploiting the condition $\sigma_D / \omega |\varepsilon| >> 1$, which is widely verified for metallic scatterers and frequencies up to several hundred of GHz (in [5] $\sigma_D / \omega |\varepsilon| \sim 10^6$). In particular, α_e and α_m assume the form:

$$\alpha_e \cong 4\pi a^3 \left(1 - j3 \frac{\omega \varepsilon'}{\sigma_D} \right) \tag{B.22}$$

$$\alpha_m = \frac{2\pi}{15} a^5 \omega^2 \varepsilon' \mu \left(\frac{\varepsilon_0 - \varepsilon'}{\varepsilon'} - j \frac{\sigma_D}{\omega \varepsilon'} \right) \tag{B.23}$$

where ε' represents the real part of the electric permittivity of the BM
Concerning α_Q, in the case of a lossless BM it takes the form:

$$\alpha_Q = \frac{\pi}{3} a^5 \omega^2 \varepsilon' \mu \left(1 - j \frac{5}{2} \frac{\omega \varepsilon'}{\sigma_D} \right) \tag{B.24}$$

while in the case of BM with dielectric losses, it has the form:

$$\alpha_Q = \frac{\pi}{3} a^5 \omega^2 \mu (\varepsilon' - j\varepsilon'') \tag{B.25}$$

where ε'' is the opposite of the imaginary part of the electric permittivity of the BM

Appendix C

Electromagnetic characterization of a coil

A coil, as shown in Fig. C.1a, consists of a metallic wire wound into a helical structure and fed at the ends. The geometrical features of a coil are completely defined by providing: the pitch, p[(*)], the length of the winding, l, and the diameter of the turns, d, or equivalently the number of turns, N, the pitch angle, φ[(**)] and the number of turns per meter, n.

In the low frequency regime, i.e. when l is much smaller than the wavelength, λ, of the applied signal, the EMF inside a coil can be suitably described by a quasi-static electric model (i.e. by neglecting the displacement-current term in the Maxwell's equations). According to this model, the spatial distribution of the field inside a coil is practically uniform and the EF is negligible as compared with the MF. Accordingly, in the low frequency regime a coil is really an only MF applicators, as assumed in [5].
However, when $l \sim \lambda$, the electromagnetic behaviour of a coil cannot be described by a quasi-static model in that becomes relevant the propagation character of the EMF. Accordingly, most of the results obtained in the low frequency regime cannot be extended when l becomes comparable or lesser than λ. In particular, due to the propagation, it is expected that the EMF inside a coil is not uniform and EF is not negligible as compared with the MF.

For the 35-turns coil used in [5], by assuming d = 0.56 cm (resulting in a cross section of about 1 cm^2,) and p = 3 mm, $l \sim$ 123 cm which is about four times larger than the wavelength of the applied signal (f = 1GHz results in a free-space wavelength of about 30 cm). Accordingly, for the coil used in [5] it is expected that the produced EF is not negligible, as erroneously assumed in [5]. Since the presence of an EF can significantly contribute to the value of P_D, as shown in eq. (2.6), to correctly analyze the model

---

(*) the pitch of a coil is the spacing between two adjacent turns

(**) the pitch angle is the angle that the unit vector along the direction of the winding makes with a plane perpendicular to the axis of the coil

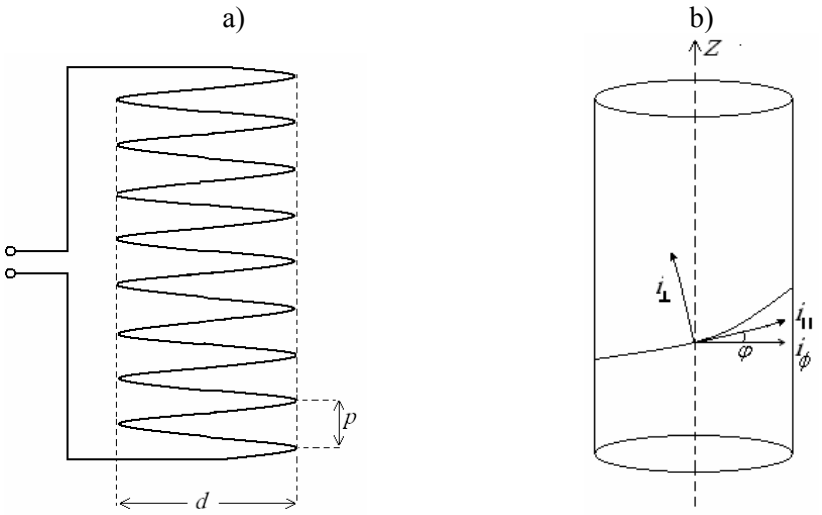

Fig. C.1. a) round wire coil; b) Sheath Helix

proposed in [5], it is important to provide an accurate electromagnetic characterization of a coil.

Concerning this point, it must be noted that the homogeneous Helmholtz equation is not separable in helical coordinates, so, a rigorous solution for the wave propagation along a coil cannot be attained. However, as far as $p << \lambda$, the electromagnetic behaviour of a coil can be suitably described by the *Sheath Helix* model [75], for which a rigorous solution for wave equation there exists.

The Sheath Helix model consists in replacing the winding with a circular tube, electrically smooth, having infinite conductivity in the direction of the winding and zero conductivity in a direction normal to the turns (see Fig. C.1b). (obviously, it is assumed the winding of perfect electric conductor).
From a mathematical viewpoint, this model is described by the following boundary conditions at the circular surface $r = d/2$ (see Fig. C.1b):

$$E^i \cdot \left(\mathbf{i}_n \times \mathbf{i}_{||}\right) = E^o \cdot \left(\mathbf{i}_n \times \mathbf{i}_{||}\right) \tag{C.1}$$

$$E^i \cdot \mathbf{i}_{||} = E^o_{||} \cdot \mathbf{i}_{||} = 0 \tag{C.2}$$

$$H^i \cdot \mathbf{i}_{||} = H^e \cdot \mathbf{i}_{||} \tag{C.3}$$

where $\mathbf{i_n}$ is the unit vectors normal to the surface $r = d/2$, $\mathbf{i_{\|}}$ is the unit vector in direction of the winding and the superscripts "*i*" ed "*o*" indicate the regions $r \le d/2$ and $r \ge d/2$, respectively.
From the cylindrical symmetry of the boundary conditions (C.1) to (C.3) follows that the EMF propagating on a Sheath Helix can be represented in terms of TE and TM modes, which are the factorized solutions, in cylindrical coordinates, of the problem consisting of the homogeneous Helmholtz equation and the boundary condition (C.1) to (C.3) [75].

Accordingly, as long as $p << \lambda$, the EMF inside (and outside) a coil can be expressed as a superposition of TE and TM modes of the Sheath Helix. Obviously, the effective number of modes to be retained depends on the value of the working frequency, *f*.

In cylindrical coordinates (r, ϕ, z), the components of the dominant TE mode, say TE_0, propagating along a Sheath Helix are given by [75]:

$$E_{\phi}^{i[o]} = -\mathrm{V}_{TE}^{i[o]}(z) I_1(\tau r)\left[K_1(\tau r)\right] \tag{C.4}$$

$$H_{r}^{i[o]} = \mathrm{I}_{TE}^{i[o]}(z) I_1(\tau r)\left[K_1(\tau r)\right] \tag{C.5}$$

$$H_{z}^{i[o]} = \frac{\tau}{j\omega\mu}\mathrm{V}_{TE}^{i[o]}(z) I_0(\tau r)\left[K_0(\tau r)\right] \tag{C.6}$$

while the components of the dominant TM mode, say TM_0, are given by [75]:

$$E_{r}^{i[o]} = \mathrm{V}_{TM}^{i[o]}(z) I_1(\tau r)\left[K_1(\tau r)\right] \tag{C.7}$$

$$E_{z}^{i[o]} = \frac{\tau}{j\omega\varepsilon}\mathrm{I}_{TM}^{i[o]}(z) I_0(\tau r)\left[K_0(\tau r)\right] \tag{C.8}$$

$$H_{\phi}^{i[o]} = \mathrm{I}_{TM}^{i[o]}(z) I_1(\tau r)\left[K_1(\tau r)\right] \tag{C.9}$$

In eqs. (C.4) to (C.9), $I_0(\tau r)$, $I_1(\tau r)$, $K_0(\tau r)$, $K_1(\tau r)$ are the modified Bessel functions of the first and second kind [80] and the functions $\mathrm{V}_{TE}^{i[o]}(z)$, $\mathrm{I}_{TE}^{i[o]}(z)$, $\mathrm{V}_{TM}^{i[o]}(z)$, $\mathrm{I}_{TM}^{i[o]}(z)$ are solutions of the following transmission line equations:

$$\frac{\partial \mathrm{V}(z)}{\partial z} = -jZ\beta \mathrm{I}(z) \tag{C.10}$$

$$\frac{\partial \mathrm{I}(z)}{\partial z} = -j\frac{\beta}{Z}\mathrm{V}(z) \tag{C.11}$$

where $\beta = \sqrt{k^2 + \tau^2}$ and $Z=\omega\mu/\beta$ for the TE_0 mode and $Z=\beta/\omega\varepsilon$ for TM_0 mode.

The functions $\mathrm{V}_{TE}^{i[o]}(z)$, $\mathrm{I}_{TE}^{i[o]}(z)$, $\mathrm{V}_{TM}^{i[o]}(z)$, $\mathrm{I}_{TM}^{i[o]}(z)$ are not independent, but related by the boundary conditions (C.1) to (C.3) as follow:

$$\mathrm{V}_{TE}^{i}(\mathrm{z}) = \frac{\tau}{j\omega\varepsilon}\mathrm{I}_{TM}^{i}(z)\frac{I_0(\tau d/2)}{I_1(\tau d/2)}\tan\varphi \tag{C.12}$$

$$\mathrm{V}_{TE}^{o}(\mathrm{z}) = -\frac{\tau}{j\omega\varepsilon}\mathrm{I}_{TM}^{o}(z)\frac{K_0(\tau d/2)}{K_1(\tau d/2)}\tan\varphi \tag{C.13}$$

$$\mathrm{I}_{TM}^{i}(z)I_0(\tau d/2) = \mathrm{I}_{TM}^{o}(z)K_0(\tau d/2) \tag{C.14}$$

From eqs. (C.12) and (C.13) follows that to satisfy the boundary condition at the surface $r = d/2$ both the TE_0 and TM_0 modes have to considered. Accordingly, in a coil the TE_0 and TM_0 modes cannot exist separately, but are coupled by the boundary conditions. Thus, all the six component of the EMF are present in a coil. From a physical point of view, the presence of E_z along the coil-axis is a consequence of the presence of a component along the z-axis of the current flowing in the winding, due to the pitch p of the coil.

In eqs. (C.4) to (C.13) the quantity τ represents the transverse eigenvalue and is solution of the following equation [75]:

$$\frac{I_1(xd/2)K_1(xd/2)}{I_0(xd/2)K_0(xd/2)} - \frac{x^2}{k^2}\tan^2\varphi = 0 \tag{C.15}$$

obtained by exploiting the boundary conditions (C.1) to (C.3).

Obviously, chosen k, d and φ, if $x = \tau$ satisfies eq. (C.15), then, τ is the only root of the eigenvalues equation. However, the existence of a τ could not be guaranteed for any value of k, d and φ. Indeed, the solution of eq. (C.15) exists for every value of k, d and φ different from zero. This can be easily

proved by noting that the function on the left side of eq. (C.15), in $(0, +\infty) \subset \mathbb{R}$, is real, continuous and assumes positive and negative values. The latter result is a consequence of the following inequalities [80]:

$$\lim_{x\to 0} \frac{I_1(xd/2)K_1(xd/2)}{I_0(xd/2)K_0(xd/2)} - \frac{x^2}{k^2}\tan^2\varphi \approx \frac{1}{2\ln(2/xd)} - \frac{x^2}{k^2}\tan^2\varphi > 0 \tag{C.16}$$

$$\lim_{x\to \infty} \frac{I_1(xd/2)K_1(xd/2)}{I_0(xd/2)K_0(xd/2)} - \frac{x^2}{k^2}\tan^2\varphi \approx 1 - \frac{x^2}{k^2}\tan^2\varphi < 0 \tag{C.17}$$

As a consequence, the modes TE_0 and TM_0 propagates along a coil at any frequency different from zero. Obviously, they represent the main contribution to the EMF at low frequencies.
The above result shows also that $\tau \in \mathbb{R}^+$, which is consistent with the existence of slow waves propagating along a coil.

From the above analysis follows that both the EF and MF are present inside a coil. In particular, for the TE_0 and TM_0 modes it results:

$$\left|\frac{E_z^i}{H_z^i}\right| = \sqrt{\frac{I_1(\tau d/2)K_0(\tau d/2)}{I_0(\tau d/2)K_1(\tau d/2)}}\zeta = \gamma\zeta \tag{C.18}$$

where ζ is the characteristic impedance of the medium filling a coil (obviously, it is assumed the medium without losses).
In eq. (C.18) the function γ is real, continuous and lower than unity. The latter property follows by the inequalities [80]:

$$I_1(x) = \frac{1}{\pi}\int_0^{\pi} e^{x\cos\vartheta}\cos\vartheta \mathrm{d}\vartheta \le \frac{1}{\pi}\int_0^{\pi} e^{x\cos\vartheta}\mathrm{d}\vartheta = I_0(x) \tag{C.19}$$

$$K_0(x) = \int_0^{+\infty} e^{-x\cosh t}\mathrm{d}t \le \int_0^{+\infty} e^{-x\cosh t}\cosh t \mathrm{d}t = K_1(x) \tag{C.20}$$

As a result, the value of $|E_z^i/H_z^i|$ in a coil, for which $p << \lambda$, ranges from zero to ζ.

For the 35-turns coil used in [5], for which the Sheath Helix model can be safely adopted, at f = 1GHz $\tau \approx 205.1$ m^{-1} and $|E_z^i/H_z^i| \approx 0.6\zeta_0 = 226\ \Omega$ (ζ_0 is the free-space characteristics impedance). This value is comparable

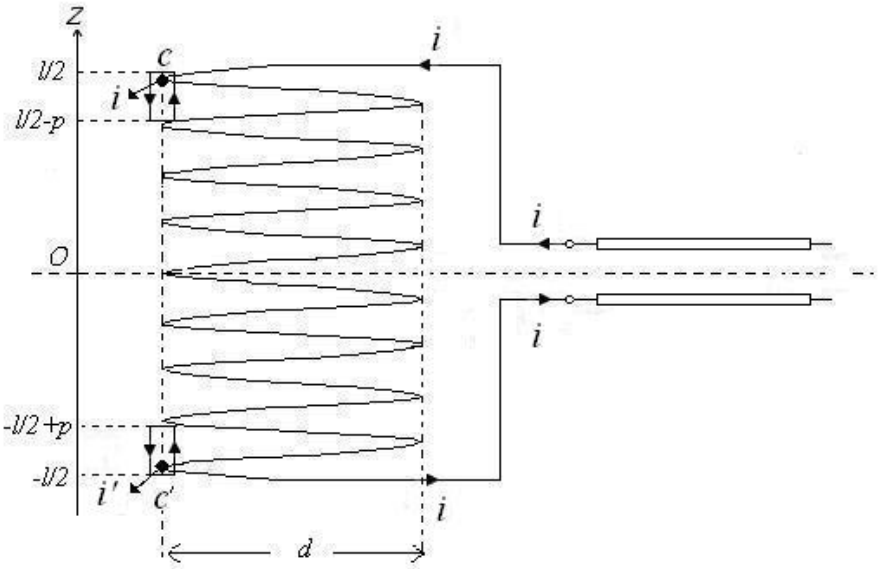

Fig. C.2. A coil fed with a transmission line

with the ratio between the amplitudes of the EF and MF in a plane wave. Therefore, the coil exploited in [5] produce an axial EF which is even more intense of the axial MF. Thus, EF must be necessarily taken in account when evaluating P_D.

In conclusion, it is worth noting that the last result has been achieved by assuming that the EMF inside the coil, at f = 1GHz, can be suitably described by the only TE_0 and TM_0 modes of the Sheath Helix. In other words, one supposes negligible the contribution due to the higher order modes compared with TE_0 and TM_0, at f = 1GHz. The consistency of such assumption has been confirmed by numerical simulations. Later on, it will provide the detail and the results of these numerical simulations.

In Fig. C.2 it is shown a schematization of the structure analyzed numerically. In particular, the winding represents the coil exploited in [5] and the transmission line schematizes the coaxial cable exploited in the simulations to feed the coil, at f = 1GHz. The feed is placed at the middle of the coil in order to make the entire structure symmetric with respect to the z-axis.

In Fig. C.3 are shown the results of the numerical simulations. In particular, in Fig. C.3a is plotted the spatial distribution inside the coil of $|E_z^i|$, while in Fig. C.3b is plotted the spatial distribution of $|H_z^i|$. As can be seen, both $|E_z^i|$ and $|H_z^i|$ display a periodic behaviour along the z-axis, which is symmetric with respect to the plane $z = 0$. Moreover, by comparing the

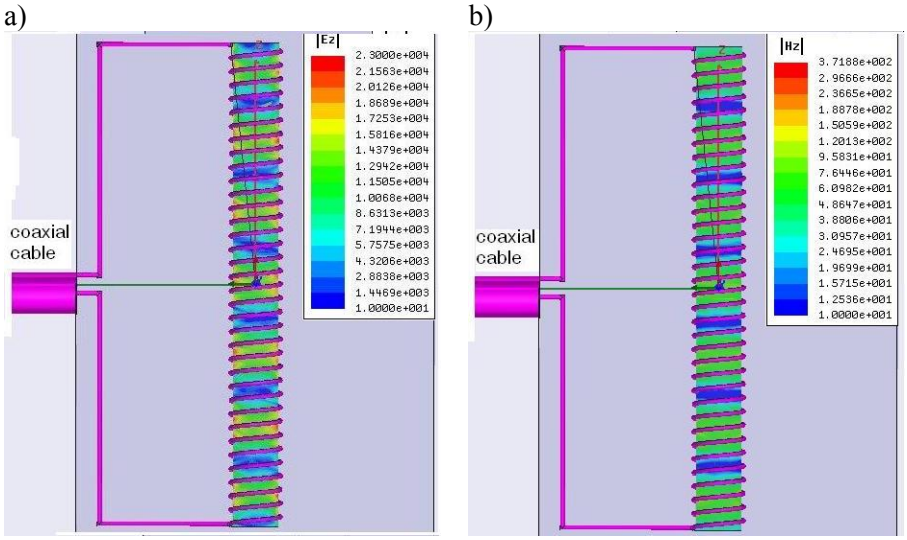

Fig. C.3. Results of the numerical simulations. a) the spatial distribution of |*Ez*| inside a coil fed with a coaxial cable, at f = 1GHz; b) spatial distribution of |*Hz*| inside a coil fed with a coaxial cable, at f = 1GHz.

two profiles it can be noted that there is a satisfactory overlapping of the peak-positions of $|E_z^i|$ and $|H_z^i|$, as well as the null-positions.

The results just described can be completely predicted by considering the only TE_0 and TM_0 modes of the Sheath Helix, as shown in the following.
By applying the Amperé-Maxwell's law to the path c of Fig. C.2 one obtains:

$$\oint_c \mathbf{H}\cdot\mathbf{i}_t dc \cong \int_{l/2-p}^{l/2} H_z^i dz - \int_{l/2-p}^{l/2} H_z^o dz = i + \iint_S \mathbf{E}\cdot\mathbf{i}_n dS \cong i \qquad \text{(C.21)}$$

In eq. (C.21), $\mathbf{i_t}$ is the unit vector tangent to c, S is a surface whose contour is c and $\mathbf{i_n}$ is the unit vector normal to S.
Furthermore, it results:

$$\int_{l/2-p}^{l/2} H_z^i dz = \int_{l/2-p}^{l/2} \frac{\tau}{j\omega\mu} \mathrm{V}_{TE}^i(z) I_0(\tau d/2) dz \cong p \frac{\tau}{j\omega\mu} I_0(\tau d/2) \mathrm{V}_{TE}^i(l/2) =$$
$$-\frac{\tau^2}{k^2} \mathrm{I}_{TM}^i(l/2) I_0(\tau d/2) \frac{I_0(\tau d/2)}{I_1(\tau d/2)} \frac{p^2}{\pi d} \qquad \text{(C.22)}$$

$$\int_{l/2-p}^{l/2} H_z^o dz = \int_{l/2-p}^{l/2} \frac{\tau}{j\omega\mu} \mathrm{V}_{TE}^o(z) K_0(\tau d/2) dz \cong p \frac{\tau}{j\omega\mu} K_0(\tau d/2) \mathrm{V}_{TE}^o(l/2) = \frac{\tau^2}{k^2} \mathrm{I}_{TM}^o(l/2) K_0(\tau d/2) \frac{K_0(\tau d/2)}{K_1(\tau d/2)} \frac{p^2}{\pi d} \tag{C.23}$$

The latter equalities in eqs. (C.22) and (C.23) are consequence of eqs (C.12) and (C.13). Moreover, by exploiting the condition (C.14), eq. (C.23) becomes:

$$\int_{l/2-p}^{l/2} H_z^o dz = \frac{\tau^2}{k^2} \mathrm{I}_{TM}^i(l/2) I_0(\tau d/2) \frac{K_0(\tau d/2)}{K_1(\tau d/2)} \frac{p^2}{\pi d} \tag{C.24}$$

From eqs. (C.21), (C.22) and (C.24) it follows that:

$$i \cong -\frac{\tau^2}{k^2} \frac{p^2}{\pi d} \mathrm{I}_{TM}^i(l/2) I_0(\tau d/2) \left(\frac{I_0(\tau d/2)}{I_1(\tau d/2)} + \frac{K_0(\tau d/2)}{K_1(\tau d/2)} \right) \tag{C.25}$$

Similarly, by applying the Amperé-Maxwell's law to the path *c'* of Fig. C.2 one obtains:

$$i' \cong -\frac{\tau^2}{k^2} \frac{p^2}{\pi d} \mathrm{I}_{TM}^i(-l/2) I_0(\tau d/2) \left(\frac{I_0(\tau d/2)}{I_1(\tau d/2)} + \frac{K_0(\tau d/2)}{K_1(\tau d/2)} \right) \tag{C.26}$$

From eqs (C.25) and (C.26) and by exploiting the symmetry of the structure shown in Fig. C.2 ($i = i'$), it results:

$$\mathrm{I}_{TM}^i(l/2) = \mathrm{I}_{TM}^i(-l/2) \tag{C.27}$$

Since $\mathrm{I}_{TM}^o(z)$ is solution of the set of eqs. (C.10) and (C.11), one has:

$$\mathrm{I}_{TM}^i(z) \propto \cos(\beta z) \tag{C.28}$$

From eqs. (C.6), (C.8), (A. 93) and (C.27) it follows that:

$$\left| E_z^i(z) \right| \propto \left| \cos(\beta z) \right| \tag{C.29}$$

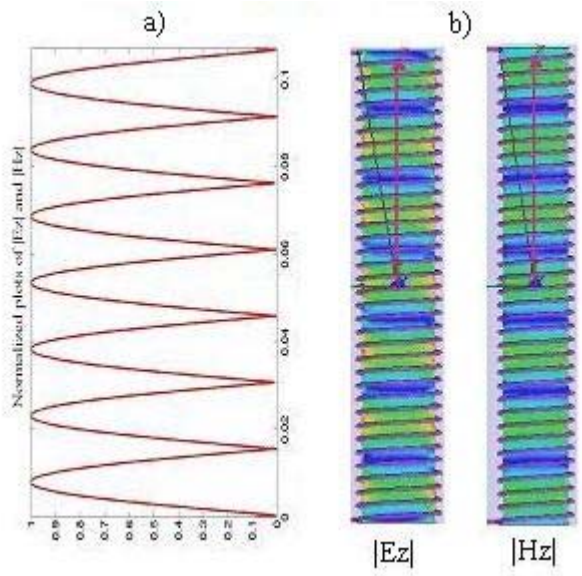

Fig. C.4. a) Profile of $|E_z^i|$ and $|H_z^i|$ in a coil predicted by the Sheath Helix model; b) profiles of $|E_z^i|$ and $|H_z^i|$ in a coil obtained by numerical simulations

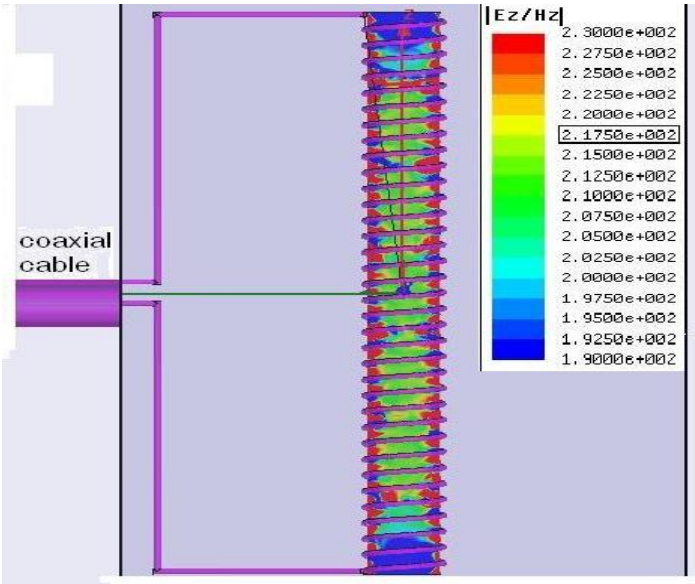

Fig. C.5. a) Spatial distribution of the ratio $|E_z^i/H_z^i|$ in a coil, obtained by numerical simulations

$$\left|H_z^i(z)\right| \propto \left|\cos(\beta z)\right| \tag{C.30}$$

where $\beta = \sqrt{k^2 + \tau^2} \approx 206.2$ m^{-1}.

In Fig. C.4 it is shown the comparison between the profiles of $|E_z^i|$ and $|H_z^i|$ predicted by the Sheath Helix model, i.e. eqs (C.29) and (C.30), and those obtained by simulations. As can be seen there is a good agreement between the two profiles.

Concerning the amplitudes of $|E_z^i|$ and $|H_z^i|$, in Fig. C.5 is displayed the spatial distribution inside the coil of the ratio $|E_z^i/H_z^i|$, obtained by numerical simulations. As can be seen, the ratio is practically constant, as indicated by the large green spot in Fig. C.5, and the value is about 217 Ω, which is very close to $0.6\zeta_0$ = 226 Ω obtained theoretically.

Accordingly, one can conclude that the coil exploited in [5], at f = 1GHz is suitable described by the only fundamental modes of the Sheath Helix model.

Appendix D

Uncertainty analysis

In this appendix for each measurement method discussed in Chapter 4 namely SCCL, OECL, T/R and S/OCL techniques, is derived the expression of the relative uncertainty in estimating ε'_r, ε''_r, μ'_r, μ''_r.

The general expression of the uncertainty here considered is:

$$\frac{\Delta y}{y_0} = \frac{1}{y_0}\sum_{i=1}^{N}\left|\frac{\partial F_y}{\partial x_i}\right|_{x_i=x_{i0}} \left|\Delta x_i\right| + \left|a_y\right| \qquad \text{(D.1)}$$

where y is the measurement result ($y = \varepsilon'_r$, ε''_r, μ'_r or μ''_r), $(x_1,\ldots, x_N)$ are the measurement data, F_y is the function relating $(x_1,\ldots, x_N)$ to y, $(x_{10},\ldots, x_{N0})$ are the values expected for the measurement data (i.e. the data not affected by errors), y_0 is the value expected for the measurement result, $a_y=F_y(x_{10},\ldots,x_{N0})- y_0$, $(\Delta x_1,\ldots, \Delta x_N)$ are the errors on measurement data and Δy the error on the measurement result.

Later on, for each technique above listed, one provides the expressions of a_y and of the sensibility coefficients:

$$c_{yi} = \left|\frac{\partial F_y}{\partial x_i}\right|_{x_i=x_{i0}} \qquad \text{(D.2)}$$

D.1 Expressions of the relative uncertainty for SCCL and OECL techniques

For the SCCL technique the basic equations to be used to estimate μ'_r and μ''_r from the measurement data $(x_1,\ldots, x_N) = (l,\ \Gamma_s)$ are:

$$\mu_r' = F_{\mu' r}\left(l, \Gamma_s\right) = \frac{2}{\beta_0 l}\left(\frac{\Gamma_s''}{1+\left(\Gamma_s'\right)^2+\left(\Gamma_s''\right)^2-2\Gamma_s'}\right) \tag{D.3}$$

$$\mu_r'' = F_{\mu'' r}\left(l, \Gamma_s\right) = \frac{1}{\beta_0 l}\left(\frac{1-\left(\Gamma_s'\right)^2-\left(\Gamma_s''\right)^2{}_s}{1+\left(\Gamma_s'\right)^2+\left(\Gamma_s''\right)^2-2\Gamma_s'}\right) \tag{D.4}$$

where Γ_s' and Γ_s'' are the real and imaginary part of Γ_s.
From eqs. (D.3) and (D.4) it follows that:

$$\frac{\partial F_{\mu' r}}{\partial l} = \frac{-2\Gamma_s''}{\beta_0 l^2\left|1-\Gamma_s\right|^2} \tag{D.5}$$

$$\frac{\partial F_{\mu'' r}}{\partial l} = \frac{\left|\Gamma_s\right|^2-1}{\beta_0 l^2\left|1-\Gamma_s\right|^2} \tag{D.6}$$

$$\frac{\partial F_{\mu' r}}{\partial \Gamma_s'} = -\frac{\partial F_{\mu'' r}}{\partial \Gamma_s''} = 4\frac{\left(1-\Gamma_s'\right)\Gamma_s''}{\beta_0 l\left|1-\Gamma_s\right|^4} \tag{D.7}$$

$$\frac{\partial F_{\mu' r}}{\partial \Gamma_s''} = \frac{\partial F_{\mu'' r}}{\partial \Gamma_s'} = 2\frac{\left(1-\Gamma_s'\right)^2-\left(\Gamma_s''\right)^2}{\beta_0 l\left|1-\Gamma_s\right|^4} \tag{D.8}$$

The eqs (D.5) to (D.8) represent the expressions of the sensibility coefficients for the SCCL method.
Concerning the expression of $a_{\mu' r}$ and $a_{\mu'' r}$, let us note that:

$$j\beta_0 l\left(F_{\mu' r}-jF_{\mu'' r}\right) = \frac{1+\Gamma_s}{1-\Gamma_s} = j\sqrt{\frac{\mu_r}{\varepsilon_r}}\tan\left(\sqrt{\mu_r\varepsilon_r}\,\beta_0 l\right) \cong j\mu_r\beta_0 l + \frac{1}{3}j\mu_r^2\varepsilon_r\left(\beta_0 l\right)^3 \tag{D.9}$$

The right hand of eq. (D.9) is attained by approximating the tangent function with the first two terms of its Taylor series expansion.
From eq. (D.9) one obtains:

$$a_{\mu' r} = F_{\mu' r} - \mu'_r = \frac{1}{3}(\beta_0 l)^2 \, \Re e\{\mu_r^2 \varepsilon_r\} \tag{D.10}$$

$$a_{\mu'' r} = F_{\mu'' r} - \mu''_r = -\frac{1}{3}(\beta_0 l)^2 \, \Im m\{\mu_r^2 \varepsilon_r\} \tag{D.11}$$

For the OECL technique the basic equations to be used to determine ε'_r, and ε''_r from the measurement data $(x_1,\ldots, x_N) = (l,\ \Gamma_o)$ are:

$$\varepsilon'_r = F_{\varepsilon' r}(l, \Gamma_o) = -\frac{2}{\beta_0 l}\left(\frac{\Gamma''_o}{1+(\Gamma'_o)^2+(\Gamma''_o)^2+2\Gamma'_o}\right) \tag{D.12}$$

$$\varepsilon''_r = F_{\varepsilon'' r}(l, \Gamma_o) = \frac{1}{\beta_0 l}\left(\frac{1-(\Gamma'_o)^2-(\Gamma''_o)^2}{1+(\Gamma'_o)^2+(\Gamma''_o)^2+2\Gamma'_o}\right) \tag{D.13}$$

where Γ'_o and Γ''_o are the real and imaginary part of Γ_s.
From eqs. (D.12) and (D.13) one obtain the following expressions for the sensibility coefficients, $a_{\varepsilon' r}$ and $a_{\varepsilon'' r}$:

$$\frac{\partial F_{\varepsilon' r}}{\partial l} = \frac{2\Gamma''_o}{\beta_0 l^2 \left|1+\Gamma_o\right|^2} \tag{D.14}$$

$$\frac{\partial F_{\varepsilon'' r}}{\partial l} = \frac{\left|\Gamma_o\right|^2 - 1}{\beta_0 l^2 \left|1+\Gamma_o\right|^2} \tag{D.15}$$

$$\frac{\partial F_{\varepsilon' r}}{\partial \Gamma'_o} = -\frac{\partial F_{\varepsilon'' r}}{\partial \Gamma''_o} = 4\frac{(1+\Gamma'_o)\Gamma''_o}{\beta_0 l \left|1+\Gamma_o\right|^4} \tag{D.16}$$

$$\frac{\partial F_{\varepsilon'' r}}{\partial \Gamma'_o} = \frac{\partial F_{\varepsilon' r}}{\partial \Gamma''_o} = -2\frac{(1+\Gamma'_o)^2 - (\Gamma''_o)^2}{\beta_0 l \left|1+\Gamma_o\right|^4} \tag{D.17}$$

$$a_{\varepsilon' r} = F_{\varepsilon' r} - \varepsilon_r' = \frac{1}{3}(\beta_0 l)^2 \,\Re e\{\mu_r \varepsilon_r^2\} \tag{D.18}$$

$$a_{\varepsilon'' r} = F_{\varepsilon'' r} - \varepsilon_r'' = -\frac{1}{3}(\beta_0 l)^2 \,\Im m\{\mu_r \varepsilon_r^2\} \tag{D.19}$$

D.2 Expressions of the relative uncertainty for the T/R method

For the T/R method the basic equations relating the measurement data $(x_1,\ldots, x_N) = (l, S_{11}, S_{21})$ to ε'_r, ε''_r, μ'_r, μ''_r are:

$$S_{11} = \frac{(1-T^2)\Gamma}{1-T^2\Gamma^2} \tag{D.20}$$

$$S_{21} = \frac{(1-\Gamma^2)T}{1-T^2\Gamma^2} \tag{D.21}$$

$$\Gamma = \frac{\sqrt{\mu_r} - \sqrt{\varepsilon_r}}{\sqrt{\mu_r} + \sqrt{\varepsilon_r}} \tag{D.22}$$

$$T = e^{-jkl} = e^{-j\sqrt{\mu_r \varepsilon_r}\beta_0 l} \tag{D.23}$$

By differentiating eqs. (D.20) to (D.23) one obtains:

$$dS_{11} = \frac{\partial S_{11}}{\partial \Gamma} d\Gamma + \frac{\partial S_{11}}{\partial T} dT = \frac{S_{11}}{\Gamma}\frac{1+T^2\Gamma^2}{1-T^2\Gamma^2} d\Gamma - \frac{2S_{11}S_{21}}{1-T^2} dT = A_\Gamma d\Gamma + A_T dT \tag{D.24}$$

$$dS_{21} = \frac{\partial S_{21}}{\partial \Gamma} d\Gamma + \frac{\partial S_{21}}{\partial T} dT = \frac{-2S_{11}S_{21}}{1-\Gamma^2} d\Gamma + \frac{S_{21}}{T}\frac{1+T^2\Gamma^2}{1-T^2\Gamma^2} dT = B_\Gamma d\Gamma + B_T dT \tag{D.25}$$

$$d\Gamma = \frac{\partial \Gamma}{\partial \mu_r} d\mu_r + \frac{\partial \Gamma}{\partial \varepsilon_r} d\varepsilon_r = \frac{\varepsilon_r d\mu_r - \mu_r d\varepsilon_r}{\sqrt{\mu_r \varepsilon_r}\left(\sqrt{\mu_r} + \sqrt{\varepsilon_r}\right)^2} = C_{\mu r} d\mu_r + C_{\varepsilon r} d\varepsilon_r \tag{D.26}$$

$$\begin{aligned} dT &= \frac{\partial T}{\partial \mu_r} d\mu_r + \frac{\partial T}{\partial \varepsilon_r} d\varepsilon_r + \frac{\partial T}{\partial l} dl = \\ &-j\sqrt{\mu_r \varepsilon_r}\,\beta_0 T dl - j\frac{\beta_0 l}{2}\sqrt{\frac{\varepsilon_r}{\mu_r}} T d\mu_r - j\frac{\beta_0 l}{2}\sqrt{\frac{\mu_r}{\varepsilon_r}} T d\varepsilon_r = D_l dl + D_{\mu r} d\mu_r + D_{\varepsilon r} d\varepsilon_r \end{aligned} \tag{D.27}$$

By substituting eqs. (D.26) and (D.27) in eqs (D.24) and (D.25) yields:

$$dS_{11} = \left(A_\Gamma C_{\mu r} + A_T D_{\mu r}\right) d\mu_r + \left(A_\Gamma C_{\varepsilon r} + A_T D_{\varepsilon r}\right) d\varepsilon_r + A_T D_l dl \tag{D.28}$$

$$dS_{21} = \left(B_\Gamma C_{\mu r} + B_T D_{\mu r}\right) d\mu_r + \left(B_\Gamma C_{\varepsilon r} + B_T D_{\varepsilon r}\right) d\varepsilon_r + B_T D_l dl \tag{D.29}$$

By solving the system of linear eqs. (D.28) and (D.29) with respect to $d\varepsilon_r$, $d\mu_r$, we get:

$$d\mu_r = A_{S_{11}} dS_{11} + A_{S_{21}} dS_{21} + A_l dl \tag{D.30}$$

$$d\varepsilon_r = B_{S_{11}} dS_{11} + B_{S_{21}} dS_{21} + B_l dl \tag{D.31}$$

where:

$$A_{S_{11}} = \frac{\left(B_\Gamma C_{\varepsilon r} + B_T D_{\varepsilon r}\right)}{\left(A_\Gamma C_{\mu r} + A_T D_{\mu r}\right)\left(B_\Gamma C_{\varepsilon r} + B_T D_{\varepsilon r}\right) - \left(A_\Gamma C_{\varepsilon r} + A_T D_{\varepsilon r}\right)\left(B_\Gamma C_{\mu r} + B_T D_{\mu r}\right)} \tag{D.32}$$

$$A_{S_{21}} = \frac{-\left(A_\Gamma C_{\varepsilon r} + A_T D_{\varepsilon r}\right)}{\left(A_\Gamma C_{\mu r} + A_T D_{\mu r}\right)\left(B_\Gamma C_{\varepsilon r} + B_T D_{\varepsilon r}\right) - \left(A_\Gamma C_{\varepsilon r} + A_T D_{\varepsilon r}\right)\left(B_\Gamma C_{\mu r} + B_T D_{\mu r}\right)} \tag{D.33}$$

$$A_l = \frac{\left(A_\Gamma C_{\varepsilon r} + A_T D_{\varepsilon r}\right) B_T D_l - \left(B_\Gamma C_{\varepsilon r} + B_T D_{\varepsilon r}\right) A_T D_l}{\left(A_\Gamma C_{\mu r} + A_T D_{\mu r}\right)\left(B_\Gamma C_{\varepsilon r} + B_T D_{\varepsilon r}\right) - \left(A_\Gamma C_{\varepsilon r} + A_T D_{\varepsilon r}\right)\left(B_\Gamma C_{\mu r} + B_T D_{\mu r}\right)} \tag{D.34}$$

$$B_{S_{11}} = \frac{-\left(B_\Gamma C_{\mu r} + B_T D_{\mu r}\right)}{\left(A_\Gamma C_{\mu r} + A_T D_{\mu r}\right)\left(B_\Gamma C_{\varepsilon r} + B_T D_{\varepsilon r}\right) - \left(A_\Gamma C_{\varepsilon r} + A_T D_{\varepsilon r}\right)\left(B_\Gamma C_{\mu r} + B_T D_{\mu r}\right)} \tag{D.35}$$

$$B_{S_{21}} = \frac{\left(A_\Gamma C_{\mu r} + A_T D_{\mu r}\right)}{\left(A_\Gamma C_{\mu r} + A_T D_{\mu r}\right)\left(B_\Gamma C_{\varepsilon r} + B_T D_{\varepsilon r}\right) - \left(A_\Gamma C_{\varepsilon r} + A_T D_{\varepsilon r}\right)\left(B_\Gamma C_{\mu r} + B_T D_{\mu r}\right)} \tag{D.36}$$

$$B_l = \frac{\left(B_\Gamma C_{\mu r} + B_T D_{\mu r}\right) A_T D_l - \left(A_\Gamma C_{\mu r} + A_T D_{\mu r}\right) B_T D_l}{\left(A_\Gamma C_{\mu r} + A_T D_{\mu r}\right)\left(B_\Gamma C_{\varepsilon r} + B_T D_{\varepsilon r}\right) - \left(A_\Gamma C_{\varepsilon r} + A_T D_{\varepsilon r}\right)\left(B_\Gamma C_{\mu r} + B_T D_{\mu r}\right)} \tag{D.37}$$

The real and imaginary parts of the complex quantities given in eqs (D.32) to (D.37) represent the sensibility coefficients to be used in eq. (D.1) to evaluate the relative uncertainty of the T/R method in estimating ε'_r, ε''_r, μ'_r, μ''_r.

Concerning the expression of $a_{\mu' r}$, $a_{\mu'' r}$, $a_{\varepsilon' r}$ and $a_{\varepsilon'' r}$, since eqs. (D.20) to (D.23) relating the measurement data l, S_{11}, S_{21} to ε'_r, ε''_r, μ'_r, μ''_r are not approximated, it results: $a_{\mu' r} = a_{\mu'' r} = a_{\varepsilon' r} = a_{\varepsilon'' r} = 0$.

D.3 Expressions of the relative uncertainty for the S/OCL technique

For the S/OCL technique the basic equations to be used to estimate μ_r and ε_r from the measurement data $(x_1, \ldots, x_N) = (l,\ \Gamma_s\ ,\ \Gamma_o\ )$ are:

$$\frac{1+\Gamma_s}{1-\Gamma_s} = Z = j\sqrt{\frac{\mu_r}{\varepsilon_r}}\tan\left(\sqrt{\mu_r \varepsilon_r}\,\beta_0 l\right) \tag{D.38}$$

$$\frac{1-\Gamma_o}{1+\Gamma_o} = Y = j\sqrt{\frac{\varepsilon_r}{\mu_r}}\tan\left(\sqrt{\mu_r \varepsilon_r}\,\beta_0 l\right) \tag{D.39}$$

By differentiating eqs. (D.38) and (D.39) one obtains:

$$d\Gamma_s = A_{\mu r}\, d\mu_r + A_{\varepsilon r}\, d\varepsilon_r + A_l\, dl \tag{D.40}$$

$$d\Gamma_o = B_{\mu r} d\mu_r + B_{\varepsilon r} d\varepsilon_r + B_l dl \tag{D.41}$$

where:

$$A_{\mu r} = \frac{\left(1-\Gamma_s\right)^2}{2}\frac{\partial Z}{\partial \mu_r} = \frac{\left(1-\Gamma_s\right)^2}{4}\left(\frac{Z}{\mu_r} + j\beta_0 l\left(1-ZY\right)\right) \tag{D.42}$$

$$A_{\varepsilon r} = \frac{\left(1-\Gamma_s\right)^2}{2}\frac{\partial Z}{\partial \varepsilon_r} = \frac{\left(1-\Gamma_s\right)^2}{4}\left(-\frac{Z}{\varepsilon_r} + j\frac{\mu_r}{\varepsilon_r}\beta_0 l\left(1-ZY\right)\right) \tag{D.43}$$

$$A_l = \frac{\left(1-\Gamma_s\right)^2}{2}\frac{\partial Z}{\partial l} = j\frac{\left(1-\Gamma_s\right)^2}{2}\mu_r\beta_0\left(1-ZY\right) \tag{D.44}$$

$$B_{\mu r} = -\frac{\left(1+\Gamma_o\right)^2}{2}\frac{\partial Y}{\partial \mu_r} = \frac{\left(1+\Gamma_o\right)^2}{4}\left(\frac{Y}{\mu_r} - j\frac{\varepsilon_r}{\mu_r}\beta_0 l\left(1-ZY\right)\right) \tag{D.45}$$

$$B_{\varepsilon r} = -\frac{\left(1+\Gamma_o\right)^2}{2}\frac{\partial Y}{\partial \varepsilon_r} = -\frac{\left(1+\Gamma_o\right)^2}{4}\left(\frac{Z}{\mu_r} + j\beta_0 l\left(1-ZY\right)\right) \tag{D.46}$$

$$B_l = -\frac{\left(1+\Gamma_o\right)^2}{2}\frac{\partial Z}{\partial l} = -j\frac{\left(1+\Gamma_o\right)^2}{2}\varepsilon_r\beta_0\left(1-ZY\right) \tag{D.47}$$

By solving the system of linear eqs. (D.40) and (D.41) with respect to $d\varepsilon_r$, $d\mu_r$, we get:

$$d\mu_r = A_{\Gamma s} d\Gamma_s + A_{\Gamma o} d\Gamma_o + C_{l1} dl \tag{D.48}$$

$$d\varepsilon_r = B_{\Gamma s} d\Gamma_s + B_{\Gamma o} d\Gamma_o + C_{l2} dl \tag{D.49}$$

where:

$$A_{\Gamma s} = \frac{1}{\left(1-\Gamma_s\right)^2}\left(\frac{\mu_r}{Z} - \frac{j}{\beta_0 l\left(1-ZY\right)}\right) \tag{D.50}$$

$$A_{\Gamma o} = \frac{1}{\left(1+\Gamma_o\right)^2}\left(\frac{\mu_r}{Y} + \frac{\mu_r}{\varepsilon_r}\frac{j}{\beta_0 l\left(1-ZY\right)}\right) \tag{D.51}$$

$$C_{l1} = -\frac{\mu_r}{l} \tag{D.52}$$

$$B_{\Gamma s} = -\frac{1}{\left(1-\Gamma_s\right)^2}\left(\frac{\varepsilon_r}{Z} + \frac{\varepsilon_r}{\mu_r}\frac{j}{\beta_0 l\left(1-ZY\right)}\right) \tag{D.53}$$

$$B_{\Gamma o} = -\frac{1}{\left(1+\Gamma_o\right)^2}\left(\frac{\varepsilon_r}{Y} - \frac{j}{\beta_0 l\left(1-ZY\right)}\right) \tag{D.54}$$

$$C_{l2} = -\frac{\varepsilon_r}{l} \tag{D.55}$$

The real and imaginary parts of the complex quantities given in eqs (D.50) to (D.55) represent the sensibility coefficients to be used in eq. (D.1) to evaluate the relative uncertainty of the S/OCL technique in estimating ε'_r, ε''_r, μ'_r, μ''_r.

Concerning the expression of $a_{\mu' r}$, $a_{\mu'' r}$, $a_{\varepsilon' r}$ and $a_{\varepsilon'' r}$, since eqs. (D.38) and (D.39) relating the measurement data l, Γ_s, Γ_o to ε'_r, ε''_r, μ'_r, μ''_r are exact, it follows that: $a_{\mu' r} = a_{\mu'' r} = a_{\varepsilon' r} = a_{\varepsilon'' r} = 0$.

Appendix E

Exact solution of the Pennen's Bio-Heat Equation in a finite spherical region characterized by a step-like heat generation

In this Appendix it is derived the expression of the temperature field, $T(r, t)$, given in eq. (6.5). Furthermore, it is shown that, at any time $t \geq 0$, $T(r, t)$ monotonically decreases with r.

The differential problems to be solved to determine $T(r, t)$ is (Sec. 6.1):

$$\frac{\partial T(r,t)}{\partial t} = \alpha^2 \frac{1}{r^2} \frac{\partial}{\partial r}\left(r^2 \frac{\partial T(r,t)}{\partial r} \right) - \frac{w_b}{\rho}\left(T(r,t) - T_0 \right) + \frac{q_{1m} + q_{1e}}{\rho c} \tag{E.1}$$

$$T(r,0) = T_0 \tag{E.2}$$

$$T(R_0,t) = T_0 \tag{E.3}$$

where:

$$q_{1m} = p_m \Pi\left(\frac{r - 0.5R_1}{R_1} \right) \tag{E.4a}$$

$$q_{1e} = p_e \tag{E.4b}$$

In eq. (E.4a) $\Pi(x)$ is a step function whose value is one for $x \in (-0.5, 0.5)$ and zero elsewhere.

For the basics, let us refer to the definitions introduced in Sec. 6.1.

Due to the linearity of the set of eqs. (E.1) – (E.4), $T(r, t)$ can be expressed as the superposition of two auxiliary temperature fields: $T(r, t) = T_0(r, t) + T_1(r, t)$, where $T_0(r, t)$ is solution of the problem:

$$\frac{\partial T_0(r,t)}{\partial t} = \alpha^2 \frac{1}{r^2} \frac{\partial}{\partial r}\left(r^2 \frac{\partial T_0(r,t)}{\partial r} \right) - \frac{w_b}{\rho}\left(T_0(r,t) - T_0 \right) \tag{E.5}$$

$$T_0(r,0) = T_0 \tag{E.6}$$

$$T_0(R_0,t) = T_0 \tag{E.7}$$

and $T_1(r, t)$ is solution of the problem:

$$\frac{\partial T_1(r,t)}{\partial t} = \alpha^2 \frac{1}{r^2} \frac{\partial}{\partial r}\left(r^2 \frac{\partial T_1(r,t)}{\partial r} \right) - \frac{w_b}{\rho} T_1(r,t) + \frac{q_{1m} + q_{1e}}{\rho c} \tag{E.8}$$

$$T_1(r,0) = 0 \tag{E.9}$$

$$T_1(R_0,t) = 0 \tag{E.10}$$

Concerning $T_0(r, t)$, one can immediately note that the unique solution of the problem (E.8) – (E.10) is $T_0(r, t) \equiv T_0$.

Concerning $T_1(r, t)$, defined the scalar field:

$$\Phi(r,t) = r T_1(r,t) \exp\left(\frac{w_b}{\rho} t \right) \tag{E.11}$$

it can be easily proved that $\Phi(r, t)$ satisfies the following Cauchy-Dirichlet problem:

$$\frac{\partial \Phi(r,t)}{\partial t} = \alpha^2 \frac{\partial^2 \Phi(r,t)}{\partial r^2} + Q(r,t) \tag{E.12}$$

$$\Phi(r,0) = 0 \tag{E.13}$$

$$\Phi(0,t)=0 \tag{E.14}$$

$$\Phi(R_0,t)=0 \tag{E.15}$$

where:

$$Q(r,t)=\frac{q_{1m}+q_{1e}}{\rho c}r\exp\left(\frac{w_b}{\rho}t\right) \tag{E.16}$$

Accordingly, the expression of $T_1(r, t)$ can be derived by solving the problem (E.12) – (E.16) and applying the relation (E.11).

It is convenient to transform the problem (E.8) – (E.10) into the problem (E.12) – (E.16) in that for the latter class of differential problems the expression of the solution is well-known and is [83]:

$$\Phi(r,t)=\sum_{n=1}^{+\infty}\phi_n(t)\sin(h_n r) \tag{E.17}$$

where $h_n = n\pi/R_0$ and $\phi_n(t)$ satisfy the following ordinary differential problem:

$$\begin{cases}\dfrac{d\phi_n(t)}{dt}+\alpha^2h_n^2\phi_n(t)=\dfrac{2}{R_0}\displaystyle\int_0^{R_0}Q(r,t)\sin(h_n r)\,dr+\alpha^2h_n\left((-1)^n\Phi(R_0,t)-\Phi(0,t)\right)\\ \phi_n(0)=\dfrac{2}{R_0}\displaystyle\int_0^{R_0}\Phi(r,0)\sin(h_n r)\,dr\end{cases} \tag{E.18}$$

From eqs. (E.13) – (E.16) one obtains:

$$\begin{cases}\dfrac{d\phi_n(t)}{dt}+\alpha^2h_n^2\phi_n(t)=\dfrac{a_n}{\rho c}\exp\left(\dfrac{w_b}{\rho}t\right)\\ \phi_n(0)=0\end{cases} \tag{E.19}$$

where:

$$a_n = \frac{2}{R_0}\int_0^{R_0}\left(q_{1m}+q_{1e}\right)\sin\left(h_n r\right)rdr = \frac{2}{n\pi h_n}\left(\sin\left(h_n R_1\right)-h_n R_1\cos\left(h_n R_1\right)\right)p_m+\left(-1\right)^{n+1}\frac{2}{h_n}p_e = a_{m,n}p_m+a_{e,n}p_e \tag{E.20}$$

By solving the set of eqs. (E.19) one attains:

$$\phi_n\left(t\right)=\frac{a_{m,n}p_m+a_{e,n}p_e}{w_b c+\rho c\alpha^2 h_n^2}\left(1-\exp\left(-\frac{w_b}{\rho}t-\alpha^2 h_n^2 t\right)\right)\exp\left(\frac{w_b}{\rho}t\right) \tag{E.21}$$

By replacing eq. (E.21) in eq. (E.17) and applying the relation (E.11) it results:

$$T_1\left(r,t\right)=\sum_{n=1}^{+\infty}\frac{a_{m,n}p_m}{w_b c+\rho c\alpha^2 h_n^2}\left(1-\exp\left(-\frac{w_b}{\rho}t-\alpha^2 h_n^2 t\right)\right)\sin\left(h_n r\right)/r+ \sum_{n=1}^{+\infty}\frac{a_{e,n}p_e}{w_b c+\rho c\alpha^2 h_n^2}\left(1-\exp\left(-\frac{w_b}{\rho}t-\alpha^2 h_n^2 t\right)\right)\sin\left(h_n r\right)/r = T_{1m}\left(r,t\right)+T_{1e}\left(r,t\right) \tag{E.22}$$

In eq. (E.22) $T_{1m}(r, t)$ and $T_{1e}(r, t)$ represent the solutions of the problem (E.8) – (E.10) when $q_{1e} = 0$ and $q_{1m} = 0$, respectively.
In conclusion:

$$T\left(r,t\right)=T_0\left(r,t\right)+T_1\left(r,t\right)= T_0+\sum_{n=1}^{+\infty}\frac{a_{m,n}p_m+a_{e,n}p_e}{w_b c+\rho c\alpha^2 h_n^2}\left(1-\exp\left(-\frac{w_b}{\rho}t-\alpha^2 h_n^2 t\right)\right)\sin\left(h_n r\right)/r \tag{E.23}$$

In eq. (E.23), by setting $\xi = r/R_0$, $\tau = (\alpha/R_0)^2 t$, $\alpha = (k/\rho c)^{1/2}$, $\beta = w_b c R_0^2/k$, $p'_{m[e]} = (R_0^2/k)p_{m[e]}$ one obtains the expression of $T(r, t)$ given in eq. (6.5).

Later on, it will be demonstrated that, at any time $t \geq 0$, $T(r, t)$ monotonically decreases with r.

To show this, firstly, one needs to demonstrate the following preliminary results:

1. denoted with $T_1'_{m[e]}(r, t)$ the solution of the problem (E.8) – (E.10) for $w_b = 0$ and $q_{1e} = 0$ [$q_{1m} = 0$], $\partial T_{1m[e]}/\partial t = (\partial T_1'_{m[e]}/\partial t)\exp(-w_b t/\rho)$;
2. $0 \leq \partial T_{1m[e]}/\partial t \leq p_{m[e]}\exp(-w_b t/\rho)/\rho c$;

3. $0 \le (w_b/\rho)T_{1m[e]}(r, t) \le p_{m[e]}(1-\exp(-w_b t/\rho))/\rho c$;
4. $\partial T_{1m}/\partial r$ evaluated at $r = R_0$ is non positive.

Point 1 can be easily proved differentiating by series the first [second] term of eq. (E.22), in turn, for $w_b = 0$ and $w_b \neq 0$ and comparing the two expressions.
It is worth noting that it is possible to differentiate by series eq. (E.22) in that:

$$\sum_{n=1}^{+\infty}\left|\frac{a_{m,n}p_m + a_{e,n}p_e}{w_b c + \rho c\alpha^2 h_n^2}\right|\left|1-\exp\left(-\frac{w_b}{\rho}t-\alpha^2 h_n^2 t\right)\right|\left|\sin\left(h_n r\right)/r\right| \le M\sum_{n=1}^{+\infty}\frac{R_0^2}{w_b c R_0^2 + \rho c\alpha^2\left(n\pi\right)^2} < +\infty \tag{E.24}$$

where:

$$M = \frac{2}{R_0}\int_0^{R_0} q_1 r dr \tag{E.25}$$

Concerning point 2, since $\partial T_1'_{m[e]}/\partial t$ is solution of the following problem:

$$\frac{\partial\left(\partial T'_{1m[e]}/\partial t\right)}{\partial t} = \alpha^2\frac{1}{r^2}\frac{\partial}{\partial r}\left(r^2\frac{\partial\left(\partial T'_{1m[e]}/\partial t\right)}{\partial r}\right) \tag{E.26}$$

$$\frac{\partial T'_{1m[e]}\left(r,0\right)}{\partial t} = \frac{q_{1m}}{\rho c}\left[\frac{q_{1e}}{\rho c}\right] \tag{E.27}$$

$$T'_{1t}\left(R_0,t\right) = 0 \tag{E.28}$$

for the maximum's principle [83] it results: $0 \le \partial T_1'_{m[e]}/\partial t \le \max(q_{1\,m[e]}/\rho c) = p_{m[e]}/\rho c$.
Moreover, since $\partial T_{1m[e]}/\partial t = (\partial T_1'_{m[e]}/\partial t)\exp(-w_b t/\rho)$, it follows that:

$$0 \le \frac{\partial T_{1m[e]}}{\partial t} \le \frac{p_{m[e]}}{\rho c}\exp\left(-w_b t/\rho\right) \tag{E.29}$$

Point 3 can be proved by noting that:

$$0 \le \frac{w_b}{\rho}\int_0^t \frac{\partial T_{1m[e]}(r,\upsilon)}{\partial \upsilon} d\upsilon = \frac{w_b}{\rho} T_{1m[e]}(r,t) \le \frac{p_{m[e]}}{\rho c}\int_0^t \frac{w_b}{\rho}\exp\left(-\frac{w_b}{\rho}\upsilon\right) d\upsilon = \frac{p_{m[e]}}{\rho c}\left(1-\exp\left(-w_b t/\rho\right)\right) \tag{E.30}$$

The first and third inequalities are due to eq. (E.29); the second equality is a consequence of eq. (E.9).
Finally, point 4 can be easily proved by noting that for $r \le R_0$ $T_{1m}(r, t) \ge T_{1m}(R_0, t) = 0$.
Now, one can demonstrate that monotonically decreases with r. This can be shown by proving that $\partial T/\partial r = \partial T_{1m}/\partial r + \partial T_{1e}/\partial r \le 0$.
Concerning $\partial T_{1e}/\partial r$, from eq. (E.8) one obtains :

$$\left[\alpha^2 r^2 \frac{\partial T_{1e}}{\partial r}\right]_0^r = \alpha^2 r^2 \frac{\partial T_{1e}(r,t)}{\partial r} = \int_0^r \left(\frac{\partial T_{1e}(\eta,t)}{\partial t} + \frac{w_b}{\rho} T_{1e}(\eta,t) - \frac{p_e}{\rho c}\right)\eta^2 d\eta \le 0 \tag{E.31}$$

The last inequality in eq. (E.31) derives from the relations (E.29) and (E.30). Accordingly, $\alpha^2 r^2(\partial T_{1e}/\partial r) \le 0$, i.e. $\partial T_{1e}/\partial r \le 0$.
Concerning $\partial T_{1m}/\partial r$, from eq. (E.8) one obtains :

$$\alpha^2 r^2 \frac{\partial T_{1m}(r,t)}{\partial r} = \int_0^r \left(\frac{\partial T_{1m}(\eta,t)}{\partial t} + \frac{w_b}{\rho} T_{1m}(\eta,t) - \frac{p_m}{\rho c}\right)\eta^2 d\eta \quad \text{for } 0 \le r \le R_1,\ t \ge 0 \tag{E.32a}$$

$$\alpha^2 r^2 \frac{\partial T_{1m}(r,t)}{\partial r} = \int_0^{R_1} \left(\frac{\partial T_{1m}(\eta,t)}{\partial t} + \frac{w_b}{\rho} T_{1m}(\eta,t) - \frac{p_m}{\rho c}\right)\eta^2 d\eta + \int_{R_1}^r \left(\frac{\partial T_{1m}(\eta,t)}{\partial t} + \frac{w_b}{\rho} T_{1m}(\eta,t)\right)\eta^2 d\eta = f(t) + g(r,t) \quad \text{for } R_1 \le r \le R_0,\ t \ge 0 \tag{E.32b}$$

By exploiting the inequalities (E.29) and (E.30) one can easily note that the integral on the right hand of eq. (E.32a) is non positive. Accordingly, for $0 \le r \le R_1$ and $t \ge 0$ $\alpha^2 r^2(\partial T_{1m}/\partial r) \le 0$, i.e. $\partial T_{1m}/\partial r \le 0$.
Concerning eq. (E.32b), the integral denoted with $f(t)$ is non positive while the integral denoted with $g(r, t)$ is non negative and increases monotonically with r (the latter property of $g(r, t)$ is a consequence of the inequalities:

$\partial T_{1m}/\partial t \geq 0$ and $(w_b/\rho)T_{1m}(r, t) \geq 0$). Accordingly, the maximum of $\alpha^2 r^2(\partial T_{1m}/\partial r)$ is assumed for $r = R_0$. Moreover, due to point 4 this maximum is non positive. As a result, for $R_1 \leq r \leq R_0$ and $t \geq 0$ $\alpha^2 r^2(\partial T_{1m}/\partial r) \leq 0$, i.e. $\partial T_{1m}/\partial r \leq 0$

In conclusion, for $0 \leq r \leq R_0$ and $t \geq 0$, $\partial T_{1m}/\partial r \leq 0$ and $\partial T_{1e}/\partial r \leq 0$, hence $\partial T/\partial r \leq 0$.

References

[1] Leslie-Pelecky DL, Labhasetwar V, Kraus RH, "Nanobiomagnetics", Advanced Magnetic Nanostructures (Springer, 2006), pp. 461-490, 2006.

[2] Phillips JL, "A topical review of magnetic fluid hyperthermia" available on www.bama.ua.edu/~joshua/archive/aug05.

[3] Bucci OM, "Electromagnetic control of micro and nano-machines for biotechnological applications", URSI-EMTS, Pisa, 2004.

[4] La Van DA, McGuire T, Langer R, "Small-scale systems for in vivo drug delivery", Nature Biotechnology, vol. 21(10), pp, 1184–1191, 2003.

[5] Hamad-Schifferli K, Schwartz JJ, Santos AT, Zhang S, Jacobson JM, "Remote electronic control of DNA hybridization through inductive coupling to an attached metal nanocrystal antenna", Nature, vol. 415, pp. 152–155, 2002.

[6] Alberti, P, Mergny, JL, "DNA duplex-quadruplex exchange at the basis for a nanomolecular machine", Proc. Natl. Acad. Sci. USA, vol. 100, pp. 1569–1573, 2003.

[7] Niemeyer CM, Adler M, Lenhert S, Gao S, Fuchs H, Chi L, "Nucleic acid supercoiling as a means for ionic switching of DNA--nanoparticle networks.", ChemBioChem, vol. 2, pp. 260–264,2001.

[8] Mornet S, Vasseur S, Grasset F, Duguet E, "Magnetic nanoparticle design for medical diagnosis and therapy", J. Mater. Chem., vol. 14, pp. 2161- 2175, 2004.

[9] Pankhurst QA, Connolly J, Jones SK, Dobson J, "Applications of magnetic nanoparticles in biomedicine", Journal of Physics D: Applied Physics, vol 36, pp. R167-R181, 2003.

[10] Jordan A, Scholz R, Wust P, Fahling H, Felix R, ""Magnetic fluid hyperthermia (MFH): Cancer treatment with AC magnetic field induced excitation of biocompatible superparamagnetic nanoparticles",", J. Magn. Magn. Mater., vol. 201, pp. 413–419, 1999.

[11] Gel'vich EA, Mazokhin VN, "Technical aspects of electromagnetic hyperthermia in medicine ", Crit. Rev. Biomed. Eng, vol. 29, pp. 77–97, 2001.

[12] Gilchrist RK, Medal R, Shorey WD, Hanselman RC, Parrott JC, Taylor CB, "Selective inductive heating of lymph nodes", *Ann. Surg*., vol. 146, pp. 596–606, 1957.

[13] Hilger I, Hiergeist R, Hergt R, Winnefeld K, Schubert H, Kaiser WA, "Thermal ablation of tumours using magnetic nanoparticles, Investigative Radiology, vol. 37 n° 10, pp. 580-586, 2002.

[14] Wada S, Yue L, Tazawa K, Furuta I, Nagae H, Takemori S, Minamimura T, "New local hyperthermia using dextran magnetite complex (DM) for oral cavity: experimental study in normal hamster tongue", Oral Diseased, vol. 7, pp. 192-195, 2001.

[15] Brezovich IA, "Low frequency hyperthermia", *Med. Phys. Monograph*, vol. 16, pp. 82–111, 1988.

[16] Hergt R, Andra W, D'Ambly CG, Hilger I, Kaiser WA, Richter U, Schmidt HG, "Physical Limits of Hyperthermia Using Magnetite Fine Particles", IEEE Transaction on magnetics, vol. 34, pp. 3745-3754, 1998.

[17] Hergt R, Hiergeist , Hilger I, Kaiser WA, Lapatnikov Y, Margel S, Richter U, "Maghemite nanoparticles with very high AC-losses for application in RF-magnetic hyperthermia", J. Magn. Magn. Mater, vol. 270, pp. 345–357, 2004.

[18] Glockl G, Hergt R, Zeisberger M, Dutz S, Nagel1 S, Weitschies1 W, "The effect of field parameters, nanoparticle properties and immobilization on the specific heating power in magnetic p.article hyperthermia", J. Phys.: Condenser. Matter, vol. 18, pp. S2935–S2949, 2006.

[19] Brusentsov NA, Gogosov V, Brusentsova TN, Sergeev AV, Jurchenko NY, Kuznetsov AA, Kuznetsov OA, Shumakov LI, "Evaluation of ferromagnetic Fuids and suspensions for the site-specific radiofrequency-induced hyperthermia of MX11 sarcoma cells in vitro " J. Magn. Magn. Mater, vol. 225, pp. 113–117, 2001.

[20] Wanga X, Gu H, Yang Z, "The heating effect of magnetic fluids in an alternating magnetic field", J. Magn. Magn. Mater., vol. 293, pp. 334-340, 2005.

[21] Jordan A, Scholz R, Wust P, Fähling H, Krause J, Wlodarczyk W, Sander B, Vogl T, Felix R, "Effects of Magnetic Fluid Hyperthermia (MFH) on C3H Mammary Carcinoma In Vivo." *International Journal of Hyperthermia*, vol. 13, pp. 587-605, 1997.

[22] DeNardo SJ, DeNardo GL, Natarajan A, Miers LA, Foreman AR, Gruettner C, Adamson GN, Ivkov R, "Thermal Dosimetry Predictive of Efficacy of ^{111}In-ChL6 Nanoparticle AMF–Induced Thermoablative Therapy for Human Breast Cancer in Mice", Journal of Nuclear Medicine, vol. 48pp. 437-444, 2007.

[23] Kogan MJ, Bastus NG, Amigo R, Grillo-Bosch D, Araya E, Turiel A, Labarta A, Giralt E, Puntes VF. 2006. Nanoparticle-mediated local and remote manipulation of protein aggregation. Nano Letters 6:110–115.

[24] Van Bladel J, "Electromagnetic fields", McGraw-Hill New York, 1964.

[25] Bucci EM, Bellizzi G, Bucci OM, Calabrese ML, Capozzoli A, Messere A, Milano G, Musumeci D, Petraglia G, Roviello G, Massa R, "Remote control of biomolecules by radiofrequency: a test study", Bioelectromagnetics Society 28th Annual Meeting, pp. 471–472, 2006.

[26] Shiliomis MI, Raikher YL, "Experimental investigation of magnetic fluids", IEEE trans. on magnetic, vol. 16, pp. 237-250, 1980.

[27] Skomski R, "Nanomagnetics", J. Phys. C.: Condenser Matter, vol. 15, pp. 841-896, 2003.

[28] Pankhurst QA, Connolly J, Jones SK, Dobson J, "Applications of magnetic nanoparticles in biomedicine", J. Phys. D: Appl. Phys., vol. 36, pp. 167–181, 2003.

[29] Malaescu I, Marin CN, "Study of magnetic fluids by means of magnetic spectroscopy", Physica B, vol. 365 , pp. 134–140, 2005.

[30] Raikher YL, Stepanov VI, **"**Stochastic resonance in single-domain particles**",** J. Phys.: Condens. Matter, vol. 6, pp. 4137-4145, 1994.

[31] Fannin PC, Marin CN, Socoliuc V, Istratuca GM, "Investigation of particle agglomeration in un-polarized magnetic fluids by means of magnetic resonance measurements", J. Magn. Magn. Mater., vol. 284, pp. 104–112, 2004.

[32] Bessias L, Jaffel LB, Dormann JL, "Relaxation time of fine magnetic particles in uniaxial symmetry**"** Phys. Rev. B, vol. 45, pp. 7805-7815, 1992.

[33] Aharoni A, "Susceptibility resonance and magnetic viscosity", Phys. Rev. B, vol. 46, pp. 5434-5441, 1992.

[34] Chantrell RW, Popplewell J, Charles SW, "Measurements of particle size distribution parameters in ferrofluids", IEEE transactions on magnetics, vol. 14 no. 5, 1978.

[35] Fannin PC, "On the use of dielectric formalism in the representation of ferrofluid data.", Journal of molecular liquids, vol. 69, pp. 39-51, 1996.

[36] Rosensweig RE, "Heating magnetic fluid with alternating magnetic field", J. Magn. Magn. Mater., vol .252, pp. 370–374, 2002.

[37] Odenbach S, "Magnetic fluids suspensions of magnetic dipoles and their magnetic control", J. Phys.: Condens. Matter, vol. 15, pp. 1497–1508, 2003.

[38] Krueger DA., "Absence of anisotropy effects in the magnetization of ferrofluids", J. Appl. Phys., vol. 50, pp. 8169-8171, 1979.

[39] Fannin PC, Scaife BPK, Charles SW, "New technique for measuring the complex susceptibility of ferrofluids", J. Phys. E: Sci. Instrum., vol. 19, pp. 238-239, 1986.

[40] Scaife BPK, "On the low-field, low-frequency susceptibility of magnetic fluids", J. Phys. D: Appl. Phys. vol. 19**,** pp. 195-l97, 1986.

[41] Fannin PC, Scaife BPK, Charles SW, "The field dependence of the complex frequency-dependent susceptibility of magnetic fluids", J. Phys. D: Appl. Phys, vol. 21, pp. 533-534, 1988.

[42] Fannin PC, Charles SW, "The study of a ferrofluid exhibiting both Brownian and Neel relaxation", J. Phys. D: Appl. Phys, vol. 22, pp. 187-191, 1989.

[43] Fannin PC, Charles SW, "The effect of particle concentration on the frequency-dependent susceptibility of ferrofluids", J. Phys. D: Appl. Phys, vol. 22, pp. 449-450, 1989.

[44] Connolly J, St Pierre TG, "Proposed biosensors based on time-dependent properties of magnetic fluids", J. Magn. Magn. Mater., vol. 225, pp. 156-160, 2001.

[45] Fannin PC, "Magnetic spectroscopy as an aide in understanding magnetic fluids", J. Magn. Magn. Mater, vol. 252, pp. 59-64, 2002.

[46] Fannin PC, A.T. Giannitsis, "Investigation of the field dependence of magnetic fluids exhibiting aggregation", Journal of molecular liquids, vol. 114, pp.89-96, 2004.

[47] Hergt R, Hiergeist , Hilger I, Kaiser WA, Lapatnikov Y, Margel S, Richter U, "Maghemite nanoparticles with very high AC-losses for application in RF-magnetic hyperthermia", J. Magn. Magn. Mater, vol. 270, pp. 345–357, 2004.

[48] Chung SH, Hoffmann A, Bader SD, Liu C, Kay B, Makowski L, Chen L, "Biological sensors based on Brownian relaxation of magnetic nanoparticles", Appl. Phys. Letters, vol. 85, n°14, pp. 2971-2973, 2004.

[49] Astalan AP, F. Ahrentorp F, Johansson C, Larsson K, Krozer A, "Biomolecular reactions studied using changes in Brownian rotation dynamics of magnetic particles", Biosensors and Bioelectronics, vol. 19, pp. 945–951, 2004.

[50] Brown WF, "Thermal fluctuations of a single-domain particle", Phys. Rev., vol. 130 n° 5, pp. 1677-1686, 1963.

[51] Fannin PC, Charles SW, "Measurement of the Neel relaxation of magnetic particles in the frequency range 1 kHz to 160 MHz", J. Phys D: Appl. Phys, vol. 24, pp. 76-77, 1991.

[52] Fannin PC, Charles SW, "On the calculation of the Neel relaxation time in uniaxial single-domain ferromagnetic particles", J. Phys D: Appl. Phys, vol. 27, pp. 185-188, 1994.

[53] Hirianca I, Malaescu I, "The rf magnetic permeability of statically magnetized ferrofluids", J. Magn. Magn. Mater., vol. 150, pp. 131-136, 1995.

[54] Malaescu I, Hirianca I, "Relaxation processes of magnetite-based ferrofluids in rf magnetic fields", J. Magn. Magn. Mater., vol. 157/158, pp. 116-118, 1996.

[55] Fannin PC, Relihan T, Charles SW, "Experimental and theoretical profiles of the frequency-dependent complex susceptibility of systems containing

nanometer-sized magnetic particles", Physical Review B, vol. 55, pp. 14423-14428, 1997.

[56] Fannin PC, Charles SW, Relihan T, " On the broadband measurement of the permittivity and magnetic susceptibility of ferrofluids", J. Magn. Magn. Mater., vol. 167, pp.274-280, 1997.

[57] Malaescu I, Marin CN, "Deviation from the superparamagnetic behaviour of fine-particle-systems", J. Magn. Magn. Mater., vol. 218, pp. 91-96, 2000.

[58] Wijaya A, Brown KA, Alper JD, Hamad-Schifferli K, "Selective Heating of Multiple Nanoparticles", Mater. Res. Soc. Symp. Proc. vol. 900E, 2006.

[59] Cregg PJ, Crothers DSF, Weckstead AW, "An approximate formula for the relaxation time of a single domain ferromagnetic particle with uniaxial anisotropy and collinear field", J. Appl. Phys., vol. 76(8), pp. 4900-4902, 1994.

[60] Coffey WT, Kalmykov YuP, Massawe ES, " The effective eigenvalue method and its application to stochastic problems in conjunction with the non linear Langevin equation", Adv. Chem. Phys., vol. 85, pp. 667-745, 1993.

[61] Fannin PC, Charles SW, "Frequency of ferromagnetic resonance in ferrofluids", Phys. Rev. B, vol. 52, pp. 16055-16057, 1995.

[62] Fannin PC, Relihan T, Charles SW, "Investigation of ferromagnetic resonance in magnetic fluids by means of the short-circuited coaxial line technique", J. Phys D: Appl. Phys, vol. 28, pp. 2003-2006, 1995.

[63] Fannin PC, Charles SW, Relihan T, "A study of the effect of an external magnetic field on the resonant frequency of magnetic fluids", J. Magn. Magn. Mater., vol. 162, pp. 319-326, 1996.

[64] Fannin PC, Perov PA, Charles SW, "Complex susceptibility measurements of magnetic fluids over the frequency range 50 MHz to 18 GHz", J. Phys D: Appl. Phys, vol. 32, pp. 1583-1586, 1999.

[65] Fannin PC, Vincent D, Noyel G, "On the measurement of the complex susceptibility and permittivity of magnetic fluids by means of two different measurement techniques", J. Magn. Magn. Mater., vol. 201, pp. 116-118, 1999.

[66] Marin CN, Malaescu I, Ercuta A, "The dependence of the effective anisotropy constant on particle concentration within ferrofluids, measured by magnetic resonance", J. Phys. D: Appl. Phys., vol. 34, pp. 1466–1469, 2001.

[67] Fannin PC, "Use of ferromagnetic resonance measurements in magnetic fluids", Journal of molecular liquids, vol. 114, pp. 79-87, 2004.

[68] Fannin PC, Scaife BKP, Giannitsis AT, Mac Oireachtaigh C, "High frequency ferromagnetic resonance measurements in magnetic fluids", J. Magn. Magn. Mater., vol. 289, pp. 159–161, 2005.

[69] Fannin PC, Malaescu I, Marin CN, "The effective anisotropy constant of particles within magnetic fluids as measured by magnetic resonance", J. Magn. Magn. Mater., vol. 289, pp. 162-164, 2005.

[70] Coffey WT, Fannin PC, "Internal and Brownian mode-coupling effects in the theory of magnetic relaxation and ferromagnetic resonance of ferrofluids", J. Phys.: Condens. Matter, vol. 14, pp. 3677–3692, 2002.

[71] Coffey WT, Kalmykov YP, "Transverse complex magnetic susceptibility of single-domain ferromagnetic particles with uniaxial anisotropy, subjected to a longitudinal uniform magnetic field", Phys. Rev. B, vol. 56, pp. 3325-3337, 1997.

[72] Guardia P, Batlle-Brugal B, Roca AG, Iglesias O, M. Morales P, Serna CJ, Labarta A, Batlle X, "Surfactant effects in monodisperse magnetite nanoparticles of controlled size", Submitted to Journal of Magnetism and Magnetic Materials.

[73] Vincent D, Jorat L, Monin J, Noyel G, "Improvement of the transmission/reflection method for dielectric and magnetic measurement on liquids between 0.1 and 20 GHz", Meas. Sci. Technol., vol. 5, pp. 990-995, 1994.

[74] Weir WB, "Automatic measurement of complex dielectric constant and permeability at microwave frequencies" Proceeding of the IEEE, vol 62 n° 1, pp. 33-36, 1974.

[75] Collin RE, "Field theory of guided waves", Wiley-IEEE Press Series, New York, 1990.

[76] Keblinski P, Cahill DG, Bodapati A, Sullivan CR, Taton TA, "Limits of Localized Heating by Electromagnetically Excited Nanoparticles", Journal of Applied Physics, vol. 100, pp. 054305-1 054305-5, 2006.

[77] Adair RK, "Vibrational resonances in biological systems at microwave frequencies", Biophisical Journal, vol. 82, pp. 1147-1152, 2002.

[78] Bagaria HG, Johnson DT, "Transient solution to the bioheat equation and optimization for magnetic fluid hyperthermia treatment", International. Journal of Hyperthermia, vol. 21 n°1, pp. 57-75, 2005

[79] Nicolas L, "Interactions between Electromagnetic Fields and Biological Tissues: Questions, Some Answers and Future Trends", available on www.cmap.polytechnique.fr/~poignard/

[80] Abramowitz M, Stegun IA, "Handbook of Mathematical Functions: with Formulas, Graphs, and Mathematical Tables", Dover Publications, New York, 1965.

[81] Jackson JD, "Classical Electrodynamics", Wiley & Sons, New York, 1975.

[82] Muller C, "Foundations of the mathematical theory of electromagnetic Waves", Springer, Berlin, 1969.

[83] Polyanin AD**, "**Handbook of Linear Partial Differential Equations for Engineers and Scientists", Chapman & Hall/CRC, 2002.